FCT
Fundação para a Ciência e a Tecnologia
MINISTÉRIO DA CIÊNCIA, TECNOLOGIA E ENSINO SUPERIOR

POPH
PROGRAMA OPERACIONAL POTENCIAL HUMANO

QREN
QUADRO DE REFERÊNCIA ESTRATÉGICO NACIONAL
PORTUGAL 2007-2013

UNIÃO EUROPEIA
Fundo Social Europeu

Universidade do Minho
Escola de Ciências

Cristóvão de Sousa Dias

Kinetics of thin-film mass transport on crystalline and amorphous substrates

Maio de 2011

Cristóvão de Sousa Dias **Kinetics of thin-film mass transport on crystalline and amorphous substrates**

UMinho | 2011

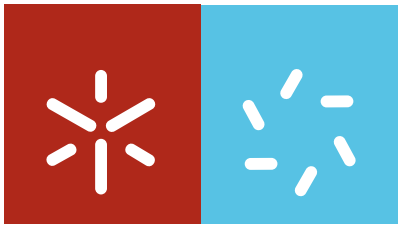

Universidade do Minho
Escola de Ciências

Cristóvão de Sousa Dias

Kinetics of thin-film mass transport on crystalline and amorphous substrates

Programa Doutoral em Física

Trabalho realizado sob a orientação do
Professor Doutor António Manuel Rosa Cadilhe
e da
Professor Doutor José Manuel Pereira Carmelo

Maio de 2011

"A physicist is just an atom's way of looking at itself."

Niels Bohr

Abstract

Deposition phenomena have always attracted the attention of researchers from different fields. Being common to many physical systems, deposition processes are also a challenge for theoretical studies. Simulations can capture essential features of deposition and subsequent physical processes on substrates, responsible for the macroscopic properties of the system. In this thesis we considered several computational techniques to study systems where deposition on crystalline and amorphous substrates take place, namely, we studied the deposition of ethanol and carbon monoxide on crystalline substrates and their subsequent oxidation, as well as the deposition and relaxation of particles on crystalline substrates and on the surface of nanoclusters.

Electro-oxidation of ethanol is a key mechanism in fuel-cells technology. To study it on a surface, a sequential adsorption model of dimers is introduced, where the dimer dissociation depends on the occupation state of the nearest neighbors. We provide an analytical solution for the proposed model in $1D$ and extend its study to $2D$ through Monte Carlo simulations. We mainly focus on the characterization of the jamming state coverage and percolation properties of the products. Besides, we show that in the presence of quenched impurities one of the species is favored and the percolation threshold is shifted.

We characterize the nature of irreversible phase transitions on a nonequilibrium system with absorbing states. We apply different methods to a generalized version of the Ziff, Gulari, and Barshad model, i.e., in the presence of a prescribed fraction of inert sites. These methods exploit short- and long-range correlations typical of first- and second-order phase transitions. We present a detailed analysis of the phase transitions to an

absorbing state. Our results report a critical inert site coverage value of 2.5%, lower than previous estimates of 7.8%, for the change in the nature of the transition from first to second order.

To study epitaxial thin-film growth, a new model is introduced and extensive kinetic Monte Carlo simulations performed for a wide range of fluxes and temperatures. Varying the deposition conditions, we find a rich growth diagram. The model reproduces several known regimes and in the limit of low particle mobility a novel regime is observed. A relation is also postulated between the temperatures of the kinetic and thermal roughening transitions.

Finally, we performed temperature accelerated dynamics simulations for the growth of copper nanoclusters. We used common neighbor analysis to identify the morphology of structures present during growth. A new model was conceived and implemented to study atoms deposition on a cluster, since the number of atoms impinging on the cluster depend on its size and each atom arrives from a random direction. The transition from the 55 Mackay icosahedral to the 75 decahedral structure was studied in detail in terms of the influence of temperature and flux at experimental conditions.

Resumo

Fenómenos de deposição têm, desde sempre, atraído a atenção de investigadores de diferentes áreas do conhecimento. Sendo comuns em vários sistemas físicos, os processos de deposição são também um desafio para estudos teóricos. Simulações podem captar as características essenciais da deposição e dos processos que ocorrem no substrato influenciando as propriedades macroscópicas do sistema. Nesta tese consideraram-se várias técnicas computacionais para o estudo de sistemas onde a deposição toma lugar em substratos cristalinos ou amorfos, nomeadamente, estudámos a deposição de etanol e monóxido de carbono em substratos cristalinos e o crescimento de partículas com dimensões nanométricas.

A electro-oxidação do etanol é um mecanismo chave na tecnologia de células de combustível. Para estudar este processo numa superfície, um modelo de adsorção sequencial de dímeros é apresentado, onde a dissociação dos dímeros depende da ocupação do vizinho mais próximo. Nós aprensentamos uma solução analítica para o modelo proposto em $1D$, e estendemos o estudo para $2D$ através de simulações de Monte Carlo. Focámo-nos principalmente na caracterização do estado de cobertura limite e das propriedades percolativas dos produtos de reacção. Além disso, mostrámos que a presença de impurezas inertes favorece uma das espécies e que o ponto crítico da transição percolativa é desviado.

Caracterizámos a natureza de uma transição de fase irreversível de um sistema fora de equilíbrio com estados absorventes. Aplicámos diferentes métodos a uma versão generalizada do modelo de Ziff, Gulari e Barshad na presença de uma fracção de impurezas inertes. A metodologia proposta explora correlações de curto e longo alcance típicas de

transições de fase de primeira e segunda ordem. Apresentámos uma análise detalhada das transições de fase para um estado absorvente. Os nossos resultados reportam uma cobertura crítica de impurezas de 2.5%, abaixo das estimativas anteriores de 7.8%, onde a natureza da transição de fase altera-se de primeira para segunda ordem.

Para estudar crescimento epitaxial de filmes finos, um novo modelo é apresentado e simulações de Monte Carlo cinético são realizadas para uma grande variedade de fluxos e temperatura. Alterando as condições de deposição, encontrámos um diagrama de modos de crescimento bastante rico. O modelo reproduz vários regimes conhecidos e no limite de baixa mobilidade, um novo regime é observado. Uma relação entre as temperaturas da transição cinética e térmica de rugosidade é também encontrada.

Finalmente, realizámos simulações utilizando o método de dinâmica molecular acelerada pela temperatura para o crescimento de nanopartículas de cobre. Utilizámos a medição de vizinhos comuns para identificar a morfologia das diferentes estruturas presentes durante o crescimento. Um novo modelo foi criado e implementado para a deposição de átomos numa nanopartícula em que o número de átomos que atinge o agregado por unidade de tempo depende do tamanho do mesmo e cada átomo chega a partir de uma direcção aleatória. A transição de uma estrutura de 55 Mackay icosaédrica para 75 decaédrica foi estudada em detalhe em termos da influência do fluxo e da temperatura em condições experimentais.

Preface

The main challenge of my PhD is an attempt to understand the relevant phenomena occurring during deposition on substrates. Statistical physics ideas and several computational techniques have been considered to develop conceptual models and shed some light on the main mechanisms driving the process.

This thesis is the result of my PhD research, started in May of 2007, at the *Universidade do Minho*, in the field of computational statistical physics. I have got the opportunity to interact with many people at the University, the *Los Alamos National Laboratory*, and several conferences, who contributed to my work.

I thank my supervisor Professor António Cadilhe for providing me with all the necessary conditions to perform my PhD thesis, allowing me to attend to several international conferences and schools, as well as the opportunity to make an internship at the *Los Alamos National Laboratory*. Through him I was also introduced to the field of far-from-equilibrium statistical physics when I was an undergraduate student, and for that I am also truly grateful.

I am specially thankful to Nuno Araújo for collaboration in some of the most significant work of my PhD thesis, for helping me during the writing part, to keep me in contact with some of the actual challenges in statistical physics, and mainly for his friendship.

My thanks also to Dr. Arthur Voter for the opportunity to work during three months with him, at the *Los Alamos National Laboratory*, from which I have, definitely, benefited.

Nonetheless, this thesis has profited from the careful reading and scrutiny of my friend João Filipe Marques who has provided me with great advises and helpful tips.

In addition, I wish to acknowledge the *Fundação para a Ciência e a Tecnologia* the fellowship (SFRH/BD/31833/2006) and to the project SeARCH the computational facilities.

My final words go to my wife for being at my side during all these years.

Contents

Abstract **v**

Resumo **vii**

Preface **ix**

Contents **xi**

List of Tables **xxi**

List of Figures **xxiii**

Introduction **1**

1 Computational Methods **5**

1.1 Standard Monte Carlo 7

1.1.1 Equilibrium Problems 8

1.1.2 Nonequilibrium Problems 14

1.2 Kinetic Monte Carlo 17

1.2.1 Infrequent Events 18

1.2.2 Transition-state-theory 19

1.2.3 Adatoms Surface Dynamics 21

1.3 Molecular Dynamics 23

1.3.1 Dynamics 23

1.3.2 Integration Methods . . . 25
1.3.3 Particles Interaction . . . 28
1.4 Accelerated Molecular Dynamics . . . 31
1.4.1 Temperature Accelerated Dynamics . . . 31
1.4.2 Other Methods . . . 38

2 Substrate deposition with reaction 41
2.1 Catalysis models . . . 42
2.1.1 Ethanol electro-oxidation model . . . 42
2.1.2 Carbon monoxide oxidation model . . . 45
2.2 1D ethanol electro-oxidation . . . 46
2.2.1 Analytical study . . . 46
2.2.2 1D Monte Carlo simulations . . . 53
2.3 2D ethanol electro-oxidation . . . 56
2.3.1 Clean substrate . . . 57
2.3.2 Substrate with impurities . . . 60
2.4 2D carbon monoxide oxidation . . . 62
2.5 Conclusions . . . 67

3 Substrate deposition with relaxation 73
3.1 Model definitions . . . 75
3.1.1 Rates calculation . . . 76
3.1.2 Corner rounding process . . . 78
3.1.3 Preventing evaporation . . . 78
3.2 Roughness evolution . . . 80
3.2.1 Schwoebel barrier effect . . . 81
3.3 Growth regime transitions . . . 82
3.3.1 BD to BDLR . . . 84
3.3.2 BDLR to kinetic rough . . . 85

3.3.3 Kinetic rough to layer-by-Layer 86
3.3.4 Thermal roughening transition 88
3.3.5 Growth mode diagram 89
3.4 Main conclusions 89

4 Growth of nanoclusters **93**
4.1 Free nanocluster growth 94
4.2 Vapor Cluster Growth Model 98
4.2.1 Deposition Model 98
4.2.2 Methods of Analysis 100
4.3 Structures Formation 102
4.3.1 Computational boost 103
4.3.2 Common Neighbor Analysis index distribution 105
4.3.3 Influence of deposited particles 106
4.3.4 Activation Barriers evolution 107
4.4 Main Conclusions 108

Final remarks **113**

Bibliography **117**

Nomenclature

E	energy
P_i	probability of finding the system in state i
Ω	number of accessible states
Z	partition function
O	observable
k_B	Boltzmann constant
T	temperature
W	Markov process transition probability
N	number of states
w	Markov process transition rate
H	Hamiltonian
σ	spin value
B	applied magnetic field
δt	time increment
k	TST process rate

TST	Transition state theory
E_a	activation energy
ν	attempt frequency prefactor
ν_i^{min}	normal modes frequency at the energy minimum
ν_i^{sad}	normal modes frequency at the energy saddle point
$\mathbf{r}$	Cartesian coordinates
$\mathbf{f}$	force
m	mass
$\mathbf{q}$	generalized coordinates
$\mathbf{L}$	Lagrangian
$\mathbf{p}$	momentum
V	interaction potential
U	external potential
V_{hs}	hard sphere potential
V_{ss}	soft sphere potential
V_{LJ}	Lennard-Jones potential
T_{low}	TAD low temperature
T_{high}	TAD high temperature
TAD	Temperature accelerated dynamics
NEB	Nudged Elastic Band Method

BCMD Basin-constrained Molecular Dynamics

HTST Harmonic transition state theory

$t_{i,low}$ time of process i at T_{low}

$t_{i,high}$ time of process i at T_{high}

δ probability of a transition still occur

k_d dimer deposition rate

k_m monomer deposition rate

CSA cooperative sequential adsorption

RSA random sequential adsorption

y_A monomer adsorption probability

y_B dimer adsorption probability

P_n probability of finding a site with length $\ell \geq n$

θ coverage

θ_m coverage of monomers

θ_d coverage of dimers

s_m rate of monomer adsorption

s_d rate of dimer adsorption

R ratio between dimers and monomers deposition rate, $R = k_d/k_m$

$r_{\min}$ minimum particle radius

$r_{\max}$ maximum particle radius

θ_∞	coverage at the jamming limit
R_L	spanning probability
P_∞	fraction of sites belonging to the largest cluster
$\langle P \rangle$	average cluster size
R_c	percolation threshold
L	system linear size
D_f	fractal dimension
$\langle s_{max} \rangle$	average size of the largest cluster
M_2	second momentum of the cluster size distribution, excluding the largest cluster
N	total number of lattice sites
$g(r)$	connectivity correlation function
θ_{imp}	Coverage of impurities
$P(s)$	cluster size distribution function
s	size of a cluster
E_i	activation energy of process i
E_m	activation energy for terrace diffusion
n_0	number of initial neighbors
n_0	number of final neighbors
J_{pp}	energy of particle-particle interaction
ϕ	ratio of binding energy and thermal energy

ν_d attempt frequency for the terrace diffusion process

R_E ratio between activation energy for terrace diffusion and energy of particle-particle interaction $R_E = E_m/J_{pp}$

F flux of impinging atoms in monolayers per second (ML/s)

$W(t)$ roughness at time t

$h(x,t)$ height of the column x at time t

β growth exponent

ρ_b density of dangling bonds

σ_b^2 variance of the density of dangling bonds

ρ_v density of vacancies

σ_v^2 variance of the density of vacancies

CNA common neighbor analysis

Dh decahedral structure

TO truncated octahedral structure

Ih icosahedral structure

List of Tables

4.1 CNA analysis for different magic numbers, where Dh are decahedral structures, Ih are Icosahedral, and TO truncated octahedral. 104

List of Figures

1.1 Schematic of the relation between theory, experiments, and computer simulations (adapted from Allen et al [25]). 6
1.2 System A in contact with a heat bath A'. 9
1.3 System A in contact with two heat baths A' and A''. 14
1.4 Transition state theory illustration with a) the energy barrier and b) the potential energy surface with the saddle points. 20
1.5 Adatom diffusion scheme with energy barriers. 21
1.6 Nearest and next-nearest neighbors in a square lattice for a diffusion hop. . 22
1.7 Pair potentials of a) Hard sphere, b) Soft sphere, and c) Lennard-Jones. . . 29
1.8 Molecule with 3 atoms and 2 bonds. 30
1.9 Scheme of the TAD method stopping time. 33
1.10 Scheme of the stop condition to the TAD method stopping time. 35
1.11 Scheme of the TAD method stopping time with revisiting states. 36
1.12 Scheme of the Parallel replica method. 39
1.13 Scheme of the hyperdynamics method. 40

2.1 Schematic representation of the adsorption rules. The A-specie (red) deposition with two empty spaces gives B-products (blue) or with only one empty space gives C (green). 45
2.2 Catalog of possible ways of splitting a segment of empty sites with length $\ell \geq n$. 47

2.3 Coverage ($\theta(t)$) and rates ($s(t)$) of adsorption as a function of time obtained through Monte Carlo simulations (symbols) and analytically (solid line) for equal rates of adsorption (a) and (d), preferential carbon adsorption (b) and (e), and different rates of adsorption ($k_d = 0.5$ and $k_m = 1$) (c) and (f). Total coverage and rates of adsorption (open squares), dimers (full squares), and monomers (open circles). 54

2.4 Coverage of dimers (open circles) and monomers (full squares) for Monte Carlo simulations and obtained analytically (solid line), with the analytical solution (solid line), at the jamming limit as a function of the ratio between the rate of deposition of dimers and monomers R. 56

2.5 Jamming coverage (θ_∞) as a function of the ratio between the rate of adsorption of dimers and monomers R, in $2D$, of dimers (open circles) and monomers (full squares) for a system size of 512^2 lattice sites. 57

2.6 a) Dependency on the ratio R of the spanning probability R_L for dimers (open) and monomers (full). Square lattices have been considered with 128^2 (squares), 256^2 (circles), and 512^2 (triangles) lattice sites, for the spanning probability R_L, clusters medium size $\langle P \rangle$(bottom inset), and fraction of sites belonging to the largest cluster P_∞ (top inset). b) Percolation threshold (R_c) as a function of the system sizes, for linear sizes of $L = \{32, 64, 128, 256, 512\}$, for dimers (full circles) and monomers (full squares). 58

2.7 a) Largest cluster (s_{max}) and (inset) second moment of the cluster size distribution function (M_2) at R_c as a function of the system sizes, for linear sizes of $L = \{32, 64, 128, 256, 512\}$, for dimers (full circles) and monomers (full squares). b) correlation function ($g(r)$) for dimers (monomers on the inset) for a system of linear size $L = 1024$ and 100 samples. 59

2.8 Difference in the jamming coverage of monomers and dimers as a function of the impurities coverage, in $2D$, for $R = 0.1$ (open circles), $R = 1$ (full squares), and $R = 10$ (full circles) for a system size of 512^2 lattice sites. . . 61

2.9 Spanning probability as a function of the ratio R, in $2D$, for a) monomers with impurities coverage from right to left of 0%, 10%, 20%, 30% and, 40%, and b) dimers with impurities coverage from left to right of 0%, 10%, 20%, and 30%. Simulation of a system size of 512^2. Clusters medium size $\langle P \rangle$ on the bottom inset and maximum cluster size P_∞ on the top inset. 62

2.10 Cluster analysis as a function of the impurities coverage. Simulation of sizes 128×128 (squares), 256×256 (circles), and 512×512 (triangles), for the spanning probability R_L, clusters medium size $\langle P \rangle$ (bottom inset), and maximum cluster size P_∞ (top inset) at a) monomers at $R = 0.1$ and d) dimers at $R = 10$. 63

2.11 Snapshots of a clean substrate system (top) and for a system with 2.5% of coverage by impurities (down). System sizes are 100×100 sites (left) and 400×400 sites (right), where black particles are impurities, dark gray monomers, light gray dimers and empty sites are white. 64

2.12 Monomers cluster-size distribution functions at the upper-bound transition for: a) different impurities coverage, in a logarithmic scale, for a system of size 800×800 lattice sites. From bottom to top we have 0%, 2%, 3%, and 7.8% of impurities coverage b) for the original ZGB model from the shortest function to the longest we have system sizes of 100×100, 400×400, 800×800, 1600×1600, and 3200×3200 lattice sites in a double logarithmic scale. 70

2.13 Concavity of the cluster-size distribution functions for different coverages by impurities, for systems of size 100×100 (open circles), 400×400 (open squares), and 800×800 (asterisks) lattice sites. 71

2.14 Spanning probability R_L as a function of the approximation to the transition point y_c for 2% (right) and 3% (left) of impurities coverage with a relaxation time of 2×10^5 MCS and a system size of 400^2. 71

3.1 Ballistic deposition rule used in the model. 76

3.2 Neighbor counting for a mobility process, where 1, 2, and 3 are the neighboring sites before the hop, and 4, 5, and 6, the ones after the hop. 77

3.3 a) Scheme of the *corner rounding* process and of the b) energy landscape. . 78

3.4 Single adatom evaporation prevention. 79

3.5 Hoshen-Kopelman cluster counting algorithm. 79

3.6 Cluster measurement to prevent evaporation. 80

3.7 a) Roughness evolution at $\phi = 3$ as a function of time defined in units of deposited layers, for $F = \{5, 10^3, 10^7, 10^{10}\}$ML/s. At higher fluxes the growth regime is rough and at lower fluxes the roughness oscillates representing a layer-by-layer growth. b) The roughness exponent β as a function of $1/F$ for different values of ϕ. From left to right $\phi = \{1, 2, 3, 4, 5\}$, measurements performed after 10^2 deposited monolayers. 81

3.8 Snapshots of the observed plateau in the roughness with a) first roughness increase, b) roughness plateau, and c) second roughness increase, for a system of 100 lattice sites and 11 deposited layers at $\phi = 4$. Each color corresponds to 10 consecutively deposited layers. 82

3.9 Snapshots of the different growth regimes a) BD, b) BDLR, c) kinetic rough, and d) layer-by-layer, for a system of 100 lattice sites and 100 deposited layers at $\phi = 3$. Each color corresponds to 10 consecutively deposited layers. 83

3.10 Density of dangling bonds (a), ρ_b, and its variance, σ_b^2, (b) as a function of $1/F$ for different values of ϕ after 100 deposited layers. From left to right, $\phi = \{1, 2, 3, 4, 5\}$. The insets are at $\phi = 3$ and for different system sizes of L=$\{400, 1600, 3200\}$. 84

3.11 The density of vacancies (a), ρ_v, and its variance (b) as a function of $1/F$ for different values of ϕ after 100 deposited layers. From left to right, $\phi = \{1, 2, 3, 4, 5\}$. The insets are at $\phi = 3$ and for different system sizes of L=$\{400, 1600, 3200\}$. 86

3.12 Growth mode diagram with the kinetic roughening transition between Layer-by-layer to Kinetically Rough growth. a) The flux as a function of ϕ for values, from bottom to top, of $R_E = 10$, $R_E = 5$, and $R_E = 1$. b) The ratio R as a function of ϕ where the symbol (Triangle) is $R_E = 10$, (Circle) is $R_E = 5$, and (Square) is $R_E = 1$. 87

3.13 a) Growth exponent evolution as a function of $1/F$ for various ϕ values near ϕ_c. From bottom to top we have $\phi = \{2, 1.8, 1.4, 1.2, 1.1\}$. b) Roughness as a function of the temperature for lattice sizes, from bottom to top, of 100, 200, 400, 1000 and 2000 on a previously deposited film of 10 ML. . . . 88

3.14 Final growth mode diagram, where TR and KR are the *Thermally Rough* regime and *Kinetically Rough* regime respectively. 90

4.1 Some magic sizes for Cu cluster, at sizes of 13, 19, 55 and 75. 96

4.2 Scheme with the sphere used to compute the flux, and the representation of the randomly generated direction of impinging atom. 100

4.3 Scheme of the CNA index representation. 102

4.4 Scheme of the classification of connection between common neighbors. . . . 103

4.5 Boost of the TAD relaxation over MD as a function of the size of the cluster for a) from top to bottom temperatures of 50K, 100K, 150K, and 200K for a pressure of 0.1 atm. b) from top to bottom pressures of 0.01 atm, 0.1 atm, 1 atm, and 10 atm for a temperature of 50K. 105

4.6 Distribution of the CNA index P(5,5,5) for a 75 atoms cluster at, left plots, a pressure of 1 atm and temperatures from top to bottom of 50, 100, 150, and 200 K. Right hand-side plots, a temperature of 150 K and pressures from top to bottom of 10, 1, 0.1, and 0.001 atm. 109

4.7 CNA P(5,5,5) index distribution for all samples, with different pressures and temperatures. A- ICO, B- DECA and C- FCC. 110
4.8 Most common structures of 75 atoms cluster for A-Icosahedral, B-Decahedral, and C-FCC. 111
4.9 Distribution of a) distances of the new particles to the center of mass of the cluster and b) angle between the different particles for decahedral (red) and icosahedral (green) formation. 112
4.10 Distribution of a) average activation barrier found for each size and b) maximum activation barrier found for each size, for decahedral (red) and icosahedral (green) formation. 112

Introduction

Natural and man-made surfaces are everywhere around us playing a relevant role in our daily life. Several examples can be found like thin-films, either semiconductors [1, 2] or materials coating [3, 4], membranes in biological systems [5, 6], or catalysts used in industry for environmental reasons [7, 8, 9, 10]. Therefore, their importance on technological applications is unquestionable. Problems on surfaces have been addressed through analytical methods [11] or computationally with techniques such as first principles [12], Monte Carlo [13], or molecular dynamics [14]. More recently, multiscale modeling has also been considered to study the system across different length and time scales [15].

The phenomenon of deposition relies mainly on two important characteristics: the material to be deposited and the type of substrate. On what concerns the first, the deposition can be of atoms, like using, for instance, the well known deposition technique of Molecular Beam Epitaxy [16], or once on the surface, deposited particles can react, diffuse, or detach [7, 17]. Also the deposition of clusters needs to be taken into account, where can be used to study, for example, quantum dots or colloids adsorbed on the surface [18]. The type of substrate, crystalline or amorphous, leads to fundamentally different surface properties. The crystalline substrate has the characteristics of having a regular arrangement. It can be treated as the faces of a crystal, where each face can have a different orientation. Amorphous substrates, can also be in the thin-film form, with the famous example of amorphous silicon (used in solar cells), or on a cluster form, where non-crystalline structures can play a key role. The importance of nanoclusters to society is well known, since they are considered by many the pillars of nanoscience [19, 20]. Their

applicability goes from materials with optical properties [21, 19] to catalysts due to their large surface/volume ratio [22].

The thesis is devoted to different phenomena occurring at surfaces, with special focus on deposition. The deposition mechanism and the subsequent ones are studied on crystalline and amorphous substrates. On crystalline substrates, diffusion of atoms upon deposition is studied. Also the study of reactions after adsorption on a crystal is performed. Amorphous substrates are modeled in the form of nanoclusters, where structures can take both crystalline and amorphous form. The study in this case is focused on the growth of free nanoclusters and the type of structures obtained.

For reactions on substrates, typical approach relies on the study of basic reaction mechanisms through first principles [23, 24] or, in the case of large molecules, with molecular dynamics [25, 14]. However, to understand cooperative phenomena at larger length and timescales, Monte Carlo methods are usually recommended. For example, in thin-films growth, simplified analytical and Monte Carlo models have been applied, where either, only deposition is considered, or simplified diffusion mechanisms [26, 27]. If more realistic mechanisms and rates are desired, kinetic Monte Carlo models can be used [28, 26, 29, 30, 31, 32, 33]. Molecular dynamics is another option, but only smaller systems and shorter timescales can be considered [34, 35]. This is appropriate when details of the dynamics are a must, which is not usually the case for the study of cooperative phenomena. Finally, in the growth of nanoclusters, details of structure formation and evolution are relevant subjects [17, 20]. It can be addressed through optimization methods to identify stable structures [36, 37, 38, 39]. However, methods that provide more details of the dynamical evolution to study kinetic effects on a growing cluster like molecular dynamics or accelerated dynamics methods need to be applied.

One chapter is devoted to reactions on crystalline substrates, where the oxidation phenomenon plays the leading role, with an industrial importance for pollution control, energy production, and material protection. One example of such phenomenon is the ethanol electro-oxidation typically related with energy production in fuel cells technology

[40], which is also addressed here. The effect of impurities is also taken into account. Since desorption can be neglected during the electro-oxidation process, the system evolves to a jamming state where percolation occurs. For industrial pollution control, carbon monoxide oxidation is an elected reaction on the heterogeneous catalysis field, due to its relevance for the automobile industry to fulfill tighten emission standards [10]. Here we chose to study surface poisoning transitions, where the nature of the transition is discussed and the effect of impurities monitored. In these systems, since desorption is negligible, RSA models can be applied [41]. However, if we consider a system where desorption becomes a relevant mechanism, models of deposition and reaction [42], with or without diffusion [43, 44], have been used. We used standard Monte Carlo, which is the proper one to study large scale systems with complex dynamics and it is tailored to study phase transitions.

The second chapter of results is dedicated to the study of thin-film growth, more precisely, epitaxial growth. The subject is of great technological interest, since the ability to growth smooth surfaces has applications on semiconductors [45], while mound growth is important to catalysis [7, 9] and quantum dots [46]. The main technique for controlled thin-film growth is molecular beam epitaxy, which can be used to produce a mono-crystalline films. We have chosen to study thin-film growth on crystalline substrates since it is better behaved than amorphous substrates, which allows more control. Besides, diffusion rates can be experimentally determined. Basic thin-film growth models do not account for diffusion, like random deposition, ballistic deposition, or Eden model [47]. Further examples, include solid-on-solid models with local relaxation [48, 49, 27], or neighbor counting models [50, 51, 52, 26]. We propose a (1+1)-dimensional study, as it can provide insight about relevant mechanisms and is computationally less demanding. We performed a fundamental study, using kinetic Monte Carlo, of growth regimes and present a phase diagram.

The final chapter of results is applied to the growth of nanoclusters. The relevance stems from the fundamental interest to either identify stable equilibrium configurations or to generate kinetically trapped, out-of-equilibrium, ones. Typical structures include the

crystalline type, with an FCC configuration for large clusters, or an octahedron structure for smaller ones. Amorphous or pseudo-crystalline structures are of great relevance, where the former can be icosahedral with fivefold symmetry or decahedral structure with FCC type facets that can be considered quasi-crystalline. We also studied a kinetic growth model to understand the influence of the deposition rate on the adopted structure by the nanocluster. In contrast, in optimization studies, kinetic effects are not accounted for, as well as the randomness provided by the impinging gas atoms. Both temperature and pressure influence were monitored. We used temperature accelerated dynamics [53, 54] to study the influence of pressure at experimental conditions, while temperature had to be kept sufficiently low to improve the boost factor.

Chapter 1

Computational Methods

The use of computational methods can be motivated by numerous factors. One can say, for instance, that it is the only possible way to study a system for which no analytical solution can be found, or that controlled experiments are not easily reproducible (or not recommended) like, e.g., astrophysics experiments, nuclear reactions, or epidemics.

Landau and Binder [13] have schematically represented the study of natural phenomena by a triangle, where at its vertices are theory, experiment, and simulation. Each vertex is dependent on the others and the nature is positioned in the center of the triangle. We present a scheme adapted from Allen and Tildesley [25] on Figure 1.1, where simulations are also related with theory and experiments, but focus on these relations as a test for models or theories.

On materials simulations, different length scales are considered. Typically four length scales [55]: electronic structure, atomistic, microstructure, and continuum. If we observe materials from different scales, we see that different physical properties need specific simulational procedures. Starting at the electronic scale (around one Ångstrom), in the domain of quantum mechanics, the solution of the Schrödinger equation has to be found. This leads to the use of first principles computational methods [56], which are computationally demanding techniques that can only be applied to very small systems. When increasing the scale into the atomistic level, which is above the electronic scale until hundreds of

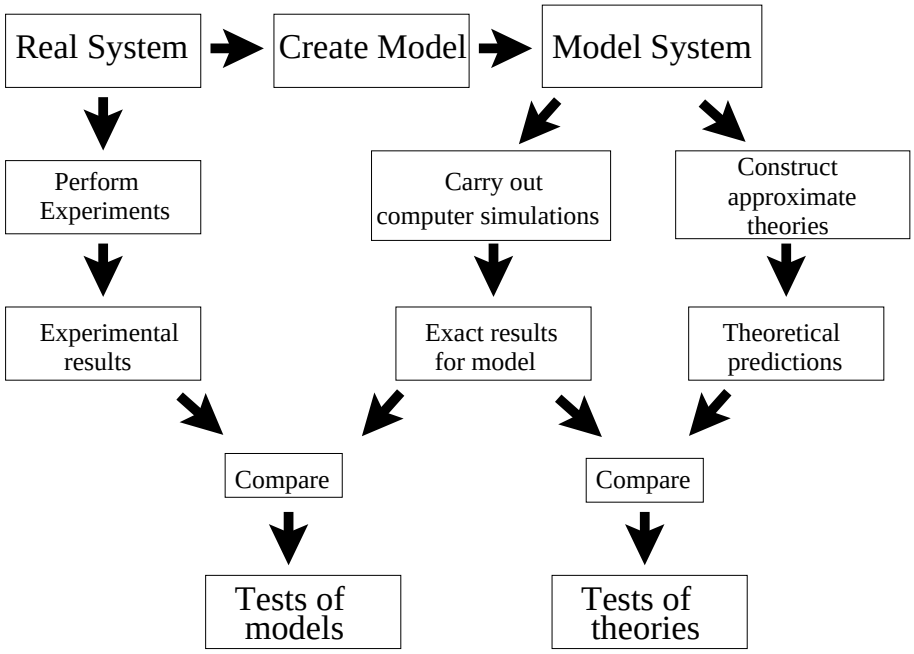

Figure 1.1: Schematic of the relation between theory, experiments, and computer simulations (adapted from Allen et al [25]).

nanometers, an incomparably larger number of particles has to be taken into account. For that reason, more efficient techniques like Molecular Dynamics (MD) [25, 14] or Monte Carlo methods (MC) [57, 13] have to be applied. At the meso and continuum scales, which are from tens of nanometers to the centimeter scale, the number of particles is not accountable. This is the scale of applications, where the individual particles are not taken into account and the system is considered as continuum. In these case, the system is usually discretized into a mesh cell, and methods like Finit-elements methods (FEM) [58] are used.

Despite the specificity of each length scale, a necessity to create computational methods that simulate across length scales arises. This is mainly to capture small scale effects on large systems without wasting time performing all small length features. Some examples of multi-scale simulational methods are, the Car-Parinello (*ab initio*-MD) method [15], Multiscale Finite Element method [59], Coarse-grained Molecular Dynamics [60], Quasicontinuum method [61], Macro-atomistic *Ab initio* dynamics [61], or Heterogeneous

Multiscale method [61].

This chapter is organized as follows: first the Standard Monte Carlo method is introduced on Section 1.1, in Section 1.2 the kinetic Monte Carlo model is presented, the method of Molecular Dynamics is on Section 1.3, and finally Accelerated MD methods are discussed on Section 1.4.

1.1 Standard Monte Carlo

The Monte Carlo method is a technique used to carry out sampling of distributions [62], which relies on random sampling, i.e., the generation of sequences of random numbers[1]. It accounts for transition probabilities between states [63] resumed in 3 steps: generate initial configuration, generate a new state, and evaluation of its acceptance.

A considerable number of physical problems are addressed through SMC. It is an useful method for numerical integration in any dimension, however, since deterministic numerical methods, like the Trapezoidal rule or Simpson rule, are more efficient at low dimensions, SMC is the chosen method for higher ones. It is tailored to study systems that have the possibility to be straightforwardly discretized or through a more complex approximation [13] by the creation of specific models. It is used to solve problems where analytical or deterministic numerical methods fail, like problems with many degrees of freedom, which are the most relevant systems in nature. As a set of examples of its use on complex systems, we have the adsorption on surfaces [41], catalysis [64, 65, 42], thin-film growth [47, 26, 31], fluids [66], and complex networks [67].

Historically, the statistical sampling, basis of SMC, has been first applied to mathematical problems like the estimation of π or numerical integration [68, 69] with the Buffon needles problem. In physics, the SMC method has been first used for nuclear calculations at the Los Alamos National Laboratory [70, 71] and to other systems, like hard sphere interaction, with the use of the Metropolis algorithm [72].

[1] Numbers are only generated in a pseudo-random way.

This section will be divided by the nature of the physical problems to be studied. On the next subsection, equilibrium problems will be defined, which are the most extensively studied through SMC. Then, nonequilibrium systems will be approached on Section 1.1.2, which the interest has testified an explosive growth in the last decades [73].

1.1.1 Equilibrium Problems

For a better view into equilibrium problems, it is first necessary to understand which are the conditions for a thermodynamic equilibrium [74]. To obtain thermodynamic equilibrium three conditions must be fulfilled. First the condition of mechanical equilibrium, where no unbalanced forces or torques are applied to the system, then the chemical equilibrium, with no global change due to chemical reactions or diffusion, and the thermal equilibrium, where there is a constant temperature inside the system and between the system and the surroundings.

In thermodynamics, equilibrium systems can be considered of three types: Isolate, close, and open. Isolated systems are associated to the microcanonical ensemble where no exchange of heat and matter with the surrounding is possible. The closed systems are related to the canonical ensemble, where they exchange heat with the surrounding but not matter. And, finally, for the case of open systems, these are associated to the grand canonical ensemble, where both exchange of heat and matter with the surrounding is possible.

To approach the microcanonical ensemble, the SMC method, relies on the fact that all configurations with the same energy are equally probable. With that in mind, using a random sampling method, states are randomly generated, where accessible states are the ones with energy between E and $E + \delta E$ [75]. The probability P_i of finding the system in state i is then,

$$P_i = \begin{cases} P_0, & E < E_i < E + \delta E \\ 0, & Otherwise \end{cases} \tag{1.1}$$

On the canonical ensemble, it is usual to consider the system to be in contact with a

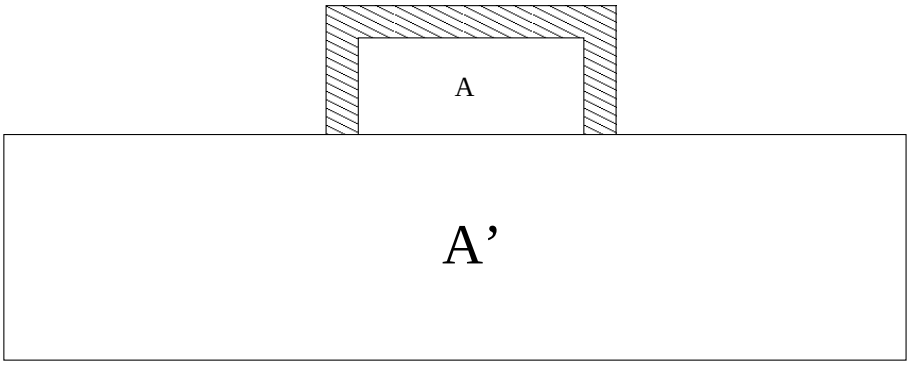

Figure 1.2: System A in contact with a heat bath A'.

heat reservoir like in Figure 1.2, where the system is A and the heat reservoir is A'. The condition of the size of system $A << A'$ must be fulfilled. The total energy of the system plus the heat reservoir is given by $E = E_{hb} + E_i$, where E_i is the energy of the state i and E_{hb} is the energy of the heat bath. The probability P_i of the system being in state i is then given by,

$$P_i = C\Omega\left(E - E_i\right), \tag{1.2}$$

where $\Omega\left(E - E_i\right)$ is the number of accessible states of the heat bath A', with energies around $E_{hb} = E - E_i$ (in the range of δE), and C is a constant obtained by the normalization condition $\sum_i P_i = 1$. One important feature is that $E_i << E$, however, in the function $\Omega\left(E - E_i\right)$, despite $E_i << E$, the therm E_i cannot be neglected since the argument of the function is rapidly varying [76]. So, performing a Taylor expansion of the logarithm of $\ln P_i$ in the neighborhood of the value $E_{hb} = E$ we obtain,

$$\ln P_i \approx \ln C + ln\Omega\left(E\right) - E_i \left(\frac{\delta \ln \Omega\left(E_{hb}\right)}{\delta E_{hb}}\right)_{E_{hb}=E}, \tag{1.3}$$

where, due to $E_i << E$, higher-order terms are neglected. Since the entropy definition is $S = k \ln \Omega$, then $\left(\frac{\delta \ln \Omega(E_{hb})}{\delta E_{hb}}\right)_{E_{hb}=E} = \beta$, where $\beta = \frac{1}{k_B T}$. The Boltzmann distribution is obtained as,

$$P_i = \frac{1}{Z} \exp\left(-\beta E_i\right), \tag{1.4}$$

where Z is the partition function.

On a SMC approach, to compute the expectation value of an observable $\langle O \rangle$, in the canonical ensemble, the quantity has to be averaged over all states with the Boltzmann distribution weight,

$$\langle O \rangle = \frac{1}{Z} \sum_i \exp\left(-\beta E_i\right). \tag{1.5}$$

If using a random sampling, the states need to be generated randomly, where relevant states are rarely encountered, which makes it a very inaccurate method. Consequently, another sampling method need to be used, which is called the importance sampling. This method generate states according to the Boltzmann distribution, where the observable value is sampled around the region of interest, which is a far more accurate method.

Markov Processes

The generation of states according to the Boltzmann distribution is not an easy task. The most used method is to reproduce the canonical ensemble behavior by naturally converging the system into equilibrium with states distribution of $\exp\left(-\beta E_i\right)$. To reproduce this behavior, the system has to evolve from state to state favoring a Boltzmann distribution. Consequently, the concept of Markov processes [77] has been considered. First order Markov processes, which are the ones more commonly used in SMC, have the peculiarity of when a state j is generated from a state i, the information about states prior to i do not improve the predictions about j. This way, the probability $W(i, t|j, t + \delta t)$ of transiting from state i to j at time t is not affected by previous transitions. To study a first order Markov process from i to j, one only needs to characterize the functions $P_i(t)$ and $W(i, t|j, t + \delta t)$ [78]. So, for the general Markov processes definition, the states are continuously distributed and the probability of being on the state j at time $t + \delta t$, is given by:

$$P_j(t + \delta t) = \int P_i(t) W(i, t|j, t + \delta t) di. \tag{1.6}$$

For a Markov processes approach, the first condition to be introduced is the ergodicity

condition, where every state is accessible from any other state, otherwise the system could be trapped in the first generated state [79].

To easily apply Markov processes to SMC, the concept of Markov chains is used. For that, states $i = 1, 2, 3, ..., N$ and time $t = n\delta t$ with $n = 0, 1, 2, ...$ are discretized. The time, here, is not the physical time, but rather a stochastic time, since at this point, for the study of equilibrium systems, the accurate dynamics are not relevant. So, applying the previous discretizations, Eq. 1.6 takes the form,

$$P_j(n+1) = \sum_{i=1}^{N} P_i(n) W(i, n|j, n+1), \tag{1.7}$$

where the transition probabilities must satisfy the condition,

$$\sum_{i=1}^{N} W(i, n|j, n+1) = 1. \tag{1.8}$$

Considering a time independent transition probability $W_{i,j}$ the Markov chain takes the form,

$$P_j(n+1) = \sum_{i \neq j}^{N} P_i(n) W_{i,j}. \tag{1.9}$$

where $W_{i,j}$ is a transition matrix.

From the concept of Markov chains, to better characterize the system, the Master Equation is introduced, where the rate of transition w_{ij} is considered instead of the transition probability. Taking into account a continuous time [13], the rate of change of the probability $P_j(t)$ is given by,

$$\frac{\delta P_j(t)}{\delta t} = \sum_{i=1}^{N} P_i(t) w_{ij} - \sum_{i=1}^{N} P_j(t) w_{ji}. \tag{1.10}$$

Detailed Balance

To achieve a steady state the Master equation takes the form,

$$\frac{\delta P_j(t)}{\delta t} = 0, \tag{1.11}$$

which leads to the relation between states given by,

$$\sum_{i=1}^{N} \left(P_i(t) w_{ij} - P_j(t) w_{ji}\right) = 0, \tag{1.12}$$

where a possible solution is the detailed balance,

$$P_i(t) w_{ij} = P_j(t) w_{ji}. \tag{1.13}$$

On the canonical ensemble, in contact with a heat bath, the system tend to an equilibrium with a temperature around the bath temperature. In equilibrium a Boltzmann distribution according to eq.1.4 [79] is obtained. When applying to SMC and taking into account the detailed balance condition, the ratio of transition rates is,

$$\frac{w_{ij}}{w_{ji}} = \frac{P_j(t)}{P_i(t)}. \tag{1.14}$$

For the distribution of eq.1.4,

$$\frac{w_{ij}}{w_{ji}} = \exp\left[\beta \left(E_i - E_j\right)\right], \tag{1.15}$$

we have now the possibility to implement a SMC algorithm with Markov chains corresponding to the proposed transition rates, which properly sample canonical systems.

Ising Model

To study equilibrium problems, the model that is traditionally considered is the Ising model. In short, a lattice is considered, with spins in each site. Spins interact with each other and can take values of ± 1. The Hamiltonian of the system takes the form,

$$H = -J \sum_{i,j} \sigma_i \sigma_j - B \sum_i \sigma_i, \tag{1.16}$$

where J is the interaction constant, σ the spin value, and B the applied magnetic field. Only nearest-neighbor interaction is taken into account, which can be a good approximation since dipole strength decline with $1/r^3$. The Ising model is usually used to study systems in contact with an heat bath (canonical ensemble), and it was primary used as a model of a magnet [80], however it has been consider, together with its generalized version given by the q-state Potts model [81], to study many problems. To apply the previous concepts of Markov chains and detailed balance, where transition rates are given by eq 1.14, an algorithm was introduced by Metropolis et al. [72], that takes into account these concepts for the packing of rigid spheres. In this algorithm, a spin is randomly choose in the lattice to flip, and the flipping of the spin is accepted with a probability given by,

$$w_{ij} = \begin{cases} \exp\left[\beta \left(E_i - E_j\right)\right] & , E_i < E_j \\ 1 & , Otherwise \end{cases} \tag{1.17}$$

What makes the Ising model so interesting and widely studied is the fact that, even without an applied field ($B = 0$), it presents a transition, varying the temperature (T). At $T = 0$, the spins are all aligned (either up or down, with equal probability), an ordered phase, and at $T = \infty$, all spins have random orientation, being in the disordered phase [82, 83]. In the thermodynamic limit there is a transition at a specific T_c where the system goes from the ordered to the disordered phase. This transition in T is a continuous phase transition.

1.1.2 Nonequilibrium Problems

In nature, equilibrium problems with no external perturbation rarely occur. Most systems present nonequilibrium characteristics [84], like a flux of particles or energy (in this thesis thin-film deposition or nano-clusters growth), external forces applied, or catalytic reactions (in this thesis ethanol electro-oxidation and carbon monoxide oxidation).

Nonequilibrium systems can be classified into two categories [85]: far-from equilibrium and out-of equilibrium. The category of far-from-equilibrium consists on systems going toward equilibrium, however with an initial perturbation or initial state far away from equilibrium. In out-of equilibrium, the system is intrinsically not in equilibrium, with a continuous external perturbation (for example, a temperature gradient [85], like it can be observed on Figure 1.3).

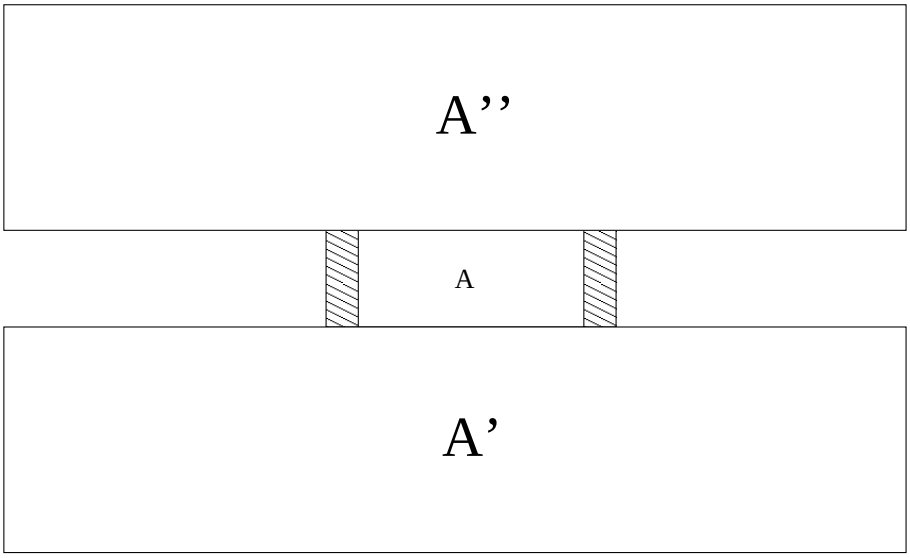

Figure 1.3: System A in contact with two heat baths A' and A''.

Steady States

Since most studies are applied to equilibrium systems, similarity with nonequilibrium systems needs to be found, which allows the application of the previously acquired knowl-

edge at equilibrium. This is where the concept of nonequilibrium steady states enters, since on a nonequilibrium system, for a constant perturbation, it can eventually find a steady state. The equilibrium state can be easily characterized without approaching the dynamics. In contrast, on the nonequilibrium steady state, the dynamics of how the system evolves to that steady state are relevant to the study of the system. These steady states can be obtained due to a stationary external perturbation, and differ from equilibrium due to fluxes of: energy, mass, charge, etc...[86]. Taking, again, the example of a system in contact with two heat baths (Figure 1.3), since it has local equilibriums with each of the heat baths, a gradient of temperature is formed. This leads to a constant heat flux and a nonequilibrium steady state occurs, where constant flux of energy is observed.

The advantage of equilibrium systems is that all states are accessible (ergodic principle), constant long-time properties of the system can be found, and an observable can be easily averaged with respect to the density of states. On the nonequilibrium counterpart, for simple steady state cases, the same fundamentals are applied [87], i.e., a steady state needs to be found, where, despite the dynamics, important properties remain constant, and it occurs, at least, during the range of experimental times.

Driven Lattice Gas

The Driven Lattice Gas model is a good example of a nonequilibrium system, since it is considered by many the "Ising model" of nonequilibrium. It presents a nonequilibrium steady state, and instead of a temperature gradient as in the example of a system in contact with two heat baths, a field is applied.

This model was introduced by Katz, Lebowtitz, and Spohn [88], to study a kinetic lattice gas, where particles are driven by a field ϕ. The configuration energy of a simple lattice gas particle σ is given by,

$$H_i = -J \sum_j \sigma_i \sigma_j, \tag{1.18}$$

where the sum is over the number of nearest neighbors. However, in this case, with the field applied in one direction, no hamiltonian is defined, which is an usual feature of nonequilibrium systems. In this model, with the applied field, detailed balance is broken by forbidding particles to jump against that same field. The rate of change over time of the state probability is also given by the master equation (Eq. 1.10). This model can be applied to a diversity of systems, from surface growth or pedestrian dynamics, to vehicular traffic flow.

SMC can be used in this model as a similar way as the Metropolis algorithm, where a pair of sites is randomly chosen, and if the first site is occupied, the particle jumps (if adjacent site empty), from i to j, with rate,

$$w_{ij} = \exp\left(-\beta\delta H + l\phi\right), \tag{1.19}$$

where δH is the energy change and $l = -1, 0, 1$ is the number of sites jumped along the field ϕ. This system also present a continuous phase transition as in the Ising model [66].

Reaction Models

Other nonequilibrium characteristics rely on the exchange of particles, like several models with adsorption, reaction, and desorption. These models lead to a flux of particles, in and out of the substrate, which can obtain a nonequilibrium steady state, that, in some cases, also lead to an ordered phase which is an adsorbing state.

Some of the first models, of this type, studied by Monte Carlo, were the reaction diffusion models, where reactants are already in the substrate and diffuse until reaction. Product desorption, or reactant coalescence occur after reaction. An example of these models is the diffusion-limited reaction model [89]. The rules of the model can be shown by,

$$\begin{aligned} A + A &\rightarrow 0 \text{ (Annihilation)} \\ A + A &\rightarrow A \text{ (Coalescence)} \end{aligned} \tag{1.20}$$

where A particles can coalesce or annihilate upon contact. This is a model with an adsorbing state where no more reactions occur. Other reaction models will be discussed in this thesis.

1.2 Kinetic Monte Carlo

One of the main limitations of the standard MC method is that too many transitions are rejected. This can occur because at low temperatures most transition attempts are rejected, or can also be due to the fact that the system is trapped on a steady state, where the relevant transitions to get out of it are infrequent. This can happen on both equilibrium states and nonequilibrium steady state. Another limitation of SMC is not having the proper time evolution, which is very important for nonequilibrium systems. In SMC, Monte Carlo steps are not real time increments, like in the Metropolis algorithm, where the steady state is the objective, each time step is only one attempt per site and not a rate based process. Consequently, the Monte Carlo method, needs proper rates to have an accurate time evolution. This is a great advantage of the kinetic Monte Carlo method (KMC), since the process choice is based on rates and the time increment is accurately computed.

At Equilibrium, where the system behavior is static, KMC is mostly useful to increase the simulation speed. Mainly, it is used as a rejection free scheme. Since dynamics are not important and parameters are usually averaged over time, there is no need for temporal analysis of observables. For nonequilibrium systems, in the other hand, the dynamical behavior is important, so if the proper transition rates are selected, as well as the proper list of events, then KMC accounts for the different time scales of processes.

One main property of KMC is that it can relate the time of the model with the physical time. This can occur if the rate of processes is experimentally known, like for the flux of deposition, the rates of diffusion, or the rates of reaction. To compute the time increment,

after knowing the rate w_i of a process i, the total rate of events needs to be found,

$$R = \sum_{i}^{N} n_i w_i, \tag{1.21}$$

where n_i is the number of events with rate w_i and N the total number of events. Then, taking into account the probability distributions, the time increment is given by [84],

$$\Delta t = -\frac{\ln(1-\tau)}{R}, \tag{1.22}$$

where τ is a random number in the interval $[0, 1[$.

In this section, we start by an approach to infrequent events, then the rate calculation through Transition State Theory is introduced, and we finalize with the KMC application to surface dynamics.

1.2.1 Infrequent Events

In KMC, understand and control of process rates is very important, since most of the time, the system dynamics are dominated by frequent events, which in several situations are far less relevant than the infrequent ones. Examples of frequent events are, for instance, ad-atom vibration during surface diffusion, or processes inside steady states with time scales much smaller than the ones for jumps out of these states. To be able to achieve, numerically, large time scales, it is necessary to group the frequent events, and control the dynamics through the infrequent events.

BKL Algorithm

As previously stated, the Metropolis algorithm has some limitations when dealing with the high rejection of transitions at low temperature or around the equilibrium state. To solve those limitations, an algorithm was proposed by Bortz, Kalos, and Lebowitz [90]. In this model, knowing the transition rate w_{ij} from state i to all states j at one step of

distance, a process is then chosen with a probability dependent on w_{ij}. For that, a line of transition rates is drawn and a random number generated between 0 and the sum of all transition rates. The time increment is given by eq.1.22. A difficulty on this scheme is the slow step of transition rate calculation, which, however, can be overcome by keeping a list of processes, where this list is updated after each transition. In the case of the Ising model, it is a small update due to the short nearest-neighbor interaction. For low transition acceptance ratio, this method is much more efficient than the simple trial and fail.

1.2.2 Transition-state-theory

As stated before, to compute the rates of processes for KMC, we can use experimental data, like flux of deposition or desorption, or the rates of diffusion and reaction. However, theoretically it is also possible to compute process rates, by using Transition-state-theory (TST) [91], which needs the values of activation energy and attempt frequency.

The use of TST has been widespread to solve problems from organic and inorganic chemistry, to solid-state physics or nuclear physics. The theoretical foundations behind TST started with Arrhenius, that empirically related the reaction rate with the inverse of the temperature. The relation,

$$k = \nu \exp\left(-\beta E_a\right), \tag{1.23}$$

where E_a is the activation energy and ν the prefactor, was found. Since the beginnings of this theory, three main areas have been developed [92]: The thermodynamic treatment, the kinetic theory treatment, and the statistical mechanics treatment. All this approaches are combined into TST.

Transient State Approximation

One essential feature of TST is the fact that the transition from state i to state j goes through an intermediate point (Figure 1.4), and this point lies at a saddle point in the energy landscape. The system in state i is considered in equilibrium with the system at the saddle point, which allows equilibrium calculations of transition rates between the initial state i and the intermediate state. The details of previous transitions are irrelevant in the rate calculation, since the system has time to thermalize between transitions, in the limit of sufficiently deep basins.

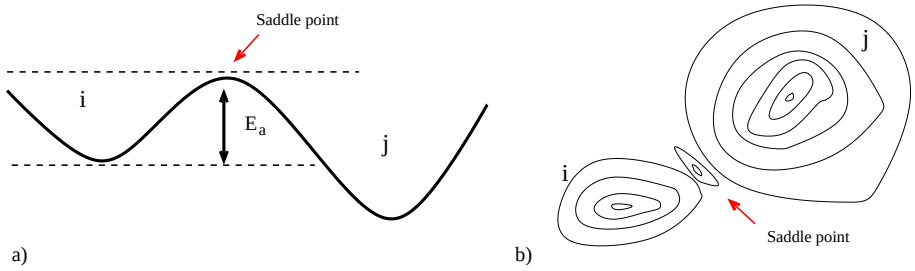

Figure 1.4: Transition state theory illustration with a) the energy barrier and b) the potential energy surface with the saddle points.

Harmonic Approximation

For the rate calculation, an approximation of the harmonic potential [93] needs also to be done. It is a good approximation for solids. The harmonic approximation around minima and saddle points is used to compute the transition rate prefactor. For a system with N minima with harmonic vibrational modes, the rate is given by,

$$k = \frac{\prod_i^{3N} \nu_i^{min}}{\prod_i^{3N-1} \nu_i^{sad}} \exp\left(-\beta E_a\right), \tag{1.24}$$

where ν_i^{min} and ν_i^{sad} are the normal mode frequencies at the minimum and the saddle point. This approximation rejects the usually used prefactor of $k_B T/h$ in TST.

The harmonic approximation has some limitations, like, high temperatures (near the

melting point) for solids, transient mobility that can exist due to low barriers in surface diffusion, or also the effect of anharmonic terms in the potential well.

1.2.3 Adatoms Surface Dynamics

As stated before, the Kinetic Monte Carlo method is useful for processes of reaction, evaporation, and diffusion. We will now focus on ad-atom surface diffusion, as a simple example of KMC use. For the TST application, the rates are also computed through the Arrhenius equation (Eq. 1.23), since ad-atom diffusion has also the characteristic of having energy barriers larger than thermal energy k_BT, where successive hops are uncorrelated. This can be observed on the scheme of Figure 1.5.

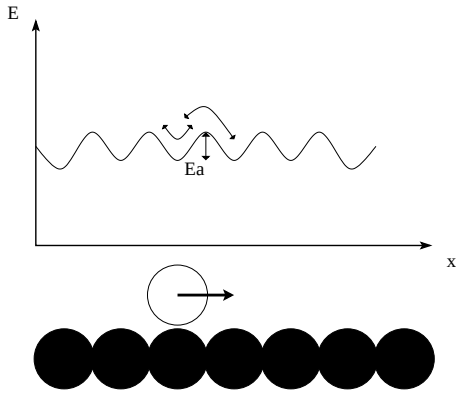

Figure 1.5: Adatom diffusion scheme with energy barriers.

The advantages of kMC, in this case, rely on the fact that it describes a time evolution that can be compared with experiments. It also avoid attempts to move particles trapped in immovable positions, and deal with the infrequent events of low temperature diffusion and adatoms in stable positions.

Barriers and Rates

When using TST, we need the activation energy of each process and the attempt frequency (prefactor in Eq. 1.23). The activation energy takes into account the attractive

potential between particles, which depends on local configuration and will rely on the number of neighbors.

The activation barriers can be calculated using experimental data, where each neighbors configuration has a different activation energy. In a square lattice, for instance, 10 neighbors are nearest or next-nearest neighbors (see Figure 1.6), which can have 1024 different configurations, however, can be reduced to 241 through symmetry and other approximations [84].

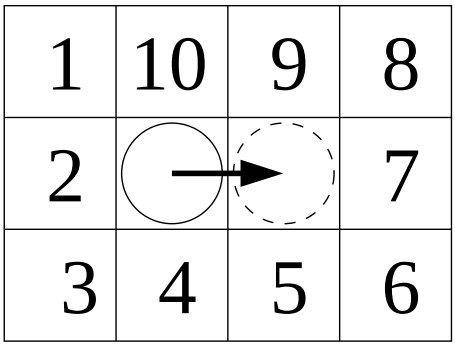

Figure 1.6: Nearest and next-nearest neighbors in a square lattice for a diffusion hop.

To solve the issue of having a large number of configurations to track, we can calculate the activation energy through neighbor counting and by using the interaction energy of pairs of atoms. Usually, the number of initial nearest-neighbors n_0 is used, and the activation energy is,

$$E_a = E_m + n_0 J_{pp}, \tag{1.25}$$

where E_m is the diffusion activation energy and J_{pp} the particle-particle interaction energy. We can also use the difference of nearest neighbors between the initial and final position (which will be presented in this thesis), where it is even possible to introduce the counting of next-nearest neighbors, but with a different interaction energy.

The attempt frequency is also important, since it sets the overall time scale of the ad-atoms movement. It depends on various factors, including the local neighbors of the ad-atom, however it is much less dependent on the neighbors than the activation energy.

For that reason it is most of the time considered constant, and can take values around 10^{11} and 10^{13} Hz.

1.3 Molecular Dynamics

The computational method of molecular dynamics (MD) is very efficient at the molecular scale, but can also be used at larger length scales. This is a technique used to obtain the dynamics of many bodies systems, by solving the equations of motion of all particles. It proceeds the work where analytical studies fail since, in general, a system with more than two interacting bodies is, in practice, not solvable. It relies on the interatomic potentials to solve the equations of motion.

On the Monte Carlo approach, the important sampling method forces the production of states with the Boltzmann distribution, and it is also necessary to discretized the phase-space into different states, which is computationally very efficient. On the other hand, the MD approach operates in a less discretized phase space, which can model unpredictable effects like lattice reorganization or unexpected atomistic cooperative phenomena.

The applications of MD [14] are varied, like fundamental studies, fluid dynamics, polymers, solids, and biomolecules.

In this section we start by exploring the method, then describe the technique implementation, and finally present some physical aspects and approximations of particles interaction.

1.3.1 Dynamics

To implement MD, the equations of motion need to be solved. For each specific type of system, a different formulation for the equations of motion can be used [14]. Equations of motion relying on Newton's formulation are usually used for free atoms with interaction.

Using Cartesian coordinates $\mathbf{r}_i$ at particle i the equation of motion is,

$$\ddot{\mathbf{r}}_i = \frac{\mathbf{f}_i}{m}, \tag{1.26}$$

where the force $\mathbf{f}$ is computed over all interactions, and m is the mass.

The Lagrange formulation for the equations of motion is a more useful notation, on specific cases, like systems with constrains. Generalized coordinates $\mathbf{q}_1$,$\mathbf{q}_2$,$\mathbf{q}_3$,...,$\mathbf{q}_n$ with n degrees of freedom are used, where the Lagrangian $\mathbf{L}(\mathbf{q}, \dot{\mathbf{q}})$ is defined as the difference between kinetic and potential energy, which depends on the coordinates and on the velocities. For a conservative system it is,

$$\frac{d}{dt}\left(\frac{\delta \mathbf{L}}{\delta \dot{\mathbf{q}}_i}\right) - \frac{\delta \mathbf{L}}{\delta \mathbf{q}_i} = 0 \tag{1.27}$$

where $i = 1, 2, 3, ..., n$. When using Cartesian coordinates, it takes the form of Newton's equations of motion.

Hamilton equations of motion, in turn, use a generalized momentum $\mathbf{p}_i$ of the coordinates $\mathbf{q}_i$, which relate with the Lagrangian formulation as,

$$\mathbf{p}_i = \frac{\delta \mathbf{L}}{\delta \dot{\mathbf{q}}_i}. \tag{1.28}$$

The Hamiltonian is then,

$$H(\mathbf{q}, \mathbf{p}) = \sum_i \dot{\mathbf{q}}_i \mathbf{p}_i - L(\mathbf{q}, \dot{\mathbf{q}}), \tag{1.29}$$

which is useful for systems where the momentum can be conserved.

Force Calculation

An important aspect of MD, is the force calculation, which is used on the equations of motion. Taking into account Newton formulation, the force applied on an atom i, subject

to an interaction potential $V(\mathbf{r}_{ij})$ with other atoms j, and an external potential $U(\mathbf{r}_i)$ is,

$$f_i = -\nabla U(\mathbf{r}_i) - \sum_j \nabla V(\mathbf{r}_{ij}). \tag{1.30}$$

To increase computational efficiency, a cutting distance r_c is included, where $|\mathbf{r}_{ij}| \leq r_c$.

Different algorithms of the implementation of interactions [14] can be used. We can test all pairs of particles however, having no knowledge if the particles are inside the cutting distance r_c or not. It is a less efficient method. We can use the method of dividing the system into cells with edges larger than r_c. Here, particles in the r_c radius are known to be in the same or neighbor cells, which reduces the computational effort. Another efficient method is to keep a list of neighbors over several time steps, however it is necessary to use a larger distance than r_c, which will depend on the time step and the velocity of particles.

1.3.2 Integration Methods

After the force calculation, it is necessary to integrate the equations of motion. To solve these ordinary differential equations, the numerical methods of finite difference are used, which consist on integrating the equations of motion in the limit of small time increments δt. There is a large amount of finite difference methods available [94], like the Euler and Picard methods, the Runge-Kutta method, or others more accurate described next.

The efficiency of the integration methods on Molecular Dynamics is very important. It has to be less time consuming than force calculation, since force calculation is the less efficient part of MD, so MD time should not be limited by the integration methods. Summarizing, desirable qualities of the integration method [25] are being computationally fast, use long δt, have a small deviation to the classical trajectory, conserve energy and momentum, and be time-reversal.

The most used integration methods are the Verlet and Leapfrog methods, which are algebraically equivalent. A less effective but more precise one is the Predictor-corrector

method.

Verlet and Leapfrog Algorithm

We present now the derivation of the Verlet Algorithm, by starting with a Taylor expansion about $\mathbf{r}(t+\delta t)$ in the neighborhood of t, as

$$\mathbf{r}(t+\delta t) = \mathbf{r}(t) + \delta t\dot{\mathbf{r}}(t) + \left(\frac{\delta t^2}{2}\right)\ddot{\mathbf{r}}(t) + ... \tag{1.31}$$

Adding the previous equation to the Taylor expansion about $\mathbf{r}(t-\delta t)$ in the neighborhood of t,

$$\mathbf{r}(t+\delta t) = 2\mathbf{r}(t) - \mathbf{r}(t-\delta t) + \delta t^2\ddot{\mathbf{r}}(t) + ... \tag{1.32}$$

where the therm in $\dot{\mathbf{r}}(t)$ (velocity) cancels out. The motion only depends on the previous position and on the force calculation. The velocity is then computed subtracting the previous Taylor expansions and takes the form,

$$\dot{\mathbf{r}}(t) = \frac{\mathbf{r}(t+\delta t) - \mathbf{r}(t-\delta t)}{2\delta t}. \tag{1.33}$$

On the case of the Leapfrog Algorithm, we start the derivation by choosing an intermediate $\frac{\delta t}{2}$ time increment for the integration. Then subtracting the Taylor expansion of $\mathbf{r}(t)$ in the neighborhood of $t+\frac{\delta t}{2}$ to the expansion of $\mathbf{r}(t+\delta t)$ in the neighborhood of $t+\frac{\delta t}{2}$ we have,

$$\mathbf{r}(t+\delta t) = \mathbf{r}(t) + \delta t\dot{\mathbf{r}}\left(t+\frac{\delta t}{2}\right). \tag{1.34}$$

To solve Eq. 1.34, the velocity needs to be computed. So, we apply the Taylor expansion to $\dot{\mathbf{r}}\left(t+\frac{\delta t}{2}\right)$ and $\dot{\mathbf{r}}\left(t-\frac{\delta t}{2}\right)$ obtaining,

$$\dot{\mathbf{r}}\left(t+\frac{\delta t}{2}\right) = \dot{\mathbf{r}}\left(t-\frac{\delta t}{2}\right) + \delta t\ddot{\mathbf{r}}(t). \tag{1.35}$$

This method is then applied to the measurements of position and velocity at different

times.

Both Verlet and Leapfrog methods are subject to uncertainty due to the truncation of the Taylor expansion. To improve the accuracy, the use of a small δt, which reduces the error in the expansions, is recommended.

Predictor-Corrector Algorithm

The main idea of this method is to predict the next time step variables using the actual time, and then correct the variables using the new positions. We can start with a Taylor expansion of each $\mathbf{r}(t+\delta t)$, $\dot{\mathbf{r}}(t+\delta t)$ and $\ddot{\mathbf{r}}(t+\delta t)$ around t (see Eq. 1.31 for the positions). Other methods like Euler, Verlet, or Leapfrog can be used. Since the values are not precise enough due to the Taylor expansion truncation, these predicted values are then corrected. For that, the values of acceleration using the new positions are computed. The error between the predicted and corrected acceleration is estimated as,

$$\Delta\ddot{\mathbf{r}}\,(t+\delta t) = \ddot{\mathbf{r}}_c\,(t+\delta t) - \ddot{\mathbf{r}}_p(t+\delta t). \tag{1.36}$$

Then, including this error into the predicted variables, we have,

$$\begin{aligned}
\mathbf{r}_c(t+\delta t) &= \mathbf{r}_p(t+\delta t) + \alpha_1\Delta\ddot{\mathbf{r}}(t+\delta t)\\
\dot{\mathbf{r}}_c(t+\delta t) &= \dot{\mathbf{r}}_p(t+\delta t) + \alpha_2\Delta\ddot{\mathbf{r}}(t+\delta t)\\
\ddot{\mathbf{r}}_c(t+\delta t) &= \ddot{\mathbf{r}}_p(t+\delta t) + \alpha_3\Delta\ddot{\mathbf{r}}(t+\delta t)
\end{aligned} \tag{1.37}$$

where the coefficients $\alpha_1, \alpha_2, \alpha_3, ...$ are chosen to optimum accuracy [25]. After the correction, other variables of interest can be computed.

On what concerns applicability and efficiency, this method is less efficient than the previous ones, since it needs to be corrected and can have more than one correction iterations to increase accuracy. However, it is more accurate than other methods, depending on the number of corrections.

1.3.3 Particles Interaction

One of the most important parameters in MD is the potential, since it is necessary for the force calculation (see Eq. 1.30). It can depend on aspects like, external potentials (electric or magnetic fields), or even walls of a container, but also depends on particles interaction, like van der Walls and electrostatic interactions, or covalent bonds.

We will mainly focus on particles interaction, since they can depend on pairs, triplets, or more interacting particles. Pair potentials are mainly used in atomistic systems (gases), and other potentials, like many-body potentials are used in metallic systems. In molecules, constrained dynamics are usually applied.

Pair Potentials

The simplest forms of pair potentials are the hard sphere and soft sphere potentials. The hard sphere potential, that can be seen on Figure 1.7a), is considered as an infinite barrier at the radius of the particle r_{min}, and has the form,

$$V_{hs}(r) = \begin{cases} \infty & r < r_{min} \\ 0 & r \geq r_{min} \end{cases} \tag{1.38}$$

The soft sphere potential, seen on Figure 1.7b), is a potential that increase progressively to infinite with the decreasing of r. It takes the form,

$$V_{ss}(r) = cr^{-\nu}, \tag{1.39}$$

where c is a constant, and the potential become less soft with the increase of ν. In the limit of large ν, it becomes an hard sphere potential with $r_{min} = 1$. These simple potentials have only a repulsive part, which cannot reproduce real phases, since the solid phase is reproduced by compact packing and, both liquid and gas phase, cannot be distinguished.

With the inclusion of an attractive part on the pair potential comes the Lennard-Jones potential, which is observed in Figure 1.7c). It has both an attractive and repulsive

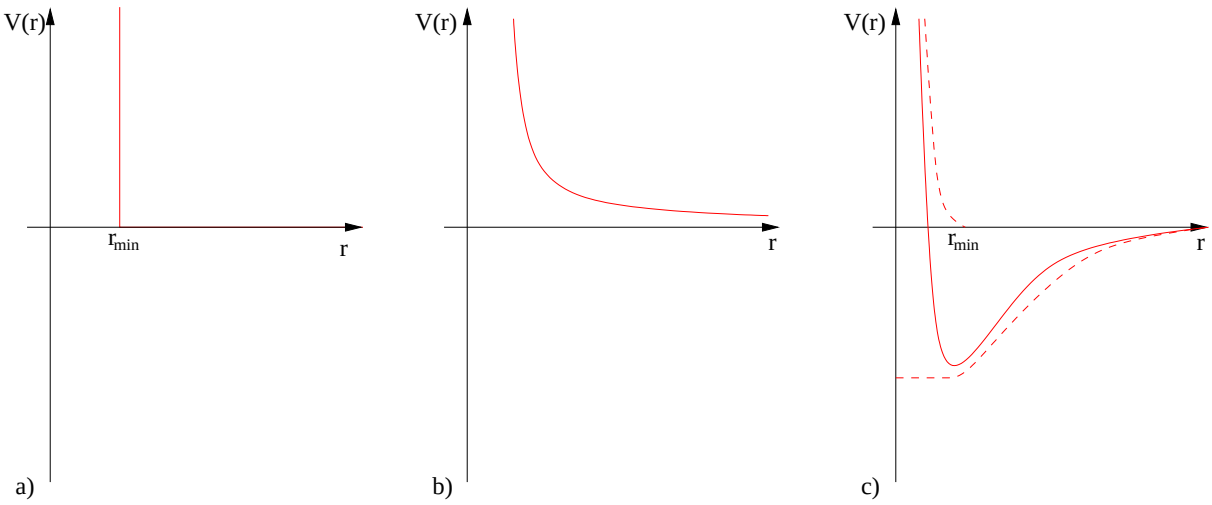

Figure 1.7: Pair potentials of a) Hard sphere, b) Soft sphere, and c) Lennard-Jones.

component, where the repulsive component come from the nucleus repulsion, and the attractive one from the Van der Walls interaction. It was first used for Argon atoms [95], and takes the form of,

$$V_{LJ}(r_{ij}) = 4\epsilon \left[\left(\frac{\sigma}{r_{ij}} \right)^{12} - \frac{1}{2} \left(\frac{\sigma}{r_{ij}} \right)^{6} \right] \tag{1.40}$$

where ϵ and σ are constant parameters specific of the system under study. This potential can reproduce the solid-liquid and liquid-gas transitions.

Other Interactions

Other type of interactions have to be taken into account, and treated differently. The case of interatomic interactions in molecules, where covalent bonds exist, the high vibrations frequency can be computationally demanding. One method to solve these issue, is by introducing constrains, where the length of atom bonds is kept constant, as we can see on Figure 1.8, with the bonds 1-2 and 2-3 that have a constrain of fixed length. Some constrains can also be applied to angles between bonds, which is possible by only including a constrain of a fixed length on two atoms, for instance, in Figure 1.8 the distance 1-3 can

be fixed.

After the intramolecular constrains, for the intermolecular interactions, regular potentials can be used between atoms of different molecules. The potential is calculated for pairs between all atoms in the different molecules, except for pairs with a fixed bond. For instance, the Lennard-Jones potential can be applied to diatomic non-polar molecules. In the specific case of simulating polar molecules, the inclusion of fictional charges in the molecule can be used [25].

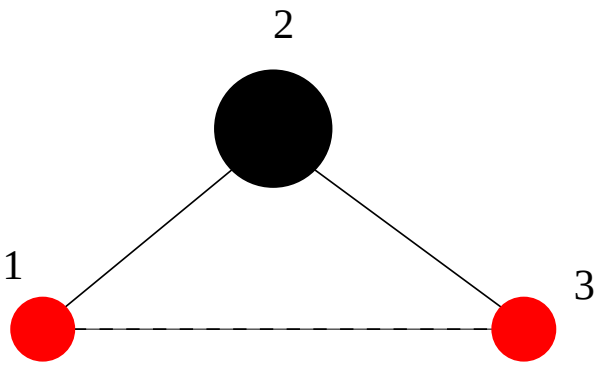

Figure 1.8: Molecule with 3 atoms and 2 bonds.

Also many-body interactions [14] must be taken into account, since pair potentials can fail to reproduce known effects. In these cases, the relative position of atoms is important, like in some crystalline structures that prefer an alignment of more than two atoms. An attempt to address this problems is by the inclusion of a third body interaction. However, in the case of metals, valence electrons are shared between atoms, so the use of potentials that include electrons density is necessary. A commonly used potential is the embedded-atom potential (EAM) [96], which is divided in two parts: the pair interaction and the electronic density dependent interaction.

1.4 Accelerated Molecular Dynamics

Despite being an useful method, MD present some limitations. For instance, the accessible simulation time is short, and even parallelization do not reduce it, since it is only useful to obtain larger system sizes. Also systems dominated by infrequent events (shown in section 1.2), present difficulties to the use of MD.

For those reasons, Accelerated Molecular Dynamics methods have been developed. A large development during the last decade has been done at the Los Alamos National Lab [54, 97], where some of these accelerated methods also use the TST approximation. Other methods like on-the-fly kMC can also be used [98] to study complex systems with complex energy landscapes.

In this section, a detailed description of the Temperature Accelerated Dynamics method will be made. Some other methods used in the literature, like Parallel Replica and Hyperdynamics will also be presented.

1.4.1 Temperature Accelerated Dynamics

The Temperature Accelerated Dynamics (TAD) method has been developed to deal with the problem of infrequent event dynamics on regular MD. For that, it is also based on the assumption of Harmonic Transition State Theory (HTST). The main characteristic of this method is that it uses the raising of the temperature to find transitions, then the ratios of the processes rates are changed for the original temperature, assuming HTST, and the proper transition to take place at the lower temperature, is selected.

Time Distribution

The first step of TAD is to understand the time distribution. Applying first-order kinetics for an infrequent-event system, the probability distribution of the time spent in

a state before a particular transition is given by,

$$f_i(t)dt = k_i e^{-k_i t} dt, \tag{1.41}$$

where k_i is the rate for the transition to occur, and $e^{-k_i t}$ is the rate for the transition i not occurring during the time t [99]. The value of k_i is given from HTST by the Arrhenius expression,

$$k_i = \nu_i e^{-\beta E_{a_i}}, \tag{1.42}$$

in which ν_i is the prefactor, $\beta = \frac{1}{k_B T}$ and E_{a_i} is the activation energy.

Basin-Constrained Molecular Dynamics (BCMD)

The second step is for the detection of the transition, and for that the Molecular Dynamics trajectory is confined to the potential energy basin. When the system tries to escape to another state, a transition is detected and it is reflected back to the original state. For each detected transition i, the escape time t_i and the activation energy E_{a_i} are computed, the latter using, for example, the Nudged Elastic Band Method (NEB) [100]. A BCMD simulation is performed at a high temperature to find the transition pathways and escape times. It is obvious that at the original temperature, the first escape time is always the correct one. However, in the case of an increased temperature, it is necessary to generate correctly distributed waiting times, to be mapped for the original temperature.

It is first necessary to relate the escape times at high temperature with the escape times at low temperature. For that we start with two temperatures T_{low} and T_{high}, each one with an escape time t_{low} and t_{high}. Knowing that the rate constant for T_{low} and T_{high} are k_{low} and k_{high}, we can relate the different escape times as,

$$k_{low} T_{low} = k_{high} T_{high}, \tag{1.43}$$

since $f(t)dt = ke^{-kt}dt$, for $x = kt$ the distribution is given by $f(x)dx = e^{-x}dx$, we can

rewrite Eq. 1.43 using Eq. 1.42 as,

$$t_{i,low} = t_{i,high} e^{E_{a_i}(\beta_{low} - \beta_{high})}. \tag{1.44}$$

With Eq. 1.44 it is possible to simulate the system at high temperature, and still obtain the correct activation energy, and is also possible to compute the escape time at T_{low}.

Time Stopping at High Temperature

After some time of performing BCMD, it is necessary to stop the MD simulation. So, the simulation has to be stopped when there is confidence that no other transition will occur at T_{low} after that time, except for a small probability δ. To understand the method employed to find the time to stop at a high temperature, the scheme of Figure 1.9 is used.

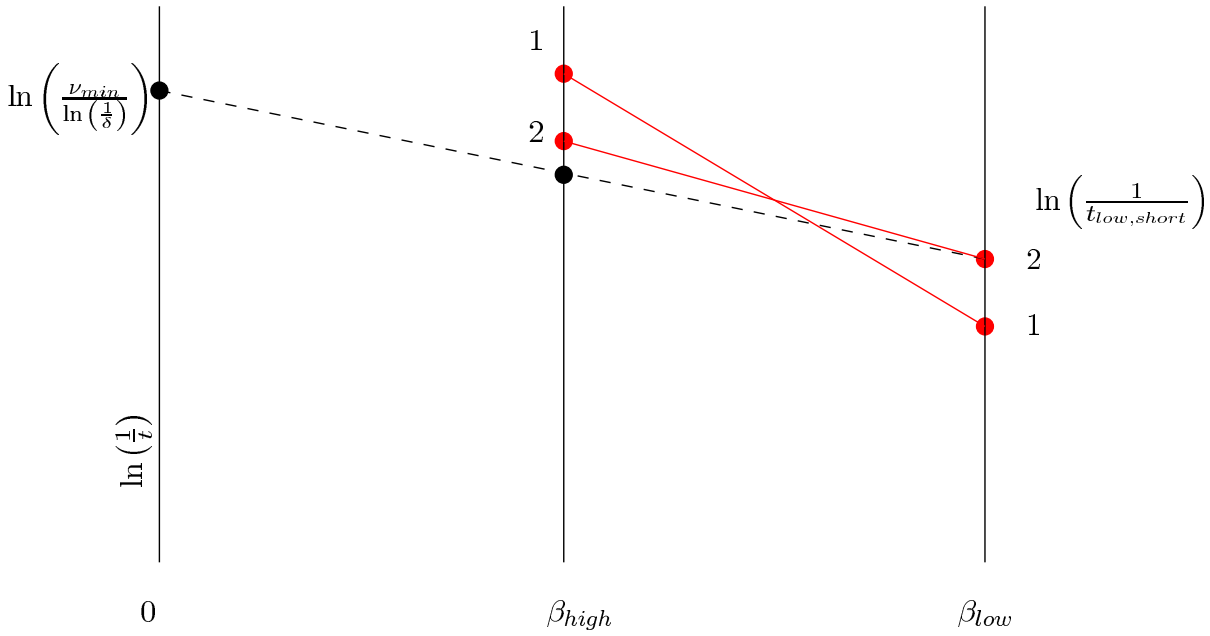

Figure 1.9: Scheme of the TAD method stopping time.

It is possible to see that a transition that happens at shorter time at T_{high} can occur at longer times at T_{low}, depending on the activation energy represented by the slope of the lines in the plot of Figure 1.9. To find the stopping time at T_{high}, a line, with a slope

lower, as can be seen on the dashed line in Figure 1.9, has to be drawn. This means that, using Eq. 1.44, for the transition to occur at a time longer than $t_{high,stop}$, it is necessary an activation energy lower than,

$$E_a = \frac{\ln\left(\frac{t_{low,short}}{t_{high,stop}}\right)}{\beta_{low} - \beta_{high}}. \tag{1.45}$$

Integrating Eq. 1.41 from $t_{high,stop}$ to infinity, we know that the probability is δ, which is the probability of a transition to occur after $t_{high,stop}$, which gives,

$$\ln\left(\frac{1}{\delta}\right) = k_{high} t_{high,stop}, \tag{1.46}$$

and replacing with Eq. 1.42 and 1.45, the final result to compute $t_{high,stop}$ is obtained as,

$$t_{high,stop} = \frac{\ln\left(\frac{1}{\delta}\right)}{\nu_{min}} \left(\frac{\nu_{min} t_{low,short}}{\ln\left(\frac{1}{\delta}\right)}\right)^{\frac{\beta_{high}}{\beta_{low}}}, \tag{1.47}$$

where the parameters ν_{min} and δ are chosen to ensure that an incorrect transition time is rarely obtained. ν_{min} is the lower bound on possible prefactors of the system. It is chosen to be able to compute $t_{high,stop}$ in a quantifiable way. If ν_{min} is chosen too high, it increases the uncertainty on the acceptance of a correct transition. If it is too low, the certainty on the correctness of the transition is improved, however the computational efficiency is largely reduced.

A more strict condition to stop the MD at T_{high} is introduced, as can be observed in the scheme of Figure 1.10. For an event to occur at a time higher than $t_{high,1} + \Delta$, the activation energy E_i should obey to the condition,

$$e(t_{high,1} + \Delta) \leq E_i \leq E(t_{high,1} + \Delta), \tag{1.48}$$

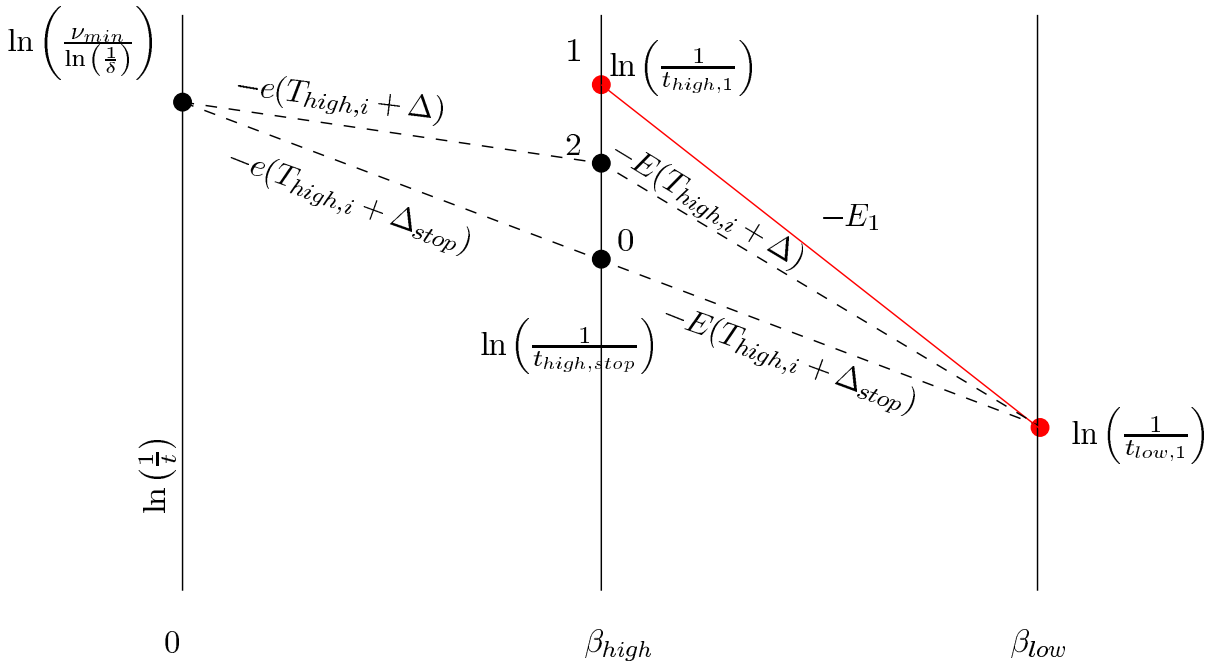

Figure 1.10: Scheme of the stop condition to the TAD method stopping time.

where,

$$e(t_{high,1}+\Delta)=\frac{\ln\left[(t_{high,1}+\Delta)\frac{\nu_{min}}{\ln\delta}\right]}{\beta_{high}}, \tag{1.49}$$

and,

$$E(t_{high,1}+\Delta)=\frac{\ln\left[\frac{t_{high,1}}{t_{high,1}+\Delta}\right]}{\beta_{low}-\beta_{high}}. \tag{1.50}$$

As the BCMD proceeds, the limits of Eq. 1.48 approach, until they reach,

$$e(t_{high,1}+\Delta_{stop})=E(t_{high,1}+\Delta_{stop}), \tag{1.51}$$

where $t_{high,1}+\Delta_{stop}=t_{high,stop}$, leading to the same result of Eq. 1.47, using Eq. 1.49 and 1.50.

Revisiting States

A new TAD procedure has been developed to increase the efficiency of the method [101]. This new TAD takes advantage of the fact that a state can be revisited more than once. However, it can be explain by the same type of scheme as before, which can be seen in Figure 1.11.

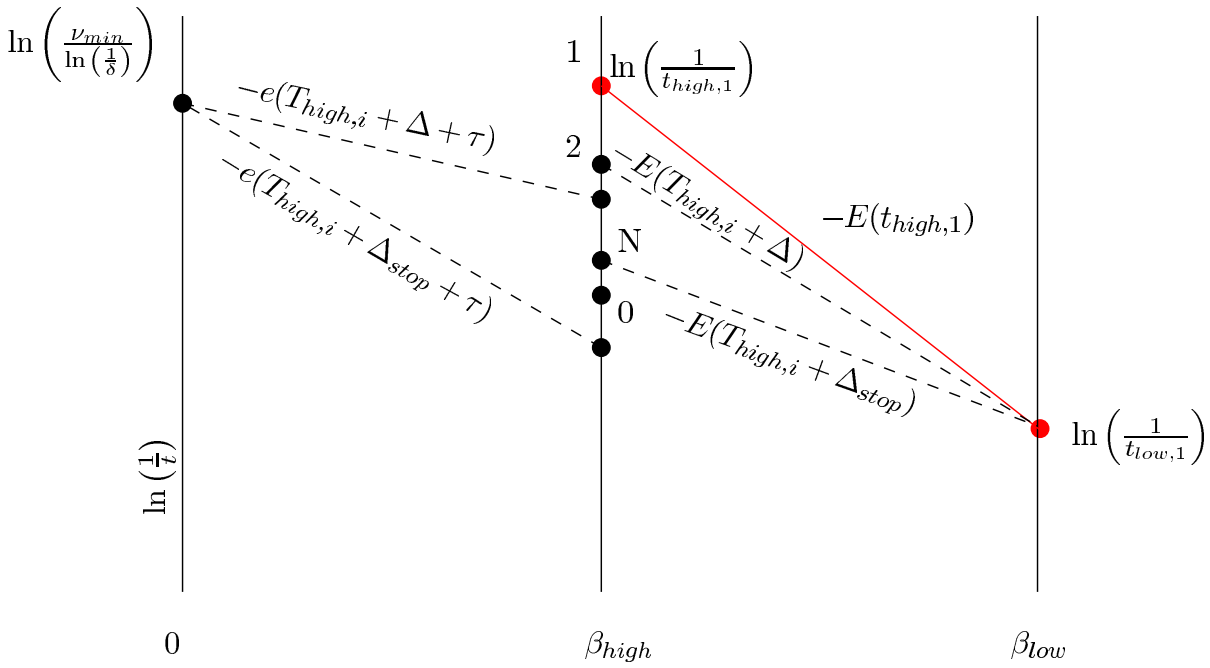

Figure 1.11: Scheme of the TAD method stopping time with revisiting states.

The procedure is as follows, after $t_{high,1}$ and finding a transition, it is still possible to say that the upper bound for the energy is $E(t_{high,1})$. Now, since a time τ has run in previous visits to the state, the lower bound energy can be calculated as $e(t_{high,1}+\Delta+\tau)$, i.e., the minimum energy of previously found transitions is given by,

$$e(t_{high,1}+\Delta+\tau) = \min\left[E_{min}, \frac{\ln\left[(t_{high,1}+\Delta+\tau)\frac{\nu_{min}}{\ln\delta}\right]}{\beta_{high}}\right]. \tag{1.52}$$

Knowing the lower bound energy, in the same way, the time to stop can be refined since,

$$e(t_{high,1} + \Delta_{stop} + \tau) = E(t_{high,1} + \Delta_{stop}), \tag{1.53}$$

and after a larger number of passages into the same state, the $t_{high,stop}$ starts to decrease. Using Eq. 1.49, the value of τ for the E_{min} converge to,

$$\tau = \frac{\ln\left(\frac{1}{\delta}\right)}{\nu_{min}} \exp\left(E_{min}\beta_{high}\right). \tag{1.54}$$

When $t_{high,stop}$ reaches a minimum value, it is possible to say, that E_{min} is the lowest energy possible, except for a probability δ. So, the $t_{high,stop}$ can just be computed, from that moment on, after a transition is found at T_{high}, by,

$$t_{high,stop} = T_{high} \exp\left(\frac{E_i - E_{min}}{\beta_{low} - \beta_{high}}\right), \tag{1.55}$$

since the T_{low} remains the same.

Synthetic Mode

One major limitation of the TAD method is also the existence of very frequent events, which occur often in realistic systems. An example is a system trapped in a super-basin, where only fast transitions between the same group of basins occur, and the activation energies are low when compared to the barrier to leave the super-basin. These low barrier processes slow the simulation time of TAD, since most of the time is spent doing the same transitions between the same states.

To solve this limitation, the synthetic mode was introduced [53]. It consists on keeping the history of the BCMD, i.e., keeping data of the MD at high temperature, every attempt out of the states, and the total time spent inside the state. A first step is to estimate attempt frequency, which can be done after a high number of attempts of the same path, where the ratio of the number of attempts and the total time spent in the state is used to

compute the attempt frequency at high temperature. Then, it is extrapolated from high to low temperature as,

$$\nu_{low,i} = \nu_{high,i} \exp\left[-E_a(\beta_{low} - \beta_{high})\right]. \tag{1.56}$$

When entering the synthetic mode, there is no more need for MD, since waiting times are generated through the exponential distribution of Eq. 1.41. Then, a list of synthetic and non-synthetic transitions is used, and MD is stopped until the non-synthetic transition time arrives. This method can be considered as some kind of KMC.

1.4.2 Other Methods

Other AMD methods have been used to address infrequent events [97, 102, 103]. We will focus on two methods: Parallel Replica [97] and Hyperdynamics [102].

Parallel Replica

Parallel Replica address the same problem than TAD of infrequent events, and use similar concepts of first-order kinetics, escape time given by Eq. 1.41, and TST.

Since this method also resorts on TST then, successive transitions are uncorrelated, time of the transition is brief, and waiting-time inside basins are long, which gives time to thermalize. The objective in this method is the parallelization of the BCMD, where the basin dynamics are spread over multi-processors, and each processor has a different trajectory generated. The first processor that finds the transition is chosen, and all other parallel MD are stopped. The schematic of this method can be seen on Figure 1.12. An important aspect is that all the time spent in each parallel attempt is added to the total time, except time spent on replicating the system, lag of the replicas, and time after the transition to allow recross or follow-on transitions. This characteristic indicates that the processors can be heterogeneous.

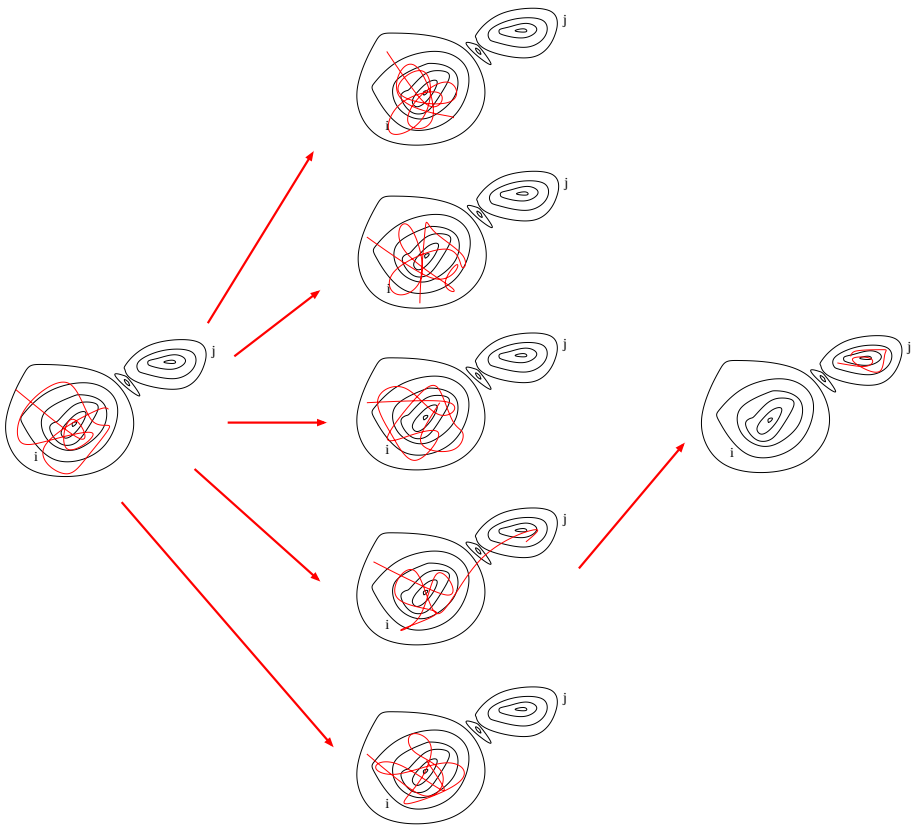

Figure 1.12: Scheme of the Parallel replica method.

Hyperdynamics

Hyperdynamics is a method that has also the same assumption of TST, but does not need to assume HTST. It addresses the infrequent events problem and the lack of previous knowledge of the transitions in the system.

This method consists on the inclusion of a bias potential $\Delta V_{bias}(\mathbf{r})$. This potential needs to have the ability of still obeying to TST, must be zero in the saddle points, and non-negative. A schematic of the method is presented in Figure 1.13, which can be computed by different ways [104]. The trajectory escapes from a state are increased, since the inclusion of a bias in the basin potential reduce the transition activation barrier, which

increases the rate of transition. However, the relation between transitions is constant, as

$$\frac{k_{A\to B}}{k_{A\to C}} = \frac{k_{A_{bias}\to B}}{k_{A_{bias}\to C}} \tag{1.57}$$

since the potential bias is the same in $A \to B$ and $A \to C$. The time is boosted by a factor of $\exp(\beta\Delta V(\mathbf{r}))$, being the total time t_{hyper} after N integrations given by,

$$t_{hyper} = \sum_{i=1}^{N} \Delta t_{MD} \exp(\beta\Delta V(\mathbf{r}_i)) \tag{1.58}$$

where Δt_{MD} is the regular MD time interval.

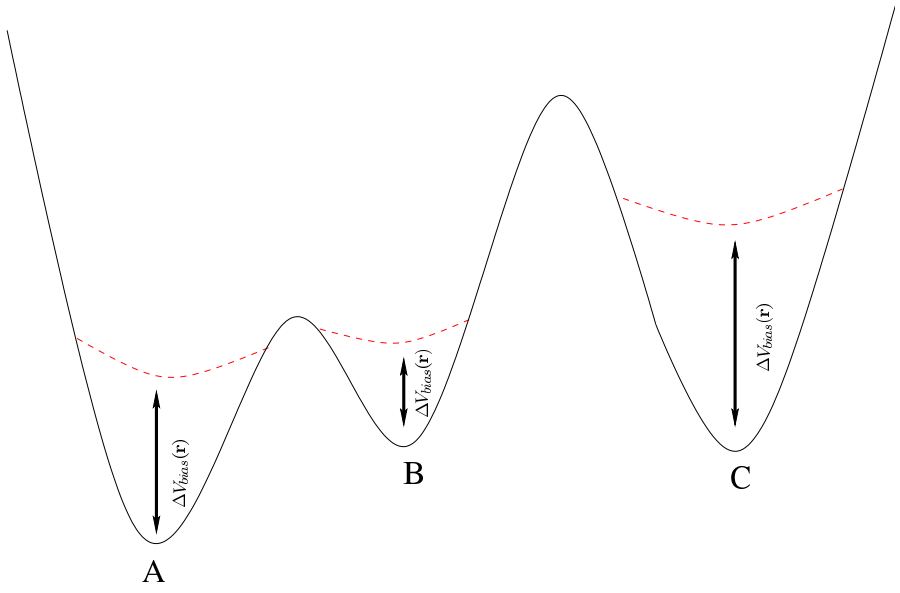

Figure 1.13: Scheme of the hyperdynamics method.

The limitations of this method are mainly that the potential bias need to be carefully chosen and that the computation of the potential can take longer times.

Chapter 2

Substrate deposition with reaction

In this chapter, we focus on surface deposition, however, we allow the possibility of reaction upon adsorption. This type of studies are of fundamental application to heterogeneous catalysis. Here, we consider two different type of models. One with adsorption and reaction, but without desorption, and the other with product desorption upon reaction. The first model is applied to ethanol electro-oxidation, which will boil into a generalized version of the random sequential adsorption model. The second model, called the Ziff, Gulari, and Barshad model, simulates the carbon monoxide oxidation on a Pt substrate. In both models, understanding the geometrical features of the oxidation process and the impact of impurities are major challenges which we address here.

This chapter is organized as follows: in the following section, both models for the ethanol electro-oxidation and carbon monoxide oxidation are introduced. In Section 2.2, Monte Carlo and analytical results are presented for the one-dimensional case of ethanol electro-oxidation. The 2D one is presented on Section 2.3, with both clean and impurities covered substrate. The results for the carbon monoxide oxidation, with relevance to the phase transitions found in it, are on Section 2.4. The final conclusions are drawn on Section 2.5.

2.1 Catalysis models

As previously stated, these two models are intrinsically different. One does not allow desorption leading always the system into a jamming state, where no more particles can be adsorbed. The other allows desorption of the reaction products, in that case carbon dioxide, and the system can be found in three different states: a continuous reactive state, where reactants continuously adsorb in the substrate, and two adsorbing states, one covered with carbon monoxide and the other covered with oxygen, where no more particles can adsorb.

2.1.1 Ethanol electro-oxidation model

Aiming a comprehensive understanding of adsorption processes and reactions on surfaces, several models have been developed with special emphasis for the ones based on random sequential adsorption [41]. Those models have mainly been studied through numerical simulations (e.g. Monte Carlo methods) [105, 106, 107, 108, 109, 110, 111, 112, 84], but there are also some analytical solutions [113, 114, 115, 116]. Our work focus on the electro-oxidation of ethanol. The interest on the oxidation of ethanol comes from its relevance on energy production. Ethanol fuel cells, being less toxic than others based on different alcohols, provide a clean, abundant, and reliable source of energy [117].

The random sequential adsorption model (RSA) has been considered as a reliable one to describe geometrical properties of the adsorption phenomenon, in the limit where the rate of desorption can be neglected. Adsorption attempts occur sequentially at sites, randomly selected, and the particle-particle interaction is coarse grained as an excluded volume one. For a more detailed description, the cooperative sequential adsorption (CSA) model has also been introduced [41], where the rates of adsorption depend on the local configuration [118]. Accounting for these effects, opens up the possibility of some control over the process to achieve a selection of species, like e.g., a specific enantiomers [119]. Besides, the RSA model and its generalization CSA, have also been considered to

understand a variety of problems, such as chemical reactions on catalytic surfaces [120], polymer reactions [121], particles adsorption on membranes [122], hydrocarbons hydrogenation reactions [123], protein [124], and colloids [125] adsorption.

During ethanol electro-oxidation, a binary adsorption takes place [23, 24], where the presence of pre-adsorbed species, in the neighborhood of the landing site, leads to the adsorption of the ethanol molecule as a monomer, suppressing the C-C cleavage. To account for this mechanism, we propose a generalized version of the CSA model where, based on the local configuration, the specie can either adsorb as a dimer or a monomer. Despite the focus on this particular system, our model can be considered to analyze other processes with an equivalent cleavage mechanism, e.g., sugars [126].

Under real conditions, the pre-adsorbed species which suppress the cleavage may be related with impurities or defects in the substrate. The effect of such heterogeneities on the adsorption process has been addressed in several occasions, in the context of RSA-like models [127, 128, 129, 130, 131, 132, 133, 134, 135]. In this work, we also shed light on this effect and show that, a controlled presence of pre-adsorbed species can be considered to promote selectivity of species.

Ethanol oxidation is of great relevance to the society, since its oxidation releases twice the energy of the one of methanol [136], posing it as a candidate to replace several classical sources of energy [40]. Wang and Liu [23] have proposed a mechanism for the Ethanol electro-oxidation on Pt substrates, which can be summarized in three pathways [24]:

- The *OH Path*, where the cleavage of the hydroxyl group leads to the formation of acetaldehyde which is then adsorbed;
- The *CH Path* where there is first a production of CH_3CHOH, being then further degraded to CH_3COH;
- The *Concerted Path* where the Ethanol molecule starts by loosing two hydrogens, followed by the desorption of acetaldehyde.

It was shown that in the Pt(100) surface (which can be mapped to a square lattice)

the relevant pathway is mainly the *CH Path* [23], where ethanol adsorption leads to the formation of acetyl (CH_3CO). The work of Wang and Liu [23] discloses that the adsorption mechanism is strongly influenced by the actual surface coverage. At low surface coverages, the Acetyl dehydrogenates into CH_2CO or $CHCO$, which leads to a $C-C$ bond cleavage, yielding CH and CO fragments. At oxidative conditions, both fragments react with the O present on the surface and desorb as CO_2. The desorption of the cleaved products can be neglected for non-oxidative conditions, which leads the system to a jamming state. Whereas, when the surface coverage is high, the $C-C$ bond cleavage is blocked, and the surface is poisoned with acetyl.

Based on the proposed mechanism, we introduce a model which can be summarized by the following rules,

$$\begin{aligned} A + 2v &\xrightarrow{k_d} 2B \\ A + 1v &\xrightarrow{k_m} C, \end{aligned} \tag{2.1}$$

where A is the ethanol molecule, $2B$ are the $C-C$ cleaved products, C is an acetyl, and k_d (k_m) stands for the dimer (monomer) deposition rate.

As cartooned on Figure 2.1, dimers are deposited uniformly on the substrate (lattice). Successful adsorption of dimers requires two neighboring empty sites. If only one is available, the specie adsorbs as a monomer. When both sites are occupied, due to the excluded volume interaction, the adsorption attempt fails and the particle attempting adsorption is no longer considered. This model differs from the traditional CSA [41] since, for the latter, the rates of adsorption on CSA depend on the state of the nearest neighbors and not on the occupation of the actual adsorption sites, while here an adsorption of dimers is considered which can take place as a monomer when one of the adsorbing sites is occupied.

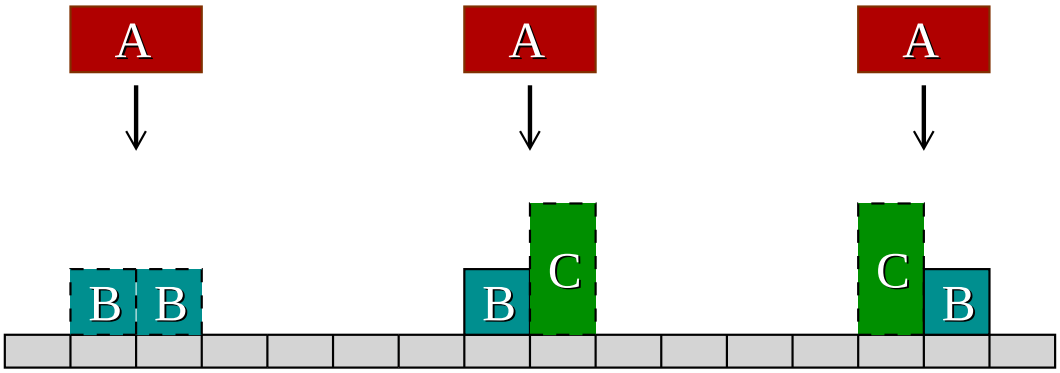

Figure 2.1: Schematic representation of the adsorption rules. The A-specie (red) deposition with two empty spaces gives B-products (blue) or with only one empty space gives C (green).

2.1.2 Carbon monoxide oxidation model

A suitable nonequilibrium system, with two irreversible phase transitions, is provided by the well-known Ziff, Gulari, and Barshad model [42] to explain the heterogeneous catalytic oxidation of carbon monoxide on a Pt(100) substrate. In this model, reactants adsorb in the substrate and react upon contact with each other. The products desorb after reaction. The reaction scheme of the model is the Langmuir-Hinshelwood mechanism,

$$\begin{aligned} A(g) + v &\rightarrow A(a) \\ B_2(g) + v &\rightarrow 2B(a) \\ A(a) + B(a) &\rightarrow AB(g) + 2v \end{aligned} \tag{2.2}$$

where A (monomer) and B (dimer) are the reactants, AB the product, v empty sites, and g and a, gas and adsorbed phase respectively.

Dimers (Oxygen molecules) adsorb (and dissociate) at the surface when two nearest-neighbor lattice sites are empty, while monomers (carbon monoxide) require only a single empty site for adsorption, and no surface mobility is allowed to either reactant species. Monomers adsorption is attempted with a probability y_{A} and dimers with $y_{\mathrm{B}} = 1 - y_{\mathrm{A}}$.

The reaction is instantaneous upon contact of an oxygen atom and a carbon monoxide molecule on two neighbor sites. This model has the interesting characteristic of presenting two irreversible phase transitions, one is a continuous phase transition at lower values of y_A with the poisoning by dimers, and the other is a first-order phase transition at higher values of y_A with the poisoning of monomers.

Several generalizations have been devised to accommodate more realistic features, however this work will focus on the presence of impurities. Impurities can be both quenched defects on the surface [137, 138, 139, 140, 141, 142] or present in the gas phase [143, 144, 145], and this work will approach the first case. The presence of impurities on the Ziff, Gulari, and Barshad model has been shown to change the order of the phase transition at the monomer poisoning phase transition from first order at low impurity coverage to a second order above a critical impurity coverage [138, 139, 140].

2.2 1D ethanol electro-oxidation

2.2.1 Analytical study

The analytical solution for the evolution of the coverage and of the distribution of empty sites can be obtained by writing the rate equation for the mechanisms of Figure 2.1. The exact results are divided into three limiting cases: the same deposition rates for dimers and monomers, preferential dimer site adsorption, and different deposition rates for monomers and dimers.

Let us start by defining P_n as the probability of a randomly chosen site belong to a segment of empty sites with length $\ell \geq n$. A catalog of the possible ways such a segment can be split, is in Figure 2.2. The segment can be destroyed by a monomer deposition on the left side of the segment in b), the right side of c), or on both sides of e). It can also be destroyed by a dimer deposition on any site of the segment in a), the right side of b), the left side of c), or on both sides of d).

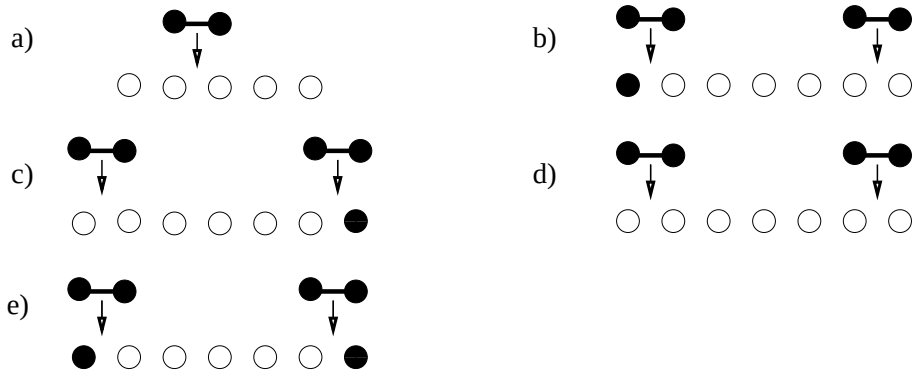

Figure 2.2: Catalog of possible ways of splitting a segment of empty sites with length $\ell \geq n$.

Each configuration is obtained with a probability given by,

$$\begin{aligned} P[\circ\circ\circ\circ\circ] &= P_n \\ P[\bullet\circ\circ\circ\circ\circ\circ] &= P[\circ\circ\circ\circ\circ\circ\bullet] = P_{n+1} - P_{n+2} \\ P[\circ\circ\circ\circ\circ\circ\circ] &= P_{n+2} \\ P[\bullet\circ\circ\circ\circ\circ\bullet] &= 2P_n - 2P[\bullet\circ\circ\circ\circ\circ\circ\circ] - P[\circ\circ\circ\circ\circ\circ\circ] \\ &= P_n - 2P_{n+1} + P_{n+2}. \end{aligned} \tag{2.3}$$

The proper set of rate equation depends on the considered case. Below, we describe this set for equal deposition rate of dimers and monomers, adsorption of a preferential dimer site, and different deposition rates for dimers and monomers.

Equal deposition rates of dimers and monomers

For equal deposition rates of monomers and dimers, the rate of both species is considered as k. The rate of change of P_n due to the adsorption of dimers is given by,

$$\begin{aligned}\left(\dot{P}_n\right)_d &= -k(n-1)P_n - kP[\bullet\circ\circ\circ\circ\circ\circ] \\ &\quad -kP[\circ\circ\circ\circ\circ\circ\bullet] - 2kP[\circ\circ\circ\circ\circ\circ\circ] \\ &= -(n-1)kP_n - 2kP_{n+1},\end{aligned} \tag{2.4}$$

where $(n-1)$ corresponds to the destruction rate of a segment with, at least, n empty sites, which is zero for $n = 1$, see Figure 2.2(a). The rate of change due to monomers adsorption is,

$$\begin{aligned}\left(\dot{P}_n\right)_m &= -2kP[\bullet\circ\circ\circ\circ\circ\bullet] - kP[\bullet\circ\circ\circ\circ\circ\circ] \\ &\quad -kP[\circ\circ\circ\circ\circ\circ\bullet] \\ &= -2k(P_n - P_{n+1}).\end{aligned} \tag{2.5}$$

From Eqs. (2.4) and (2.5), the total rate of change is given by,

$$\left(\dot{P}_n\right)_T = \left(\dot{P}_n\right)_d + \left(\dot{P}_n\right)_m = -(n+1)kP_n. \tag{2.6}$$

This result is equivalent to consider that, regardless the type of adsorption, a segment of n, or more, empty sites can be destroyed by adsorption on $(n+1)$ different places. This equation gives $P_n(t) = \exp\left[-(n+1)kt\right]$. The coverage θ can then be obtained from the probability of a certain site belong to a segment of size $n \geq 1$, i.e.,

$$\theta(t) = 1 - P_1(t) = 1 - \exp\left(-2kt\right). \tag{2.7}$$

Defining $s_m(n)$ as the rate of monomers adsorption on a n-segment, i.e., $s_m(n) = -\left(\dot{P}_n\right)_m$, we obtain,

$$\begin{aligned} s_m(n) &= 2k(P_n - P_{n+1}) \\ &= 2k\left[\exp\left(-\left[n+1\right]kt\right) - \exp\left(-\left[n+2\right]kt\right)\right]. \end{aligned} \tag{2.8}$$

The adsorption of monomers on a segment of size $n \geq 1$ is given by,

$$s_m(n=1) = 2k\left[\exp\left(-2kt\right) - \exp\left(-3kt\right)\right]. \tag{2.9}$$

From the rate of adsorption, the coverage of monomers can be obtained from $\dot{\theta}_m = s_m$ for $n = 1$ giving,

$$\theta_m(t) = \left[1 - \exp\left(-2kt\right)\right] + \frac{2}{3}\left[\exp\left(-3kt\right) - 1\right]. \tag{2.10}$$

Defining now $s_d(n)$ as the rate of dimers adsorption on a n-segment, i.e., $s_d(n) = -\left(\dot{P}_n\right)_d$, we obtain,

$$s_d(n) = k\left[\left(n-1\right)\exp\left(-\left[n+1\right]kt\right) + 2\exp\left(-\left[n+2\right]kt\right)\right]. \tag{2.11}$$

The adsorption of dimers on a segment of size $n \geq 1$, is then given by,

$$s_d(n=1) = 2k\exp\left(-3kt\right). \tag{2.12}$$

Knowing the rate of adsorption, the coverage of dimers can be obtained from the rate equation, $\dot{\theta}_d = s_d(n=1)$,

$$\theta_d(t) = \frac{2}{3}\left[1 - \exp\left(-3kt\right)\right]. \tag{2.13}$$

Adsorption of a preferential dimer site

Considering a preferential dimer site means that the symmetry is broken and the first adsorption on the substrate is done by a specific compound of the dimer. The cleavage

only takes place if there is a neighboring empty site, in any direction, to adsorb the other compound. In $1D$, the left site of the dimer is considered as the preferred one. However, by symmetry, results are independent of the considered one. For this special case, the change on the P_n by dimers is,

$$\begin{aligned}\left(\dot{P}_n\right)_d &= -k(n-1)P_n - kP[\bullet\circ\circ\circ\circ\circ\circ] \\ &\quad -kP[\circ\circ\circ\circ\circ\circ\bullet] - 2kP[\circ\circ\circ\circ\circ\circ\circ] \\ &= -(n-1)kP_n - 2kP_{n+1},\end{aligned} \tag{2.14}$$

while by monomers is,

$$\begin{aligned}\left(\dot{P}_n\right)_m &= -kP[\bullet\circ\circ\circ\circ\circ\bullet] - kP[\circ\circ\circ\circ\circ\circ\bullet] \\ &= -k(P_n - P_{n+1}).\end{aligned} \tag{2.15}$$

For the total change on P_n we obtain,

$$\left(\dot{P}_n\right)_T = \left(\dot{P}_n\right)_d + \left(\dot{P}_n\right)_m = -nkP_n - kP_{n+1}. \tag{2.16}$$

Considering the relation between P_n and P_{n+1} as, $P_{n+1} = Q_nP_n$ [146], then $\dot{P}_{n+1} = \frac{d(Q_nP_n)}{dt}$, giving,

$$\dot{P}_{n+1} = -(n+1)kQ_nP_n - kQ_{n+1}Q_nP_n, \tag{2.17}$$

plugging it back into Eq. (2.16) [41, 147] we obtain,

$$\frac{dQ_n}{dt}\frac{1}{Q_n} = -(n+1)k + nk - k(Q_{n+1} - Q_n). \tag{2.18}$$

If we assume $Q_{n+1} = Q_n$, then $\frac{dQ_n}{Q_n} = -kdt$. Therefore, $Q_n(t) = \exp(-kt)$, which when replaced in Eq. (2.18) gives $\dot{P}_n = -[nk + k\exp(-kt)]\,P_n$, and so,

$$P_n(t) = \exp[-nkt + (\exp[-kt] - 1)]. \tag{2.19}$$

Since the coverage θ is dependent on the evolution of the probability of finding a segment of size $n \geq 1$,

$$\theta(t) = 1 - P_1(t) = 1 - \exp[-kt + (\exp[-kt] - 1)]. \tag{2.20}$$

The independent rates of adsorption for dimers and monomers, and the subsequent calculation of the coverage for each specie are solved as before.

Different deposition rates for dimers and monomers

To attempt a generic solution for the rules given by Eq. (2.1), it is necessary to consider different deposition rates for monomers (k_m) and dimers (k_d). Accounting for the rate of change of P_n by dimers given by Eq. (2.4),

$$\left(\dot{P}_n\right)_d = -(n-1)k_d P_n - 2k_d P_{n+1}, \tag{2.21}$$

while by monomers,

$$\left(\dot{P}_n\right)_m = -2k_m(P_n - P_{n+1}). \tag{2.22}$$

The change on the the total P_n with time is then given by,

$$\begin{aligned} \left(\dot{P}_n\right)_T &= \left(\dot{P}_n\right)_d + \left(\dot{P}_n\right)_m \\ &= -[k_d(n-1) + 2k_m]\,P_n - 2(k_d - k_m)P_{n+1}. \end{aligned} \tag{2.23}$$

For the sake of simplicity, we define $\alpha_n = (n-1)k_d + 2k_m$ and $\beta = k_d - k_m$. In the same way as before, applying the relation $P_{n+1} = Q_n P_n$, the rate equation for P_{n+1} is,

$$\dot{P}_{n+1} = \dot{Q}_n P_n + Q_n \dot{P}_n = -\alpha_{n+1} Q_n P_n - 2\beta Q_{n+1} Q_n P_n, \tag{2.24}$$

replacing $\dot{P}_n$ by Eq. (2.22),

$$\begin{aligned} &\dot{Q}_n P_n + Q_n \left[-(\alpha_n + 2\beta Q_n) P_n\right] = \\ &-\left(\alpha_{n+1} Q_n + 2\beta Q_{n+1} Q_n\right) P_n \\ &\dot{Q}_n = -k_d Q_n - 2\beta (Q_{n+1} - Q_n) Q_n, \end{aligned} \tag{2.25}$$

and considering the relation $Q_{n+1} = Q_n$, then $Q_n(t) = \exp(-k_d t)$. From the above result, Eq. (2.23) simplifies as $\dot{P}_n = -\left(\alpha_n - 2\beta Q_n\right) P_n$, which gives,

$$P_n(t) = \exp\left[-([n-1]\, k_d + 2k_m)t - \frac{2(k_d - k_m)}{k_d}\left(1 - \exp\left[-k_d t\right]\right)\right]. \tag{2.26}$$

From Eq. (2.7),

$$\begin{aligned} \theta(t) &= 1 - P_1(t) \\ &= 1 - \exp\left[-2k_m t - \frac{2(k_d - k_m)}{k_d}\left(1 - \exp\left[-k_d t\right]\right)\right], \end{aligned} \tag{2.27}$$

and for $k_m = k_d = k$ the solution boils down to Eq. (2.7). If $s_m(n)$ is defined as the rate of monomers adsorption on a n-segment $s_m(n) = -\left(\dot{P}_n\right)_m$, then,

$$s_m(n) = 2k_m(1 - Q_n)P_n. \tag{2.28}$$

The relations $y = \exp(-k_d t)$ and $\gamma = \frac{k_m}{k_d}$ are considered, and the adsorption of monomers on a segment of size $n \geq 1$ is given by,

$$s_m(n=1) = 2k_m\left[1 - y\right] y^{2\gamma} \exp\left[-2(1-\gamma)(1-y)\right]. \tag{2.29}$$

From the rate of adsorption, the coverage of monomers is given by, $\dot{\theta}_m = s_m$ for $n = 1$, leading to,

$$\dot{\theta}_m = 2k_m\,(1-y)\,y^{2\gamma}\exp\left[-2(1-\gamma)(1-y)\right], \tag{2.30}$$

and so,

$$\theta_m = -\int_1^{\exp(-k_d t)} 2\gamma\,(1-y)\,y^{2\gamma-1}\exp\left[-2(\gamma-1)(1-y)\right]dy. \tag{2.31}$$

The dimers rate of adsorption is then,

$$s_d(n) = k_d(n-1)P_n + 2k_d Q_n P_n. \tag{2.32}$$

For the sake of simplicity, the relation $y = \exp(-t)$ is used, and the adsorption of dimers on a segment of size $n \geq 1$ is given by,

$$s_d(n=1) = 2k_d\left[y^{k_d}y^{2k_m}\exp\left(-\frac{2\left[k_d-k_m\right]}{k_d}\left[1-y^{k_d}\right]\right)\right]. \tag{2.33}$$

For the rate of adsorption, the coverage of monomers can be given by, $\dot{\theta}_d = s_d$ for $n = 1$, and integrating over y gives,

$$\theta_d = -\int_1^{\exp(-t)} 2k_d y^{k_d+2k_m-1}\exp\left[-\frac{2(k_d-k_m)}{k_d}(1-y^{k_d})\right]dy. \tag{2.34}$$

2.2.2 1D Monte Carlo simulations

We numerically studied the proposed model through Monte Carlo simulations, performed on a lattice with 10^4 sites, where periodic boundary conditions have been applied and results have been averaged over 10^2 samples.

The coverage as a function of time is plotted on Figures 2.3(a), (b), and (c) for the three previously described cases, namely, equal deposition rate of dimers and monomers, adsorption of a preferential dimer site, and different deposition rates for dimers and monomers.

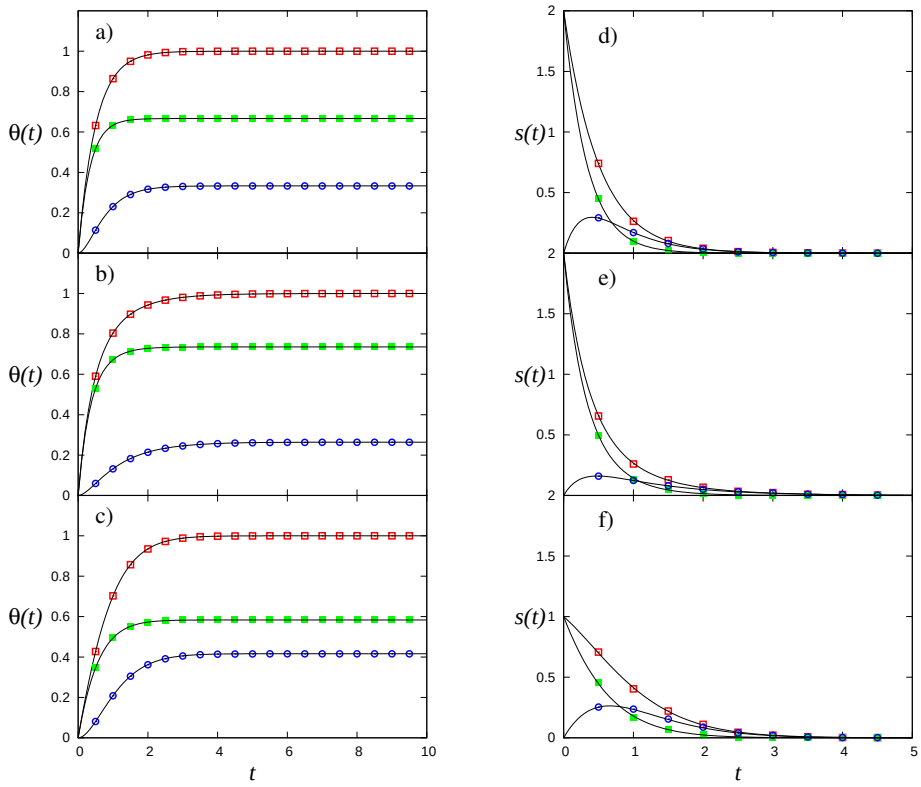

Figure 2.3: Coverage ($\theta(t)$) and rates ($s(t)$) of adsorption as a function of time obtained through Monte Carlo simulations (symbols) and analytically (solid line) for equal rates of adsorption (a) and (d), preferential carbon adsorption (b) and (e), and different rates of adsorption ($k_d = 0.5$ and $k_m = 1$) (c) and (f). Total coverage and rates of adsorption (open squares), dimers (full squares), and monomers (open circles).

The total coverage θ_T, the coverage of dimers θ_d, and the coverage of monomers θ_m are computed over 10 Monte Carlo (MC) sweeps, where one MC sweep corresponds to one adsorption attempt per lattice site. Figure 2.3(a) shows the case of equal deposition rates for dimers and monomers, where $k_d = k_m = 1$. The solid lines in the plot represent the analytical solution given by Eqs. (2.7), (2.10), and (2.13). The preferential dimer site rule of adsorption is in Figure 2.3(b), where despite the values of the deposition rates being given by $k_d = k_m = 1$, the results are equivalent to having values of $k_d = 1$ and $k_m = 0.5$, since the deposition of a monomer by the non-favored dimer site is not allowed. For these rules of deposition, the exact results are given by Eqs. (2.20), (2.14), and (2.15). The final

case, where a different deposition rate for dimers and monomers is considered, is plotted in Figure 2.3(c), with deposition rates of $k_d = 0.5$ and $k_m = 1$. The exact solution is given by Eqs. (2.27), (2.31), and (2.34). For all cases, data points from Monte Carlo lay on the line given by the exact solution.

Figures 2.3 (d), (e), and (f) show the rates of adsorption as a function of time (only five MC sweeps are shown). The plots (d), (e), and (f) correspond, respectively, to equal deposition rates, preferential dimer site rule, and different deposition rates. For the same conditions as for the coverage study, some particular aspects can be observed. The dimers rate of adsorption, for instance, starts at a value of two for $k_d = 1$ since dimers occupy two sites at each deposition. The monomers rate of adsorption starts at zero, and increases since it requires previously adsorption of, at least, one particle. The rate of monomers adsorption increases due to the large influence of the substrate coverage and reaches a maximum when the number of isolated empty sites start to decrease. Exact results are shown for each plot, and are consistent with the ones obtained with Monte Carlo simulations.

Since desorption is neglected, a jamming limit is obtained where no further particles can be adsorbed. In Figure 2.4, we see the coverage in the jamming limit θ_∞ as a function of the ratio between dimers and monomers deposition rates, $R = k_d/k_m$, where the solid line is the analytical solution, open circles are dimers, and full squares monomers. It can be observed that in the limit of $R \ll 1$, a complete coverage of monomers is found, except for one dimer that always need to be adsorbed to start the monomers deposition. With the decrease in the coverage of monomers an increase on the coverage of dimers is observed and an equal coverage is reached for a ratio $R = 0.207 \pm 0.006$. In the limit of $R \gg 1$, a maximum coverage of dimers is obtained in agreement with the classical adsorption of dimers in a one-dimensional lattice [41]. For the jamming, Monte Carlo results are also in agreement with the analytical solution.

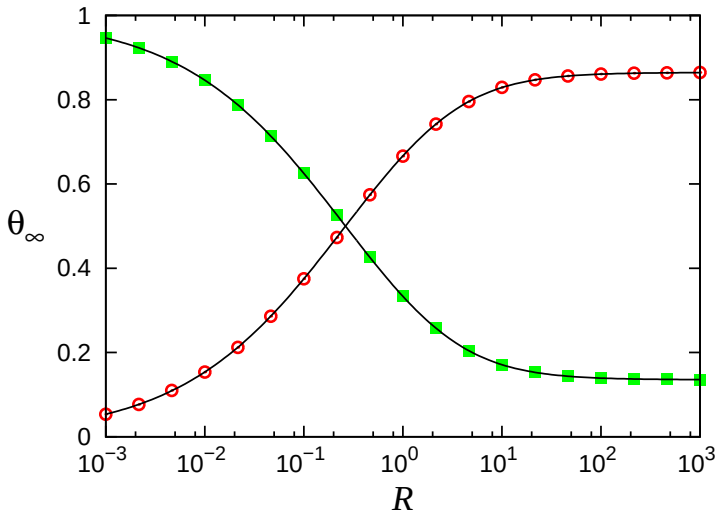

Figure 2.4: Coverage of dimers (open circles) and monomers (full squares) for Monte Carlo simulations and obtained analytically (solid line), with the analytical solution (solid line), at the jamming limit as a function of the ratio between the rate of deposition of dimers and monomers R.

2.3 2D ethanol electro-oxidation

In two dimensions, even for the simplest case of monomers adsorption, no analytical solution has been found. However, it is a case of interest, specially the regular square lattice which reproduces, for example, the topology of the Pt(100) surface. In this section, we study the proposed model on a square lattice through Monte Carlo simulations. We devote special attention to the percolation properties of aggregates of monomers and dimers [148].

Monte Carlo simulations have been performed on square lattice of different sizes, namely, 128^2, 256^2, and 512^2 lattice sites, with periodic boundary conditions in both directions. Results have been averaged over 10^4 samples for values of R between 10^{-3} and 10^3. To decrease the computational effort, a rejection free algorithm was implemented, where the next adsorption trial takes place on an empty site randomly selected from a list of available sites, where the weight of each configuration is properly taken into account. To accurately follow the time evolution, the entire population of events is considered as

well as the rate of monomers and dimers adsorption.

Simulations have been done on both clean and impurities-covered substrates. Impurities are considered quenched and, for the sake of simplicity, solely influence the adsorption process by purely geometrical restrictions.

2.3.1 Clean substrate

On a clean substrate, the coverage of dimers is larger than for monomers and the rate of adsorption of monomers as a function of time has a maximum, as also observed on the one-dimensional case. However, the coverage of monomers is favored in two dimensions, since each deposited dimer as a greater influence on monomers deposition than in one dimension, mainly due to a larger fraction of configurations with pairs of occupied and empty neighboring sites. This can be observed on Figure 2.5, where we plot the jamming limit θ_∞ as a function of the ratio R. In this case, the point of equal coverage for dimers and monomers occur for a ratio $R \approx 0.6$, which is larger than in one dimension, corroborating that monomers are favored.

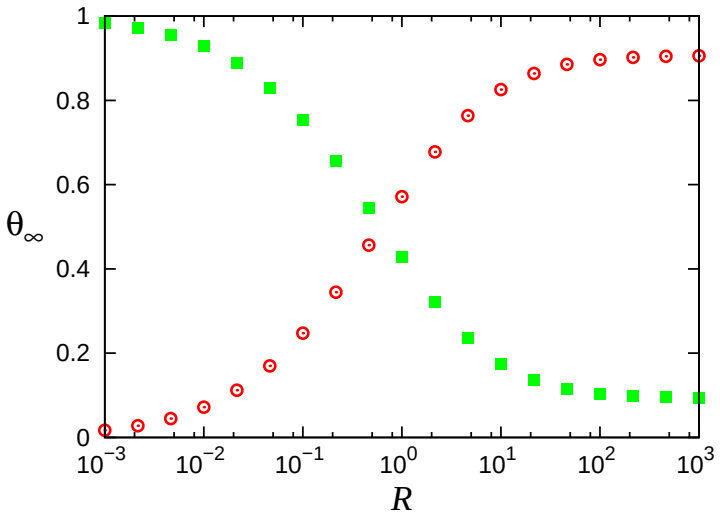

Figure 2.5: Jamming coverage (θ_∞) as a function of the ratio between the rate of adsorption of dimers and monomers R, in $2D$, of dimers (open circles) and monomers (full squares) for a system size of 512^2 lattice sites.

The percolation behavior is analyzed by identifying clusters in the system with the Hoshen-Kopelman algorithm [149]. While for lower values of R the system is dominated by monomers, as discussed for 1D, for higher values of R dimers dominate. A percolation transition is then observed for both dimers and monomers with R as a control parameter. In Figure 2.6(a) we plot the spanning probability R_L defined as the probability of having a percolation cluster in the system. We analyze both percolations. At the percolation transition of either monomers or dimers, the fraction of sites occupied by the specie under study is compatible with the percolation threshold for site percolation in the considered topology [150]. In the top inset of Figure 2.6(a) is the fraction of sites belonging to the largest cluster P_∞ (the order parameter of the percolation transition). The average cluster size, normalized by the system size, $\langle P\rangle = \langle s\rangle/N$ is plotted on the bottom inset of Figure 2.6(a). On this plot, the average size of clusters reduces with the system size. This occurs due to a larger weight of smaller clusters in the sampling.

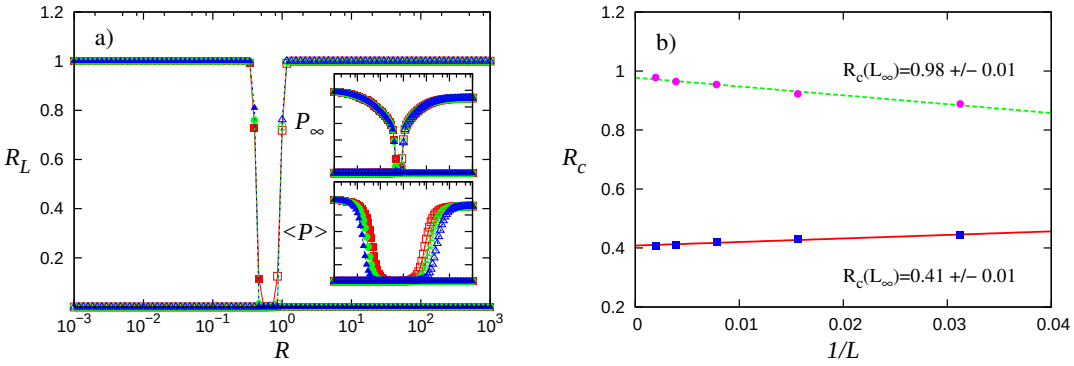

Figure 2.6: a) Dependency on the ratio R of the spanning probability R_L for dimers (open) and monomers (full). Square lattices have been considered with 128^2 (squares), 256^2 (circles), and 512^2 (triangles) lattice sites, for the spanning probability R_L, clusters medium size $\langle P\rangle$(bottom inset), and fraction of sites belonging to the largest cluster P_∞ (top inset). b) Percolation threshold (R_c) as a function of the system sizes, for linear sizes of $L = \{32, 64, 128, 256, 512\}$, for dimers (full circles) and monomers (full squares).

The percolation threshold (R_c) can be estimated by analyzing the maximum value on the standard deviation of the spanning probability. It can be observed in Figure 2.6(b), that the percolation threshold scales with the system size. Obtaining for dimers $R_c(L_\infty) =$

0.98 ± 0.01, and for monomers $R_c(L_\infty) = 0.41 \pm 0.01$.

The scaling of the average size of the largest cluster ($\langle s_{max} \rangle$) at R_c gives some relevant information on the percolation transition. Figure 2.7(a) shows $\langle s_{max} \rangle$ as a function of the system size (L) which scales as $\sim L^{D_f}$, where D_f is the fractal dimension. For both monomers and dimers the obtained scaling of the system size dependence of the mass of the largest cluster is consistent with the fractal dimension $D_f = 1.8958$ of the classical percolation universality class [150].

Another important parameter to be taken into account is the second momentum of the cluster size distribution given by,

$$M_2 = \frac{\sum_{i \neq max} s_i^2}{N}, \tag{2.35}$$

where s is the cluster size, N is the total number of lattice sites, and the sum runs over all clusters excluding the largest one. The size of the largest cluster is removed from the simulation. The variable M_2 at R_c as a function of the system size is given in the inset of Figure 2.7(a), where another scaling behavior is observed obeying to the power law $M_2 \sim L^{\frac{\gamma}{\nu}}$, with $\frac{\gamma}{\nu} = 1.8$, in agreement with the scaling relation $\frac{\gamma}{\nu} = 2D_f - d$.

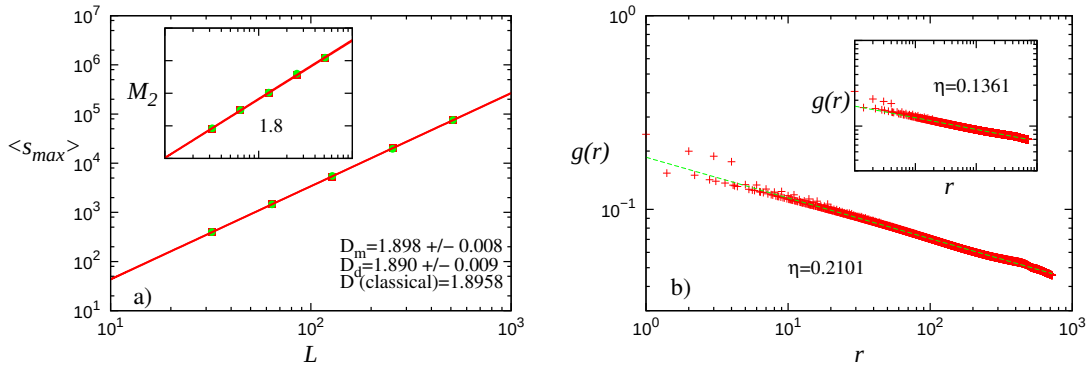

Figure 2.7: a) Largest cluster (s_{max}) and (inset) second moment of the cluster size distribution function (M_2) at R_c as a function of the system sizes, for linear sizes of $L = \{32, 64, 128, 256, 512\}$, for dimers (full circles) and monomers (full squares). b) correlation function ($g(r)$) for dimers (monomers on the inset) for a system of linear size $L = 1024$ and 100 samples.

We also measured the correlation function, also known as connectivity correlation function, defined as

$$g(r) = \langle \delta_{ij} \rangle - \frac{s_{max}^2}{N^2}, \tag{2.36}$$

where δ_{ij} is 1 if both sites i and j are occupied by the same cluster and zero otherwise. s_{max} is the size of the largest cluster. Figure 2.7(b) shows that at R_c both correlation functions are power laws with the same exponent of classical percolation.

2.3.2 Substrate with impurities

Impurities are common on realistic systems, for example, Pb atoms on catalytic surfaces [10]. To be considered, quenched impurities are randomly distributed on the substrate. These impurities do not react and remain immobile, influencing only the adsorption, mainly the mechanism of dimer dissociation, which can favor monomers at the jamming state.

Since impurities geometrically favor the coverage of monomers, the value of $\theta_m - \theta_d$ as a function of impurities coverage θ_{imp} is plotted in Figure 2.8. A maximum is observed at a specific value of impurities coverage. Different maximum positions are identified for different ratios R, where low values of R favor monomers leading to an earlier maximum, and a high ratio unfavors monomers leading to a later maximum. These results open up the possibility of tuning the production of monomers by controlling the fraction of impurities in the system.

In addition to an influence on species coverage, impurities also shift the percolation threshold. Figures 2.9(a) and (b), show the spanning probability R_L as a function of the ratio between the deposition rate of monomers and dimers for various values of impurities coverage. The monomers percolation transition is mainly affected at larger impurities coverages and is shifted to lower values of R. Dimers percolation transition, on the other hand, is shifted to higher values of R. For higher values of the impurities coverage, the clusters of impurities predominate in the surface and neither monomers nor dimers

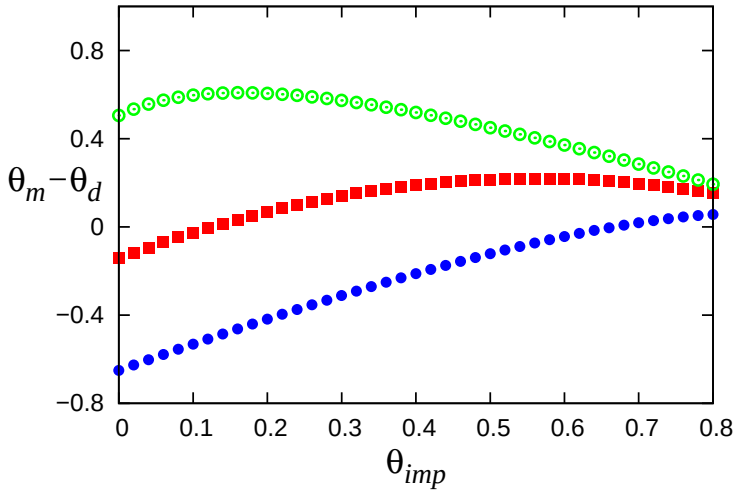

Figure 2.8: Difference in the jamming coverage of monomers and dimers as a function of the impurities coverage, in $2D$, for $R = 0.1$ (open circles), $R = 1$ (full squares), and $R = 10$ (full circles) for a system size of 512^2 lattice sites.

percolate. The top inset of Figures 2.9(a) and (b) shows the fraction of sites belonging to the largest cluster P_∞ as a function of R, with $P_\infty = \frac{\langle s_{max} \rangle}{N(1-\theta_{imp})}$, where N is the total number of lattice sites, and θ_{imp} is the coverage of impurities. The normalized average cluster size $\langle P \rangle$ is also plotted in the bottom inset of Figures 2.9(a) and (b), with $\langle P \rangle = \frac{\langle s \rangle}{N(1-\theta_{imp})}$. In the case of monomers, as disclosed by the behavior of the spanning probability, the size of the largest cluster is only significantly affected by impurities for values of impurities coverage above 30%. In the case of dimers, impurities have a larger effect on R_L and P_∞. In both cases, the average cluster size is largely reduced with the increase of impurities, since the number of small clusters isolated by impurities increase.

In Figures 2.10(a) and (b), we see the influence of impurities coverage on the percolation cluster for both monomers, at $R = 0.1$, and dimers, at $R = 10$. It can be shown that for monomers the percolation cluster disappear for $\theta_{imp} \approx 0.35$, and for dimers it disappears at $\theta_{imp} \approx 0.25$. Regardless of the ratio R, all reactants percolation transitions disappear in the limit of $\theta_{imp} = 1 - p_c$, where p_c is the site percolation threshold on a square lattice.

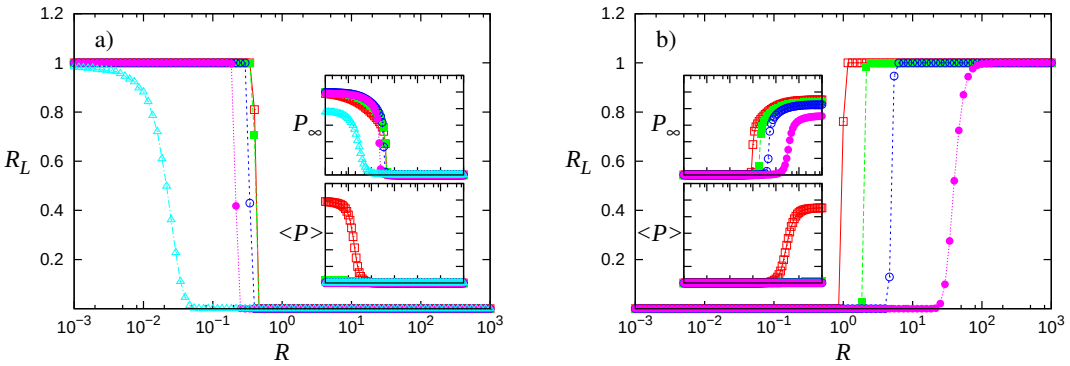

Figure 2.9: Spanning probability as a function of the ratio R, in $2D$, for a) monomers with impurities coverage from right to left of 0%, 10%, 20%, 30% and, 40%, and b) dimers with impurities coverage from left to right of 0%, 10%, 20%, and 30%. Simulation of a system size of 512^2. Clusters medium size $\langle P \rangle$ on the bottom inset and maximum cluster size P_∞ on the top inset.

2.4 2D carbon monoxide oxidation

Nonequilibrium phase transitions, i.e., phase transitions occurring in nonequilibrium systems have been, in recent years, target of extensive research [151, 152, 85, 153]. Mainly nonequilibrium phase transitions into absorbing states [152, 153], due to the variety of systems that exhibit them. One relevant objective is to identify the nature of an absorbing phase transition, typically, first or second order. In the case of reversible phase transitions, a standard procedure to distinguish a first-order from a second-order can be resorting to hysteresis loops. However, such a procedure drives the system, which may, in the case of irreversible phase transitions, lead to an absorbing state, which in some cases does not lead to a correct assumption over the nature of the transition [154]. For the case studied here, the definition of the nature of the irreversible phase transition will rely on the short and long correlation length present on first and second order phase transitions.

To study the phase transitions on the original Ziff, Gulari, and Barshad model several procedures have been used in the literature including mean-field studies [155], epidemics analysis [156, 157], and hysteresis loops using constant-coverage ensemble [158]. Some of these procedures, and others, have been employed to analyze the influence of impurities

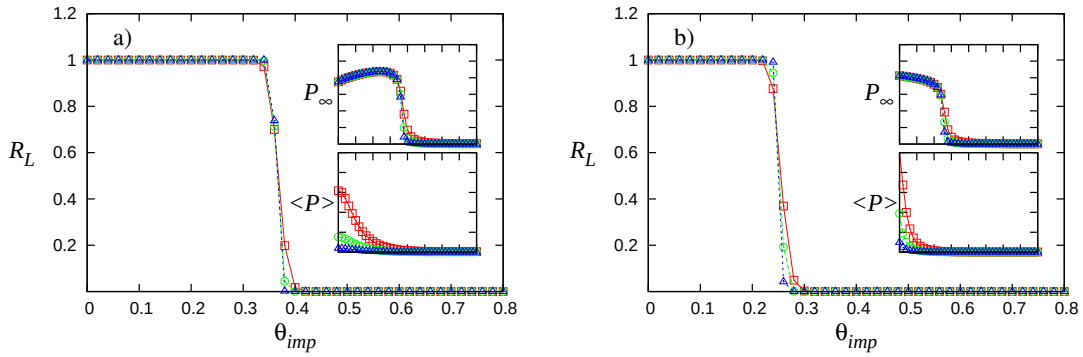

Figure 2.10: Cluster analysis as a function of the impurities coverage. Simulation of sizes 128×128 (squares), 256×256 (circles), and 512×512 (triangles), for the spanning probability R_L, clusters medium size $\langle P \rangle$ (bottom inset), and maximum cluster size P_∞ (top inset) at a) monomers at $R = 0.1$ and d) dimers at $R = 10$.

on the first-order phase transition. The use of hysteresis analysis has been performed with the introduction of CO desorption [141], which can be done since the desorption gives a reversible character to the phase transition. Also mean field [139] and other simulation studies [138, 140] were applied to the characterization of the phase transition, together with the calculation of critical exponents on an epidemics study [144].

In the present work, we apply concepts of long and short range correlation length to study the value of the critical *impurity* coverage at which the nature of the transition changes, exploiting the fact that correlation length is finite at a first-order phase transition and infinite at a second-order one [159]. We exploit the fact that the size of clusters scale with the size of the system above a critical value of impurities coverage (Figure 2.11). It was also found that the system undergoes a percolation transition before the poisoning one above that same critical value.

It has been shown in the literature that the addition of small amounts of *impurities* affects both transition points (with a stronger impact on the upper-bound one by significantly lowering its value). The presence of *impurities* not only changes the position of the critical value of the upper-bound transition, but it also changes its nature from a first- to a second-order phase transition. Like previously mentioned, the effect

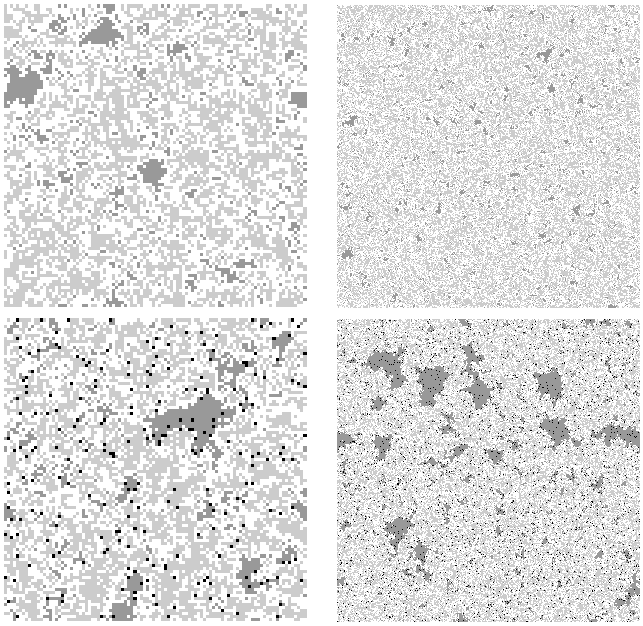

Figure 2.11: Snapshots of a clean substrate system (top) and for a system with 2.5% of coverage by impurities (down). System sizes are 100×100 sites (left) and 400×400 sites (right), where black particles are impurities, dark gray monomers, light gray dimers and empty sites are white.

of impurities on the upper-bound transition, has been of great interest in the literature [137, 138, 139, 140, 141, 142, 143, 144, 145]. Two of this studies [138, 140] have shown a complete different behavior on the upper-bound transition for a regular distribution of inert sites and for a random one. It was shown that the second-order nature of the upper-bound does not yield for a regular distribution. Spatial fluctuations of impurity density must be present, and support the claim that a study of spatial correlations can lead to a better understanding of the effect of impurities.

The transition points are computationally demanding to establish due to the critical slowing down when approaching the poisoning transition to achieve the nonequilibrium steady state. The transition points were defined for system sizes of 200×200 with a precision of 10^{-3} for each impurities coverage. The Monte Carlo simulations were carried out for different system sizes and initial concentrations of *inert sites*. Starting each simulation with a *clean substrate* (no impurities present), in which a given coverage of impurities is

initially set, sampling different configurations of impurities (at fixed coverage).

Resorting to the well established idea that at a first-order phase transition correlations remain short range and, in contrast, at a second-order phase transition the correlation length diverges, thus becoming of the size of the system, methods to approach these characteristics are applied. This fundamental difference can be exploited to characterize the order of the phase transition. We, therefore, compute the cluster-size distribution function at the monomer poisoning transition. A similar study for the original ZGB model were done by Kolb and Boudeville [160]. The cluster-size distribution functions are defined as $P(s)$, which is the probability of having clusters with a size s. We develop this idea to the determination of the value of *impurities* coverage θ_{imp}, at which, the upper-bound phase transition changes from a first to a second order.

We proceed to address the nature of the absorbing phase transition at the upper bound, when a random uniform distribution of impurities is present on the surface. As we can see in Figure 2.12a), for values of the coverage below 2.5% the concavity of the cluster size distribution function is downwards. This shape of the distribution function can claim that the size of the larger cluster does not scale with the size of the system. To support this idea, in Figure 2.12b) we simulated systems of linear size of 100, 400, 800, 1600, and 3200 lattice constants at 0% of *impurities*. The cluster-size distribution function present a stretched exponential shape meaning that cluster sizes are small and remain so even if the system size is increased, i.e., the size of the clusters does not scale with the size of the system. For $\theta_{imp} \geq 2.5\%$ in Figure 2.12, the concavity is upwards, i.e., it favors the presence of large clusters. Once again, the dependence of the cutoff of the cluster-size distribution function was monitored: a strong system size dependence is observed. Consequently, cluster sizes scale with the size of the system (See Figure 2.12), and the distribution functions of reactants at the phase transition are mainly characterized by these equations,

$$P(s) = \begin{cases} \exp\left(-s^{\alpha}\right) & \theta_{imp} < \theta_c \\ s^{-\beta} & \theta_{imp} > \theta_c \end{cases}, \tag{2.37}$$

where the exponent α goes to zero for $\theta_{imp} \to \theta_c$.

To identify the transition, one has to identify the particular value of the coverage by *impurities* with zero concavity, where the stretched exponential disappear. To better assess the transition point, the various cluster-size distribution functions were fitted to a second degree polynomial and then compute the concavity of the polynomial function. To prevent poor statistics at the tail of the distribution to influence the determination of the concavity, cluster sizes above 4×10^2 particles were discarded for fitting purposes. The resulting plot of concavity (as provided by the second degree coefficient of the fitting polynomial function) vs. *impurity* coverage can be seen on Figure 2.13. Notice that the value of the crossover from *small* to *large* cluster sizes, is not significantly affected by the system size.

It is possible at this point to estimate the impurities coverage value where the dynamical phase transition changes its nature from first to second order. By the data of Figure 2.13, the critical *impurities* coverage can be considered between 2% and 2.5%.

Since it is proven that long-range correlations are present in the system, the large coverage of reactants near the poisoning of the system for the continuous phase transition will indicate that the system contain clusters that spread all over the substrate. This will mean that the system will undergo also a percolation transition before the complete poisoning by reactants. Since for the case of the first-order phase transition, the correlations are short-range, the size of the clusters will remain small, even near the poisoning point. Taking that in consideration, the above mentioned percolative transition will not occur for the first-order phase transition. This point is shown on Figure 2.14 for the *impurities* coverage of 2% and 3%.

Taking into account these arguments, measuring the percolation properties of the reactant could also indicate the point where the nature of the phase transition changes from first to second order. However, in contrast with the cluster size distribution functions method, computing the percolation transition when approaching the poisoning point has the already discussed problems related with the relaxation time to reach the nonequilib-

rium steady state, which is largely dependent on the distance of the poisoning point and the size of the system. Since the major drawbacks of studying these dynamical phase transitions into absorbing states are the critical slowing down near the transition point and it size dependency position, the use of cluster size distribution functions are presented as a more suitable method, since the measurements can be done only at one position, near the poisoning transition, where the relaxation time is well known, instead of the simulation of an approximation to the transition point where due to the critical slowing down and the size effect the relaxation time increase significantly.

2.5 Conclusions

For the ethanol electro-oxidation case, we introduce a new model for the study of dimers with binary adsorption, where the adsorbing specie can adsorb as either a dimer or a monomer based on the local configuration of the landing site. The properties of the model were studied on a $1D$ and $2D$ system. In the latter case, the proposed model describes the mechanisms of ethanol electro-oxidation on a Pt(100) surface, disclosed by Wang and Liu [23]. Three different cases have been considered: the same deposition rates for dimer and monomer adsorption; preferential dimer site adsorption; different deposition rates. We analytically solved the one dimensional case and studied the two dimensional one through Monte Carlo simulations.

The percolation properties of the adsorbed species reveals that, while monomers percolate at low ratios of dimers/monomers deposition rate, dimers percolate for high ratios. The influence of impurities has also been monitored, disclosing that the coverage of monomers is significantly improved by their presence.

In the present work, we restrict our study to the geometrical properties of the adsorption process. As a follow up, the model can be extended to more complex mechanisms of adsorption where, not only different particle-particle interactions can be considered, but also the long-range interactions typical of large molecules.

On the Ziff, Gulari, and Barshad model with impurities, the results prove that the positioning of the critical point, where the nature of the phase transition changes, is at low values of impurities coverage. This is in conflict with previous works, which describe the critical point as being at a value of *impurities* coverage of 7.8% [139]. These different results can be explained by the fact that the use of the coverage of reactants as the order parameter requires the achievement of a nonequilibrium steady state, which can lead to several difficulties. First, since the size of the system affects the poisoning transition, the system can saturate before reaching a percolative cluster and give a wrong assumption of a discontinuous transition. Second, if the relaxation time is not long enough, the system may not have time to reach a coverage value large enough to contain a percolative cluster.

For these reasons, our method of using the cluster-size distribution function leads to more relevant results than simply using the coverage evolution. Since the shape of the cluster-size distribution functions is related with the spatial correlations in the system, the power-law behavior of the size distribution functions, for the continuous phase transition, indicates that the cluster sizes growth with the system size, being possible to predict even before reaching the transition point, that the spatial correlations of the reactant will scale with the system size. In the other hand, for cluster-size distribution functions of the stretched exponential type, it indicates that even by increasing the system size or by relaxing the system for longer times, the spatial correlations will always remain small.

It is important to refer the role of impurities in the nature of the phase transition, since they are the key feature that allow the monomer clusters to expand themselves all over the system, creating points of support for the cluster to growth. This also shows that it is necessary a finite value of impurities to keep large monomer clusters in the system despite being in the reactive side of the transition.

The motivation for applying these methods, in the context of the Ziff, Gulari, and Barshad model, stems from the existence of these two largely studied irreversible phase transitions of different nature, since the irreversible nature of the transitions forbids the use of more common methods. In our case, these applied methods provided us with a

different value of impurities coverage, on the Ziff, Gulari, and Barshad model, in which the upper-bound transition changes its nature from a first to a second order with the increase of impurities. We contradict the previously approved value of 7.8% of impurities coverage [139], by stating that the value is between 2% and 2.5%.

It is conjectured that this change in the nature of the dynamical phase transition is due to a percolative transition that occurs before the poisoning of the system for values of impurities coverage higher than 2.5%. This property justifies the existence of long-range percolation proper of a percolative cluster that spans the entire system.

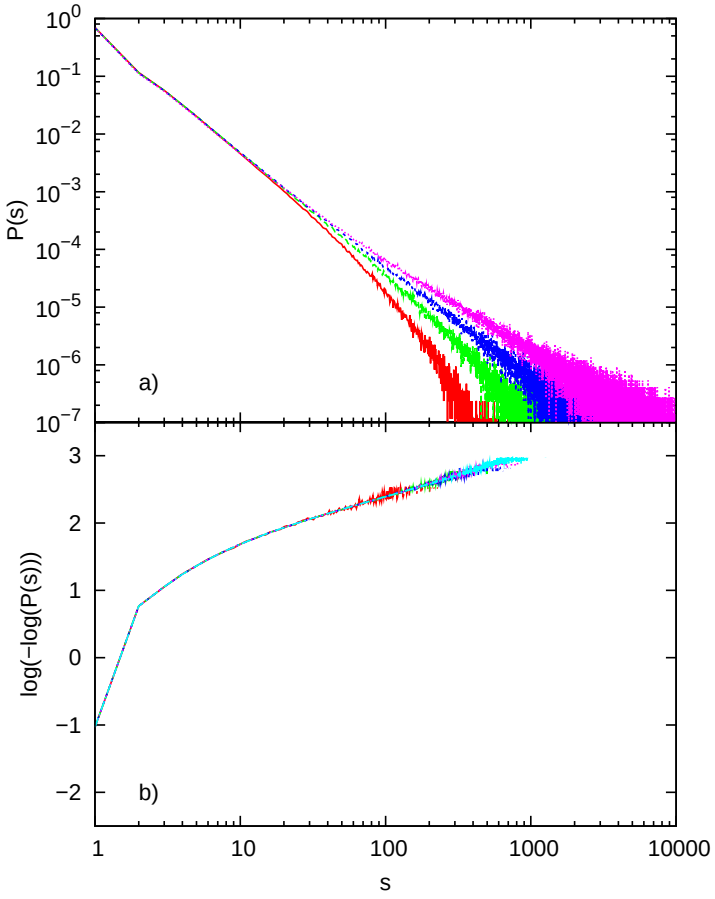

Figure 2.12: Monomers cluster-size distribution functions at the upper-bound transition for: a) different impurities coverage, in a logarithmic scale, for a system of size 800×800 lattice sites. From bottom to top we have 0%, 2%, 3%, and 7.8% of impurities coverage b) for the original ZGB model from the shortest function to the longest we have system sizes of 100×100, 400×400, 800×800, 1600×1600, and 3200×3200 lattice sites in a double logarithmic scale.

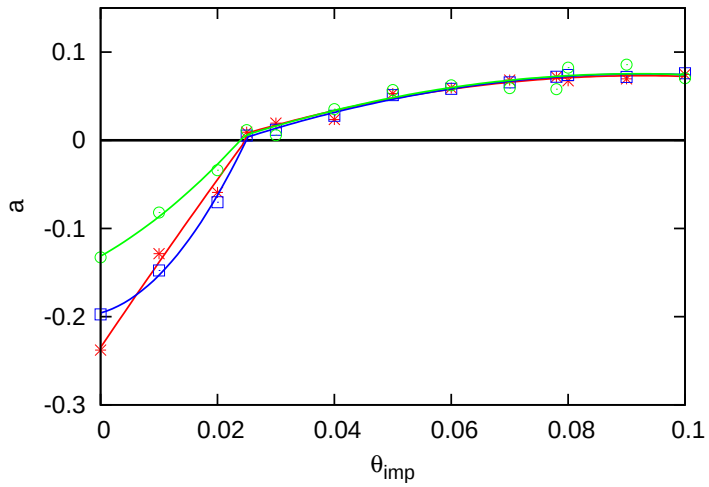

Figure 2.13: Concavity of the cluster-size distribution functions for different coverages by impurities, for systems of size 100×100 (open circles), 400×400 (open squares), and 800×800 (asterisks) lattice sites.

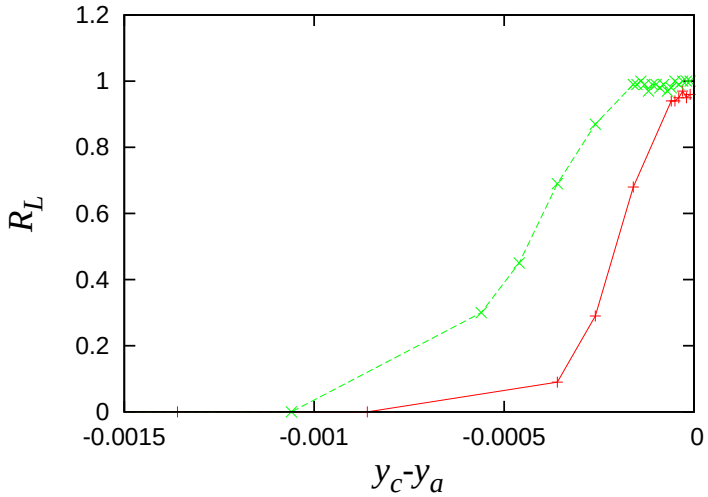

Figure 2.14: Spanning probability R_L as a function of the approximation to the transition point y_c for 2% (right) and 3% (left) of impurities coverage with a relaxation time of 2×10^5 MCS and a system size of 400^2.

Chapter 3

Substrate deposition with relaxation

The growth phenomenon is an intrinsically nonequilibrium problem where deposition events, perturbing the system and keeping it out of equilibrium, compete with relaxation ones leading to equilibrium. Particles arrive to the substrate at a certain flux and hop between different basins, in the energy landscape, through thermally activated processes. Two different characteristic times are then identified, the typical deposition time, related to the flux, and the relaxation time, related to temperature. The ratio between the first and latter is a measure of the nonequilibrium character of the system [161].

The development of several deposition and visualization techniques has challenged scientists to tune the morphology of nanostructures, through the control of the growth conditions. Both experimental [162, 163, 164, 30] and theoretical [165, 166, 167, 168] studies have been performed to identify the main mechanisms leading the process at the atomistic scale. Herein, we introduce a model to study the influence of deposition conditions, namely, the temperature and deposition flux, for multilayer growth.

During homoepitaxial growth, where deposited and substrate particles are of the same type, for temperatures below the roughness transition, the layer-by-layer growth regime is expected with nucleation of subsequent layers only occurring after the previous ones had time to complete. However, if the time between consecutive deposition events is short as compared to the typical timescale for the rate determining processes, then there will

not be enough time to (thermally) equilibrate, on average, between deposition events and growth takes place even further away from equilibrium, since thermal processes leading to relaxation remain unaltered. For example, one can expect island formation on top of existing islands, therefore leading to the nucleation of new layers on top of incomplete ones.

Based on the technological application, different growth regimes are required. For the production of catalysts, rough surfaces with mounds are an advantage [7, 9]. Yet, to obtain highly effective semiconductors, smooth structures should be produced [45]. Understanding how deposition conditions (flux and temperature) lead to different regimes is one of the goals of our work.

During growth, different phenomena occur at different time and length scales requiring different computational techniques. For example, to understand the basic interactions between particles, electronic properties need to be computed [169]. Some local properties resulting from such interactions can be studied through Molecular Dynamics simulations [35, 170]. However, to achieve length and time scales where properties emerging from such interactions are observed, other techniques are required. Typically, stochastic models are developed and implemented with the kinetic Monte Carlo method, where possible processes in the system are identified, together with their rates (computed from the activation barriers) according to which the system evolves [55, 171, 172, 173, 174].

There has been a substantial amount of effort focused on the study of submonolayers deposition, island formation, and island-island coalescence [165, 175, 176, 84, 135, 105], while, for multilayer growth several questions remain open [177, 178, 179, 180, 181]. Typically, either a detailed approach is considered, which attempts to include as many as possible mechanisms [161, 182, 183, 184, 52, 50, 32] or simple models are developed, where mechanisms are restricted to the most relevant ones [31, 28, 26, 185, 51, 48, 186, 187]. In this work, we adopt the latter approach which allows a better understanding of the role of each process in the system dynamics.

Exploring the two parameter space of temperature and deposition flux we, not only,

reproduce several growth regimes previously reported, but we also identify a new one, namely, at low particle mobility. In this new regime, the typical analysis based on surface properties is not able to characterize it since the novel properties belong to the bulk. Besides, the transition between different regimes is also studied.

This chapter is organized in the following way. The model is introduced in Section 3.1. Simulation results are addressed in Section 3.3, along with their discussion. The conclusions are drawn in Section 3.4.

3.1 Model definitions

We introduce a model where the activation barrier of each process is computed based on the one for the terrace diffusion and the coordination number in the initial and final states. This accounts for well known phenomena like, e.g., the *corner rounding* barrier. The neighbor counting approach has some limitations, since a pair-wise interaction is considered, thus neglecting many body effects. However this simplified interactions have successfully been considered in previous studies to address length and time scales of the order of the ones considered in this work [30, 29, 188].

In this model particles are randomly deposited on the substrate. Deposited particles can then hop in the energy landscape between adjacent basins through thermally activated processes. To identify the set of possible processes on the surface and compute their activation barrier, we take the difference between the coordination number in the initial and final positions [50]. In spite of its simplicity, this strategy has been able to grasp relevant phenomena like, e.g., the high vacancy mobility observed in several experiments [189], and the relevance of perimeter mass transport for submonolayer island evolution on Ag(100) substrates [176].

The ballistic rule for deposition implies that deposited particles stick to the first occupied (nearest) neighbor, so particles can overhang [190, 191, 192], as we can see on the Figure 3.1. However, the ballistic deposition model produces too many vacancies,

other models (see for example Ref. [51, 193]) such as solid-on-solid (SOS) and downward funneling mechanism have been considered for deposition [194], are not able to reproduce the experimentally observed vacancies.

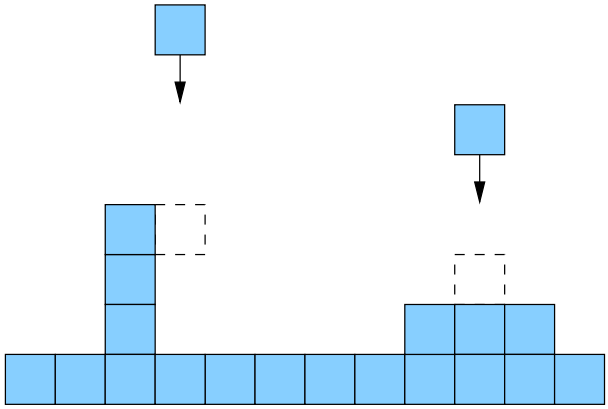

Figure 3.1: Ballistic deposition rule used in the model.

.

3.1.1 Rates calculation

The rate of process i is obtained from the Arrhenius equation,

$$r_i = \nu_i e^{-E_i/k_B T}, \tag{3.1}$$

where ν_i is the attempt frequency. For simplicity the same attempt frequency is assumed equal for all processes, so $\nu_i \equiv \nu$ [195]. The activation energy is,

$$E_i = E_m - (n_f - n_0)J_{pp}, \tag{3.2}$$

where E_m is the activation barrier for terrace diffusion, J_{pp} the energy of the particle-particle interaction, and the coordination number before (after) the hop is n_0 (n_f), as can be seen on Figure 3.2.

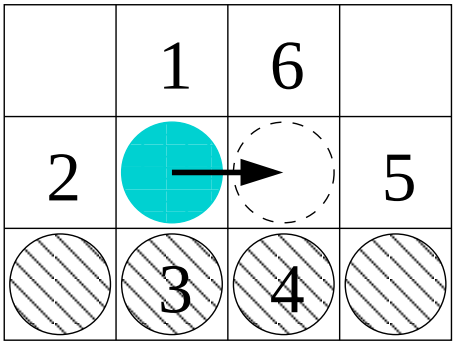

Figure 3.2: Neighbor counting for a mobility process, where 1, 2, and 3 are the neighboring sites before the hop, and 4, 5, and 6, the ones after the hop.

We introduce ϕ as the ratio between binding energy and thermal energy,

$$\phi = J_{pp}/k_B T. \tag{3.3}$$

The attempt frequency for the terrace diffusion process ν_d is defined as,

$$\nu_d = \nu e^{-\frac{Em}{k_B T}}. \tag{3.4}$$

If we characterize a certain material in terms of the ratio, $R_E = E_m/J_{pp}$, between the activation energy for terrace diffusion, E_m, and the pair-wise interaction between particles, J_{pp}, we can rewrite Eq. (3.4) as,

$$\nu_d = \nu e^{-R_E \phi}. \tag{3.5}$$

According to equations (3.1) and (3.5), the rate of a certain process i can then be obtained with,

$$r_i = \nu_d e^{\Delta n_i \phi}. \tag{3.6}$$

The set of parameters in the model can now be reduced to two energetic ones, namely, the ratio R_E and ϕ. The former measures the activation barrier of the terrace diffusion in units of the particle-particle interaction while the latter provides a measure of mobility. The last parameter is the flux (F), defined as the number of impinging atoms arriving at

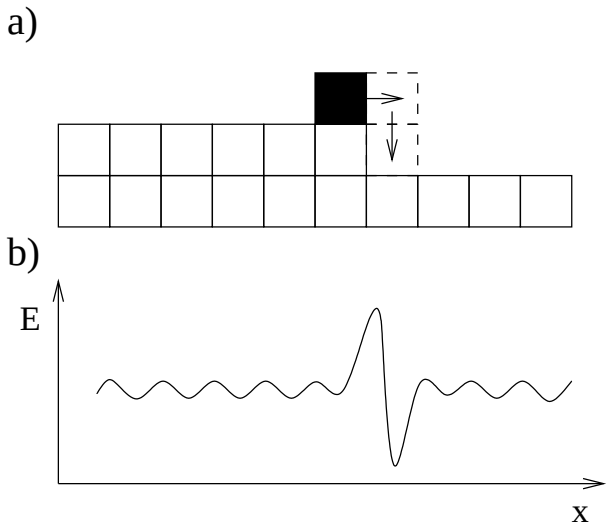

Figure 3.3: a) Scheme of the *corner rounding* process and of the b) energy landscape.

the surface (in the present case a line) per unit of site and time, in monolayers per second (ML/s).

3.1.2 Corner rounding process

A key process in this system is the *corner rounding* [196, 197] as illustrated in Figure 3.3. This process is usually included by considering a direct jump to the step below. An extra parameter is then used for the activation barrier of the jump [183, 198, 194, 196]. In the present model, the rules naturally account for such barrier, with a two steps process.

3.1.3 Preventing evaporation

For epitaxial growth, the particle detachment from the substrate can be neglected [199]. To achieve such constrain, processes which break connectivity to the substrate are forbidden. First, single adatoms have to be prevented to detach from the substrate, as can be seen on Figure 3.4. Second, all cases where clusters break connectivity due to the diffusion of a particle bellow are neglected. To identify these situations we consider the Hoshen-Kopelman algorithm [149]. The Hoshen-Kopleman is based on a cluster coloring

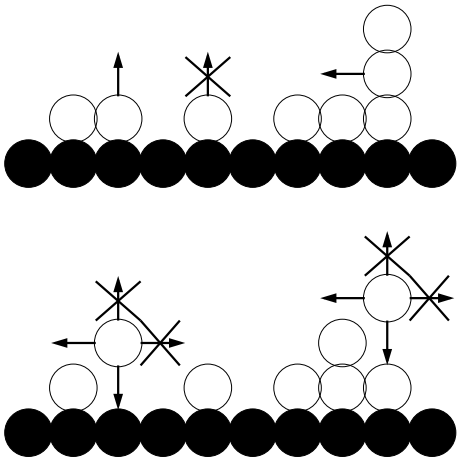

Figure 3.4: Single adatom evaporation prevention.

method, which consists on numbering the individual clusters in the system, as we can see on Figure 3.5.

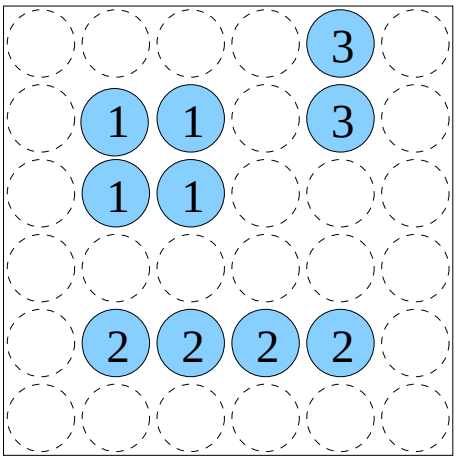

Figure 3.5: Hoshen-Kopelman cluster counting algorithm.

This rule prevent clusters from detaching from the substrate, a mechanism that can be neglected for a large region of the diagram of flux and temperature. Regardless of that, these processes are negligible since the boiling point of these materials is usually very high, and it is only applied to prevent unphysical process common on KMC lattice models. So, by using the Hoshen-Kopelman algorithm, we measure the clusters after the

mobility, as presented in the Figure 3.6. If the neighbor sites to the initial position of the particle are numbered differently, it means that the mobility has broken a connection, leading to a cluster evaporation.

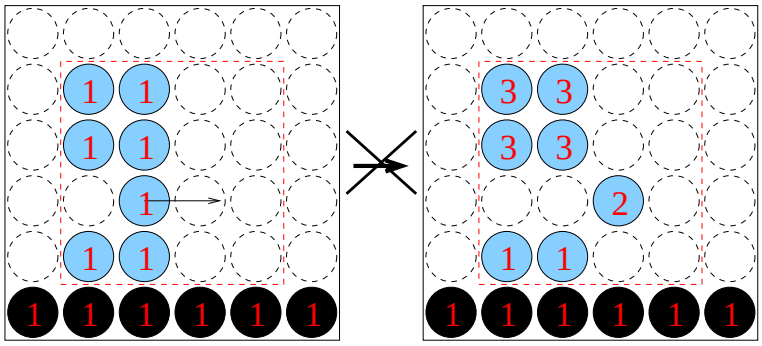

Figure 3.6: Cluster measurement to prevent evaporation.

3.2 Roughness evolution

To study different growth regimes reproduced with this model, we performed extensive kinetic Monte Carlo simulations of a 1+1 dimensional system. Time increment is computed as $\Delta t = -\ln(1-\tau)/\sum_i r_i$, where τ is an uniformly distributed variable in the range $[0, 1[$ and the sum is over all processes accessible to each of the particles, thus giving the total rate of the system. Simulations were carried out with periodic boundary conditions in the horizontal direction. Unless otherwise stated, simulations were performed on a lattice of 10^3 sites and the results were averaged over 10^3 samples.

We now start with the analysis of the effect of the flux of impinging particles in the morphology of the system. We compute the time evolution of the roughness defined as,

$$W(t) = \sqrt{\langle [h(x,t) - \langle h(t) \rangle]^2 \rangle}, \tag{3.7}$$

where $h(x,t)$ is the height of the column x at time t and $\langle h(t) \rangle$ is the average height over all columns at time t.

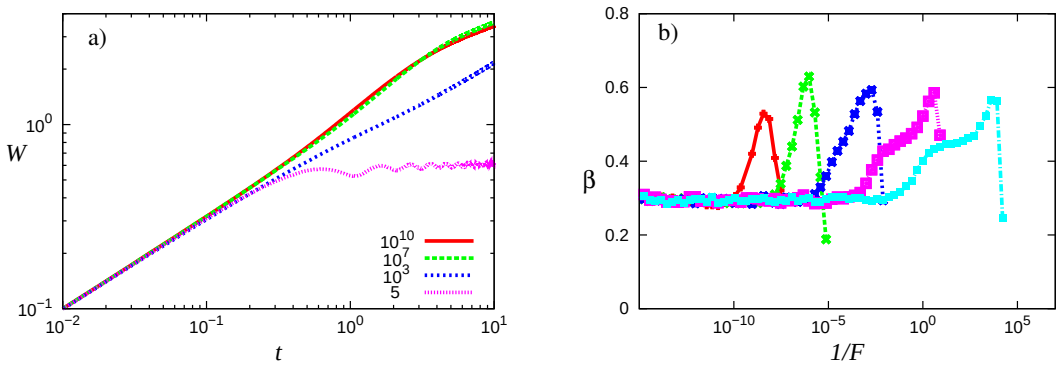

Figure 3.7: a) Roughness evolution at $\phi = 3$ as a function of time defined in units of deposited layers, for $F = \{5, 10^3, 10^7, 10^{10}\}$ML/s. At higher fluxes the growth regime is rough and at lower fluxes the roughness oscillates representing a layer-by-layer growth. b) The roughness exponent β as a function of $1/F$ for different values of ϕ. From left to right $\phi = \{1, 2, 3, 4, 5\}$, measurements performed after 10^2 deposited monolayers.

In Figure 3.7(a) the evolution of the roughness is plotted for different values of F, with $\phi = 3$ and $R_E = 5$. After few deposited layers, different behaviors are observed and limiting regimes can be identified, like e.g., ballistic deposition at high fluxes and layer-by-layer at low deposition fluxes. For a characterization of the different growth regimes at various conditions, the most commonly used measurement is the growth exponent β, given by,

$$W(t) \sim t^{\beta}. \tag{3.8}$$

In Figure 3.7(b), we plot the value of β as a function of $1/F$, for $R_E = 5$ for different values of ϕ. For a fixed temperature (constant ϕ), the inverse of the flux is a measurement of the mobility in the system.

3.2.1 Schwoebel barrier effect

A plateau in the roughness exponent as a function of the flux is observed. Small islands are formed at the level of the first layer and relaxation favors interlayer diffusion [200]. The size of the islands increases with the mobility (inverse of the flux) and the interlayer diffusion diminishes. This effect can be observed on the snapshots of Figure 3.8, where the

first layers of growth are simulated for a 100 lattice sites system. The previous justification of the island size can be proven here, since in Figure 3.8(b), for the roughness plateau, the island size is small, in opposite to the snapshot of Figure 3.8(c), where the islands have a significantly larger size.

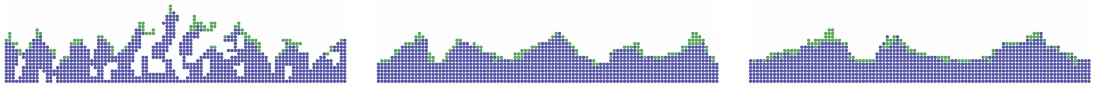

a b c

Figure 3.8: Snapshots of the observed plateau in the roughness with a) first roughness increase, b) roughness plateau, and c) second roughness increase, for a system of 100 lattice sites and 11 deposited layers at $\phi = 4$. Each color corresponds to 10 consecutively deposited layers.

This effect is well known in the literature, as the Schwoebel barrier effect [34, 201, 202, 162, 194, 30, 50, 198], where an extra barrier is found when a particle attempts to diffuse down a step edge. However, in our model, no extra barrier is included. Only the proposed mechanism for corner rounding, where the diffusion process takes into account the number of neighbors before and after the hop. This brings a different perspective over the studies of Schwoebel barrier, where here we propose that the barrier comes only from the difference in neighbors interaction for the corner rounding process.

Another curious behavior arises from the fact that at low values of the ratio between interaction and thermal energy, ϕ, the plateau previously presented is well decreased, as can be seen for the lines of $\phi = 3$ and $\phi = 5$ on Figure 3.7(b). This can explain the various values of the Schwoebel barrier effect for different materials.

3.3 Growth regime transitions

At low mobility, the system approaches the ballistic deposition (BD) regime, characterized by shadowing of lower layers due to the overhanging of particles. As the mobility

increases, a relaxation of these particles is promoted and the roughness increases - we denote this regime as ballistic deposition with local relaxation (BDLR). When the density of vacancies vanish, the regime where nucleation of new layers before the complete nucleation of the ones below is observed - which leads to an increase in the roughness exponent - corresponds to the kinetic rough (KR) regime. For low values of flux (higher mobility), the system as enough time to relax between deposition events and a layer-by-layer growth (LBL) is observed [191]. Snapshots of different regimes are shown in Figure 3.9.

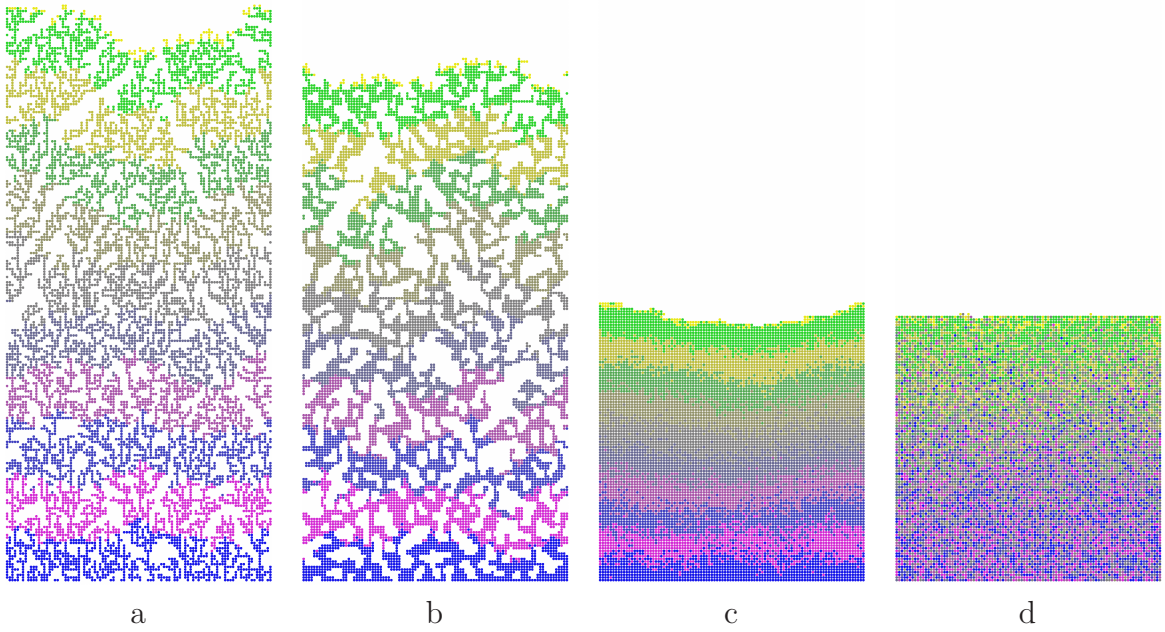

Figure 3.9: Snapshots of the different growth regimes a) BD, b) BDLR, c) kinetic rough, and d) layer-by-layer, for a system of 100 lattice sites and 100 deposited layers at $\phi = 3$. Each color corresponds to 10 consecutively deposited layers.

In the following subsections, these different transitions and their growth regimes are discussed. First, the transition from BD to BDLR is addressed, then the one from BDLR to kinetic rough growth, and finally the transition from kinetic rough to layer-by-layer growth. This section is closed with the characterization of the thermal roughening transition.

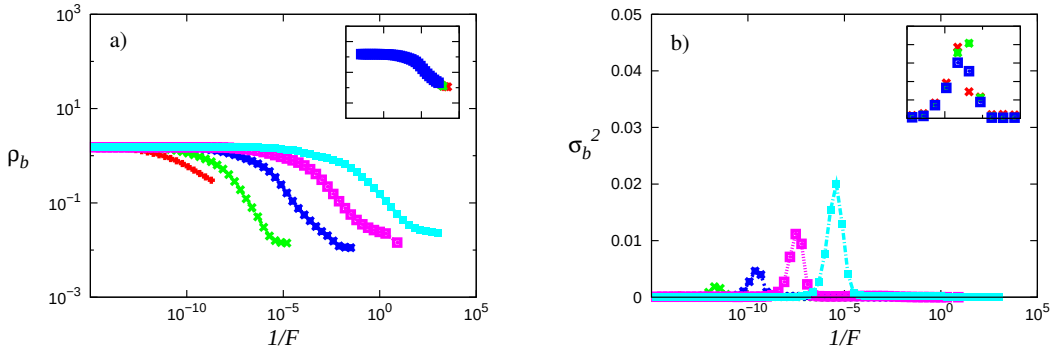

Figure 3.10: Density of dangling bonds (a), ρ_b, and its variance, σ_b^2, (b) as a function of $1/F$ for different values of ϕ after 100 deposited layers. From left to right, $\phi = \{1, 2, 3, 4, 5\}$. The insets are at $\phi = 3$ and for different system sizes of L=$\{400, 1600, 3200\}$.

3.3.1 BD to BDLR

At high fluxes or low temperatures, two growth regimes are present, BD and BDLR, which differ by the presence of diffusion solely in the BDLR regime. However, this mobility is very low and, mainly, particles hop to neighboring sites with higher coordination (processes with lower activation barrier according to Eq. (1.23)).

Despite similar behavior of the roughness for both regimes, the snapshots in Figure 3.9 reveal different bulk structures. Therefore, the typical analysis based on the roughness exponent [47] is useless to differ them. Since the coordination is higher in the BDLR regime, in Figure 3.10(a), we analyze the behavior of the density of dangling bonds (bonds to empty sites) given by,

$$\rho_b = \frac{N_b}{LN_l}, \tag{3.9}$$

where N_b is the number of dangling bonds, L is the linear size of the system, and N_l is the number of deposited layers.

In Figure 3.10(a) a constant density of dangling bonds is observed for higher fluxes which decreases at lower fluxes. The point where the transition from constant density of dangling bonds to lower values occurs, depends on the mobility of particles, which is fixed

in these results, but could shift in the thermodynamic limit since with an increasingly higher number of deposited layer, the mobility will be present at any non-infinite flux. An interesting behavior is found for the variance of the density of dangling bonds (σ_b^2) in Figure 3.10(b), given by

$$\sigma_b^2 = \langle(\rho_b - \langle\rho_b\rangle)^2\rangle. \tag{3.10}$$

A maximum is observed, which can be taken to pin down the transition from BD to BDLR. A non-vanishing maximum with the system size (inset of Figure 3.10(b)) is a sign of a discontinuous transition in the thermodynamic limit [203]. Besides, the peak for the second moment evinces with ϕ meaning that the jump intensifies with the mobility decrease. Snapshots of the system before and after the transition are presented in Figures 3.9(a) and 3.9(b).

3.3.2 BDLR to kinetic rough

When lowering the flux, the diffusion increases and particles placed on overhanging positions hop to more stable positions, due to a larger relaxation time between deposition events. This behavior reduces the shadowing effect characteristic of the BD and, consequently, an increase in the roughness is observed (see Figure 3.7(b)). The number of overhanging particles is reduced, which means that the density of vacancies in the film also decreases. We measure this density, given by,

$$\rho_v = 1 - \frac{N_l}{\langle h\rangle}, \tag{3.11}$$

where N_l is the number of deposited layers, and plotted it, as a function of $1/F$ in Figure 3.11(a). A transition on ρ_v from 0.5, characteristic of the BD regime, to near 0 in the kinetic rough regimes is obtained. As previously stated, the BDLR density of vacancies does not differ significantly from the BD one, due to the shadowing. Figure 3.11(b) shows

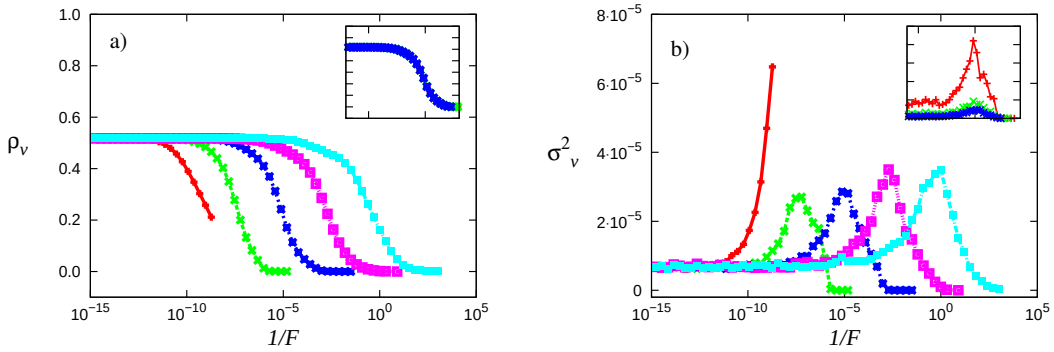

Figure 3.11: The density of vacancies (a), ρ_v, and its variance (b) as a function of $1/F$ for different values of ϕ after 100 deposited layers. From left to right, $\phi = \{1, 2, 3, 4, 5\}$. The insets are at $\phi = 3$ and for different system sizes of L=$\{400, 1600, 3200\}$.

the variance of the density of vacancies

$$\sigma_v^2 = \langle(\rho_v - \langle\rho_v\rangle)^2\rangle, \tag{3.12}$$

where the average is over all samples. A maximum is observed, at the transition point from the BDLR to kinetic rough growth, which, corresponds to the maximum of the roughness exponent in Figure 3.7(b). The maximum vanishes in the thermodynamic limit, being a sign of a continuous transition (inset of Figure 3.11(b)) [203]. Snapshots of the system before and after the transition are presented in Figures 3.9(b) and 3.9(c).

3.3.3 Kinetic rough to layer-by-Layer

Another relevant transition reproduced by this model is the kinetic roughening transition between layer-by-layer and kinetic rough growth. The transition point can be computed by extrapolating in Figure 3.7(b) the flux F, when the growth exponent, β, goes to zero. Snapshots of the system before and after the transition are in Figure 3.9(c) and 3.9(d).

In Figure 3.12(a), the transition points from kinetic rough to layer-by-layer growth can

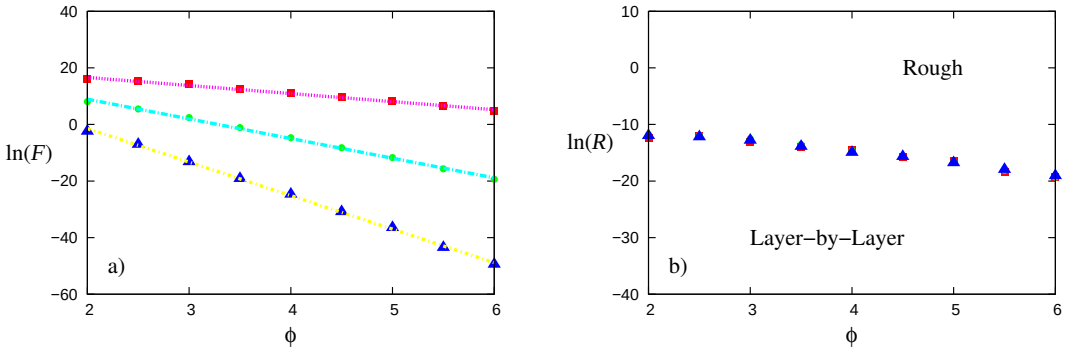

Figure 3.12: Growth mode diagram with the kinetic roughening transition between Layer-by-layer to Kinetically Rough growth. a) The flux as a function of ϕ for values, from bottom to top, of $R_E = 10$, $R_E = 5$, and $R_E = 1$. b) The ratio R as a function of ϕ where the symbol (Triangle) is $R_E = 10$, (Circle) is $R_E = 5$, and (Square) is $R_E = 1$.

be observed. In agreement with previous work [192, 191], the transition has an Arrhenius dependency of the flux over the inverse of the temperature. For different values of R_E (Figure 3.12(a)), different slopes of the Arrhenius exponential function, representing the kinetic roughening transition, are observed. To generalize, the flux is rescaled in unities of the terrace diffusion process, ν_d. A ratio (R) is then defined to relate the flux of particles (F) and the terrace diffusion rate (ν_d),

$$R = \frac{F}{\nu_d}. \tag{3.13}$$

The ratio R is represented on Figure 3.12(b) by a growth mode diagram as a function of ϕ and different values of R_E. The transition has now the same behavior independently of the R_E value, which indicates, within the limits of this study, a material independent transition. Unlike the previous cases, for this transition a finite-size study has not been considered since the Layer-by-layer regime is an initial transient regime, which, for long enough time scales or large enough system sizes, eventually crosses to the Kinetically Rough regime [49].

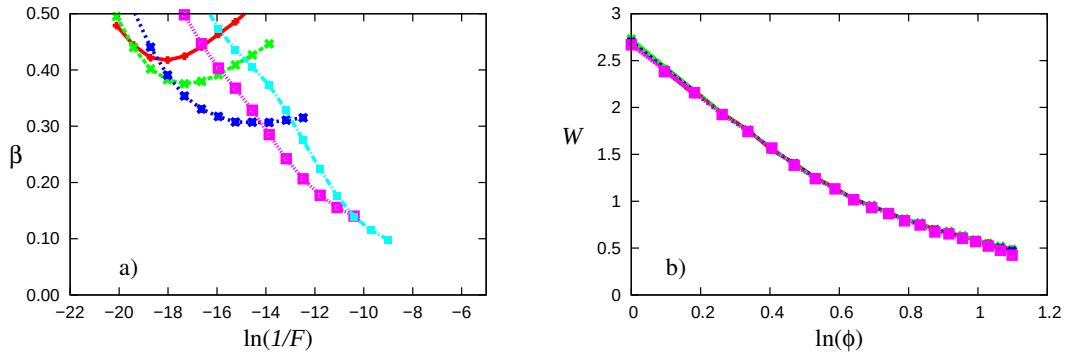

Figure 3.13: a) Growth exponent evolution as a function of $1/F$ for various ϕ values near ϕ_c. From bottom to top we have $\phi = \{2, 1.8, 1.4, 1.2, 1.1\}$. b) Roughness as a function of the temperature for lattice sizes, from bottom to top, of 100, 200, 400, 1000 and 2000 on a previously deposited film of 10 ML.

3.3.4 Thermal roughening transition

The transition reported above is of nonequilibrium nature, though, a roughening transition can also occur under equilibrium conditions, known as thermal roughening or equilibrium roughening transition [168]. To study this transition two different approaches are considered since it does not occur due to nonequilibrium effects like previous ones. We first consider its influence on the kinetic roughening transition (Figure 3.13(a)) and we then systematically study the behavior of an initially smooth surface at different temperatures (Figure 3.13(b)).

The transition to the layer-by-layer regime is observed for a wide range of ϕ values, however, in Figure 3.13(a), bellow a certain value of ϕ, the growth exponent does not converge to zero, i.e., the transition to a layer-by-layer growth does not occur. In fact, the roughness exponent β diverges at values of $\phi < 2.0$, which can be interpreted as a critical ϕ_c, below which layer-by-layer regime is no longer observed.

To systematically study this equilibrium transition we consider an initial flat surface with 10 layers and let it evolves, for different values of ϕ, to a constant roughness. Figure 3.13(b) is the roughness as a function of ϕ for different system sizes. The roughness of the system increases logarithmically bellow the transition point ϕ_c.

A relation can now be established between the thermal roughening temperature, T_{tr}, and the one from the kinetic roughening, T_{kr}. This can be deducted from Figure 3.12(b), and the thermal roughening transition relation $\phi_c = J_{pp}/T_{tr}$. Which can be represented by,

$$F_c = A\nu_d \exp\left(-\frac{\alpha\phi_c T_{tr}}{T_{kr}}\right), \tag{3.14}$$

where A and α are independent of the temperature and flux, solely depending on R_E. This equation fits the plots of Figure 3.12(a), where the Arrhenius dependency of the flux over the temperature is observed. To reduce the dependency of Eq. (3.14) on R_E, the ratio R (Eq. (3.13)) is used, leading to the relation,

$$R = B \exp\left(-c\frac{T_{tr}}{T_{kr}}\right), \tag{3.15}$$

where B and c are constants. In Figure 3.12(b) are the same lines of Figure 3.12(a) with the proposed scaling relation.

3.3.5 Growth mode diagram

Obtained results are summarized in Figure 3.14. The diagram represents, for different pairs of ϕ and F, the corresponding growth regime. BD/BDLR and BDLR/KR transition lines were picked from Figures 3.10(b) and 3.11(b), respectively. For the KR/LBL and thermal roughening transition results from sections 3.3.3 and 3.3.4 were considered. The diagram of Figure 3.14 represents the observed growth modes and the transition lines between them.

3.4 Main conclusions

We presented a kMC model to study the influence of both the flux and temperature on the epitaxial growth. We simulated 1+1 dimensional ballistic growth with thermally ac-

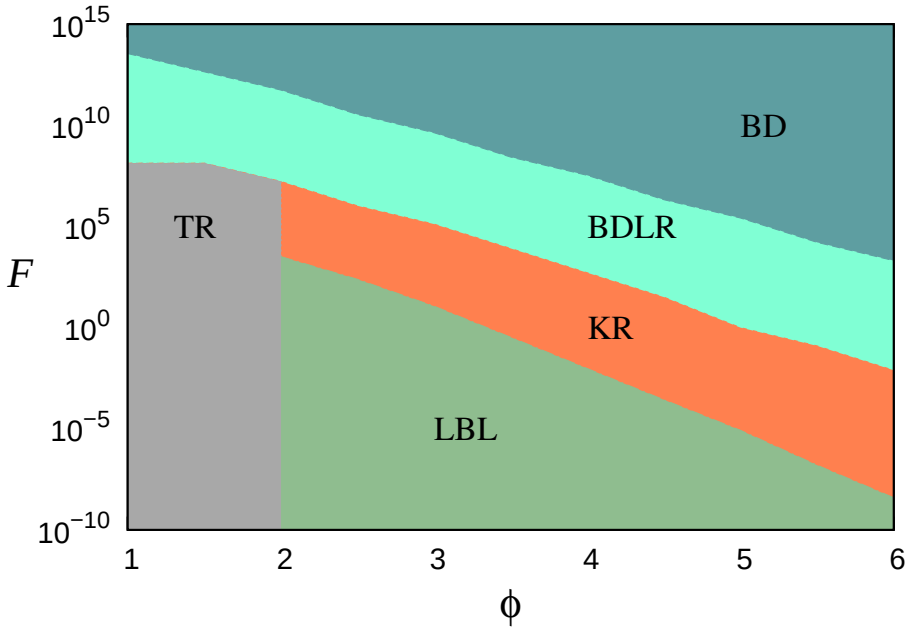

Figure 3.14: Final growth mode diagram, where TR and KR are the *Thermally Rough* regime and *Kinetically Rough* regime respectively.

tivated relaxation processes. In this work, despite the simplicity of the neighbor counting procedure, already known regimes are reproduced like, e.g., ballistic deposition, kinetic rough, layer-by-layer, and thermal rough growth. A new regime between BD and KR is identified, which we name as ballistic deposition with local relaxation (BDLR). Despite the similarities in the surface structure with the BD growth, significantly different bulk properties were found.

We studied the transitions between the identified regimes with emphasis on the BD/BDLR and BDLR/KR ones, where the traditional surface properties analysis is meaningless and a study of the bulk properties is needed. The transition KR/LBL was also studied and an Arrhenius relation of temperature and flux postulated. Besides, we extended the postulated relation to map from the temperature of the thermal and kinetic roughening transitions.

Understanding the scaling properties of the new regime and the influence of the deposition conditions in the vacancies distribution, are some of remaining the open questions.

Our model can also be straightforwardly extended to 2+1 dimensions where new regimes can be identified. Besides, by considering different pair-wise interactions between different species, it is possible to study heteroepitaxial growth, when the elastic energy is neglected.

Chapter 4

Growth of nanoclusters

Since the advent of nanosciences, clusters of nanometer size have played a relevant role [204, 17, 20]. These clusters, named nanoclusters, are by definition, aggregates of atoms or molecules of various sizes and compositions at the nanometer scale. The particles that constitute these nanoclusters can interact in different ways, from Coulomb interaction for charged ions, covalent or metallic bonds, to van der Waals type. Based on their constitution, they can be classified as homogeneous (one type of particles) or heterogeneous (various types of particles).

Nanoclusters are a challenge *per si*, since they have distinct properties from bulk or individual atoms. The properties of a cluster show strong size dependence [204, 20] and, even clusters of the same size, but different morphology (isomers), may differ in their main properties [204, 17]. The properties of nanoclusters can also be controlled by the mixture of different types of atoms (nanoalloys) [19].

On what concerns applications, nanoclusters have a wide range of technological utility, due to their unique properties of catalytic [205] (high surface-to-volume ratio), optical, electrical, magnetic, and mechanical nature. A great challenge is present on the implementation of nanoclusters on miniaturized electronic devices [18], and also their interaction with soft matter has been extensively studied [206]. Besides, their inclusion in a matrix of a certain material to change its mechanical, electrical, and/or thermal properties has

also been a main focus of research [207, 208, 209].

The chapter is organized as follows: in Section 4.1 an introduction to free nanocluster growth is given with both theoretical and experimental approach. On Section 4.2 our model for cluster growth and the methods of analysis are presented. The results and discussions are given on Section 4.3 and the conclusions drawn on Section 4.4.

4.1 Free nanocluster growth

Historically speaking, the experimental creation of free nanoclusters was first done 30 years ago, with the growth of noble-gas clusters [20]. The growth of metallic clusters was only accomplished 10 years later. Since then, cluster growth technology has largely evolved, due to the introduction of UHV-compatibility, the possibility of binary metal clusters production, and the emergence of more efficient mass-selection techniques [21].

The main theoretical approach to the study of nanoclusters has been on their structures, since it dictates the clusters properties. The effects considered in the literature, as being behind the growth of a specific nanocluster structure are of energetic, thermodynamic, and kinetic type [17]. Energetic effects on cluster structures are related with finding the structure that minimizes a cluster total energy, which depends on the potential-energy surface (PES). The PES is the energy landscape of a cluster, with barriers and basins that depend on particles position [17]. The most stable structure is the one with the global minimum on the PES. The thermodynamic effects are related with the influence of temperature on the cluster structure [17, 210]. Finally, the kinetic effects, which are the ones that depend on particles deposition conditions, where the time between deposition events, during growth, influence the final structure of the cluster [20]. The main focus of our study will be on the kinetic effects, where the relevance of both temperature and flux of particles is taken into account, since typically growth conditions are such that the system has not enough time to attain the equilibrium configuration between successive deposition events.

Despite the importance of the kinetic effects of deposition, energetic studies are of interest to understand which are the most common structures at a specific size. Mainly the occurrence of "magic" structures, of great stability. To find these structures, using energetic studies, it is first necessary to consider particles interactions, by solving the Schrödinger equation for the electronic interaction (*ab initio*) [211, 212, 204], using molecular dynamics [39, 213, 37, 38, 214, 17], or Monte Carlo simulations [215, 36]. In all cases, the challenge is the search of the most stable isomer at a specific size. For *ab initio* studies, the cluster sizes are limited to few particles, since these are very computationally demanding methods. So, the use of global optimization algorithms [17] for the search of the preferred isomer, can be presented as the best option. Both molecular dynamics and Monte Carlo methods can be used, and present similar efficiency [20]. Molecular dynamics methods are more widespread, and various potentials like Lennard-Jones [38], Sutton-Chen [213], or EAM [39], are used.

From these optimization methods, the so called "magic" sizes are found. These are cluster isomers with the most energetically stable structure on a specific range of sizes [214, 37, 216]. Some magic sizes for Cu clusters can be observed on Figure 4.1. The objective of the study of these "magic" sizes, rely on predicting the structures formed during cluster growth. However, despite being the most stable structures at specific sizes, they are frequently not found on experimental realizations. This occurrence give even more arguments to the consideration of kinetic effects during cluster growth.

So, since these kinetic effects are our main interest, it is important to review the common experimental technique used to growth free nanoclusters. This technique, called the vapor cluster growth can be divided into three stages [212, 217, 21]: creation of a hot vapor of the material, super-saturation, and detection of the clusters. The heating methods for the hot vapor are mainly: heating in a crucible, targeting with a laser pulse, or hitting with a ion beam. To obtain the supersaturation from the hot vapor, supersonic expansion or collisional thermostat are used. For the supersonic expansion, the vapor is mixed with a high pressure inert gas, where it is expanded. This method produces clusters at high

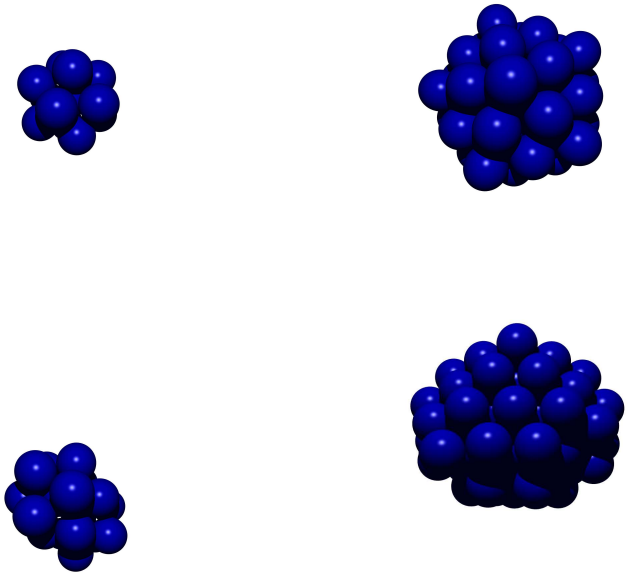

Figure 4.1: Some magic sizes for Cu cluster, at sizes of 13, 19, 55 and 75.

temperatures (near evaporation). The collisional thermostat consist on mixing the vapor with a cold inert-gas flow, producing low temperature clusters. In this case aggregation proceeds mainly through the addition of single atoms, where re-evaporation is negligible. This is the experimental method simulated in the present work. The experimental apparatus ends with cluster detection methods, like e.g., diffraction methods or mass-selective detection of ionized clusters, that are deposited and then observed by microscopy.

Important experimental realizations have been done to study the kinetic effects on metallic clusters growth. Growth of Cu and Ag clusters by Reinhard *et al.* [218, 219], produced by inert-gas aggregation and analyzed by electron diffraction, have been performed to study the influence of the growth conditions of pressure and temperature on the morphology of the clusters. Different structures have been identified at different sizes and growth conditions. Their main conclusions rely on the existence of large Ag icosahedra clusters [218] when energy considerations predict FCC structure, suggesting that clusters remain kinetically trapped, during growth, on icosahedral structures. It was also found that cluster structures are influenced by the growth conditions, where the tuning of the

pressure and the temperature affects the production of FCC or icosahedral structures. For the case of Cu clusters [219], the transition from icosahedra to FCC was found at sizes of the order of 3.8 nm.

Kinetic effects must be taken into account, since the effect of deposition is extremely relevant and kinetically trapped structures can occur. To study these effects, from the theoretical point of view, solid-state growth models are considered, where different potentials are used and simulations of the free nanoclusters are performed, mainly, with molecular dynamics. Two types of computational studies are commonly used when studying kinetic effects: freezing of nanoclusters, where clusters are formed at very high temperatures (above the melting point) until they reach the desired size and then are cooled down to a solid state. The second type occurs at relatively low temperatures, and is simulated by aggregating particles at a specific flux to an initial seed. This way, the nonequilibrium effects brought by the deposition process are taken into account. This second type will be the one used in our work. Molecular dynamics simulations of kinetically trapped structures have been performed on different materials and cluster sizes, like for instance, small Ag clusters [220, 221] (less than 150 atoms), intermediate and large Ag clusters [222] (up to 600 atoms), or even clusters of C_{60} molecules [223].

This simulational methods have been efficient on predicting experimental cluster growth, in opposite to energetic studies. Physical problems like the emergence of large icosahedral clusters instead of FCC, have been addressed, where a transformation from a decahedron into a icosahedron has been shown, with the shell-by-shell growth into larger icosahedron clusters. Also interesting phenomena like reentrant morphologies at different conditions, like at intermediate values of temperature in Ag clusters [220] or for the cluster size of 38 atoms of Ag and Cu [216], have been predicted by these methods.

4.2 Vapor Cluster Growth Model

As previously stated, our growth model attempts to simulate the inert-gas aggregation method, where particles aggregate on an initial seed. Re-evaporation is not allowed since clusters are bellow the melting temperature [212], which in the case of metallic clusters is well bellow the boiling point. The main aspect of this computational technique is the fact that the deposition is simulated by Molecular Dynamics, however, the relaxation of clusters is done through the technique of Temperature Accelerated Dynamics, presented on section 1.4.

4.2.1 Deposition Model

State-of-the-art models for clusters growth consider particles addition by collision towards the cluster center with a flux which does not depend on the actual cluster size [20]. However, the randomness of clusters and particles motion and the dependence of the flux on the cluster size are two relevant features which we include in the model.

We deduce the flux by starting with an ideal gas approximation $PV = nRT$, where P is the pressure, V the volume of the chamber, n the number of moles of molecules, R the ideal gas constant, and T the temperature. We then compute the number of particles that collide with a area A, in a time interval of Δt. Considering a cylinder of length $v_x \Delta t$, the number of particles N_p inside that same cylinder is given by,

$$N_p = \frac{N}{V} A v_x \Delta t, \tag{4.1}$$

where N is the total number of particles in the chamber and v_x the velocity of particles in the xx axis. Since the number of particles with velocity v_x is given by $dN_{v_x} = N_p f(v_x) d_{v_x}$ [74], we have,

$$dN_{v_x} = \frac{N}{V} A v_x \Delta t f(v_x) d_{v_x}, \tag{4.2}$$

where $f(v_x)$ is the velocity distribution function in the x direction. Accounting only for

the velocities in the positive direction in x,

$$\int_0^{+\infty} dN_{v_x} = \frac{N}{V} A\Delta t \int_0^{+\infty} v_x f(v_x) d_{v_x}, \tag{4.3}$$

where $< |v_x| >= \int_{-\infty}^{+\infty} v_x f(v_x) d_{v_x}$ and the system is isotropic (no field applied), $f(v_x)$ is a even function, so $< |v_x| >= 2\int_0^{+\infty} v_x f(v_x) d_{v_x}$. Applying to Eq. 4.3, the number of collisions with A in the time interval Δt is given by,

$$N_{v_x} = \frac{N}{V} A\Delta t \frac{< |v_x| >}{2}. \tag{4.4}$$

Knowing that $< |v_x| >= \frac{1}{2} < |v| >$ [75], the flux is,

$$\phi = \frac{N_{v_x}}{A\Delta t} = \frac{N}{4V} < |v| >, \tag{4.5}$$

where $< v >$ is the average velocity of particles in any direction.

Taking into account that $N = nN_A$, from the ideal gas equation and Eq. 4.5 we have,

$$\phi = \frac{PN_A < |v| >}{4RT}, \tag{4.6}$$

replacing the average velocity $< |v| >= \sqrt{\frac{8k_BT}{\pi m}}$ [75], for a spherical cluster we can assume the flux of impinging atoms as,

$$\phi = \frac{PA}{\sqrt{2\pi k_B T m}}. \tag{4.7}$$

Now that we have an equation of the flux as a function of the cluster surface, we can compute the flux by considering the area of a sphere around the cluster (see Figure 4.2). Here, the sphere has a radius equal to the radius of the cluster plus the value of the cut-off distance (Rc). This cut-off is the distance above which the interaction can be neglected such that, a truncation on the potential may be considered. All deposited particles will be released at this distance in accordance to the flux. To represent the random character of the motion of the gas particles, when an impinging atom is placed on a random position

of the sphere surface, the direction of that same atom is randomly generated, as can be seen on Figure 4.2. One interesting aspect is that if the angle θ, between the direction of the atom and a vector towards the center of the cluster, is larger enough, the model accounts for the possibility of the particle missing the collision with the cluster.

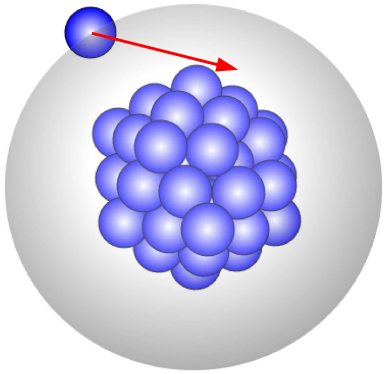

Figure 4.2: Scheme with the sphere used to compute the flux, and the representation of the randomly generated direction of impinging atom.

Summarizing, the main advantages of the model relies on the fact that particles do not arrive at the cluster only pointing at the center, preventing a tendency for spherical clusters, the flux of particles depends on the size of the cluster, and the relaxation between deposition events is simulated trough Temperature Accelerated Dynamics, which boost largely the computational efficiency (mainly at low temperatures). The potential considered for the particles interaction is the EAM potential [96], since the material to be studied is copper.

4.2.2 Methods of Analysis

One difficulty when studying clusters, is related with the similarities between the non-crystalline structures that characterize them. The simplest strategy would consider solely the distribution of particle-particle distances but significantly different structures are characterized by similar distributions. Therefore, the method of analysis is extremely

important for a correct study of nanocluster structures.

Despite previously stating that energetic studies of clusters are not the right ones to take into account all physical phenomena, a calculation of energy is still necessary to allow the pointing out of the structure stability. To classify the different structures, the Common Neighbor Analysis is used, which by mapping relations between particles and their neighbors, allow a good identification of the different structures.

Energies Analysis

For the classification of clusters by their stability, the energy of the cluster is computed. However, clusters have similar energies, even at different sizes. For that, a variable is introduced that calculate the relative energy of the cluster, taking into account its volume and the bulk cohesive energy of the material. This variable Δ is defined by the following equation [224],

$$\Delta = \frac{E_{tot} - NE_{coh}}{N^{\frac{2}{3}}}, \tag{4.8}$$

where E_{tot} is the cluster energy, N is the number of atoms, and E_{coh} is cohesive energy per atom on the bulk of a crystal made of the same material. This variable is a helpful way to identify the most stable isomer at a specific size, and it can show the different "magic" sizes of clusters of a specific material.

Common Neighbor Analysis

The Common Neighbor Analysis (CNA) method consists on the study of the connections between common neighbors of a pair of neighbors [225]. To define the distance of first neighbors it is necessary to study the distance distribution function between atoms of the cluster, where the first peak of the distribution function is the distance of the first neighbor. Then, a value of distance $r < r_1$ is used to be considered first neighbors, where r_1 is the position of the first minimum on the distance distribution function previously calculated.

After identifying a pair of first neighbors and their common first neighbors, we count

the connections between those first neighbors. The next step is to classify those values of first neighbors and connections into three indexes jkl. The index j is the number of common neighbors, represented on Figure 4.3a), index k is the number of connections between common neighbors, shown on Figure 4.3b), and the index l is the longest connection between those common neighbors, which can be seen on Figure 4.3c). The probability of finding pairs of first neighbors, P(j,k,l), with some specific combination indexes is then computed.

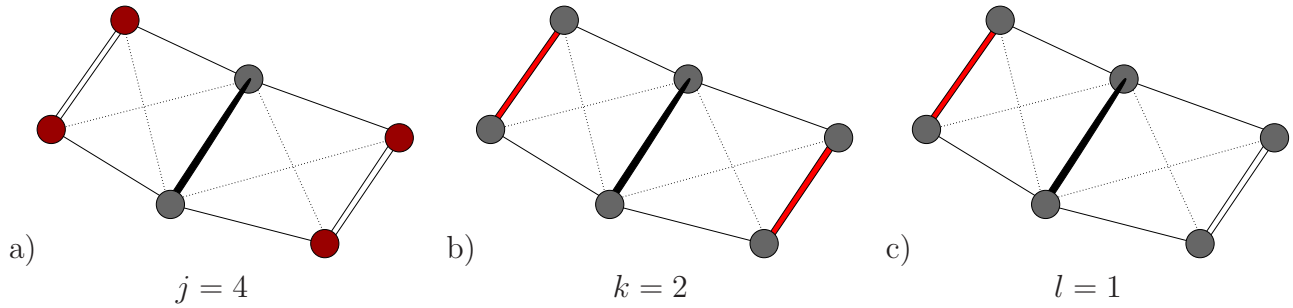

Figure 4.3: Scheme of the CNA index representation.

It was found in the literature that the values of P(5,5,5), P(4,2,1), and P(4,2,2) are enough to differ the cluster structures of the type Icosahedral, Decahedral, and FCC [222, 20]. This indexes can be observed on Figure 4.4, where the P(5,5,5) represents the fivefold symmetry common on the Icosahedral structures, which should be a high value for icosahedral, and null for the FCC. The index P(4,2,1) is the one related with atoms in a FCC structure, which should be high for those same structures. In Table 4.1 the values of these CNA indexes for some perfect structures at "magic" sizes are presented [222]. This table can be used as a guide to identify structures during the cluster growth.

4.3 Structures Formation

Despite the large number of previous studies on the influence of the temperature on cluster growth [20], a systematic study on the dependency of the cluster structure with the flux as not yet been done. Our advantage is, by relaxing the system through TAD,

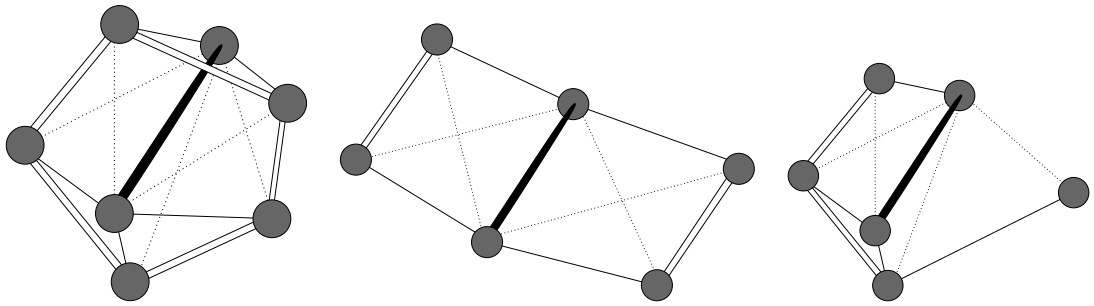

a) P(5,5,5) b) P(4,2,1) c) P(4,2,2)

Figure 4.4: Scheme of the classification of connection between common neighbors.

the possibility to simulate very low fluxes of particles (near experimental conditions). For that, lower temperatures are consider what is tailored for TAD since the lower the temperature the more efficient the technique.

In this section, we will first present the estimation of the boost on performance given by the use of the TAD technique on cluster growth. This technique has not been used yet on the growth of nanocluster, so this analysis could bring some enthusiasm on the application of this method for the growth of clusters of various materials. We will then, present the different structures grown at various temperatures and fluxes, and also study the influence of the deposition process, on the final structure formation. We will finally use the possibility given by the TAD technique of saving all energy barriers overcome during the growth and study their values for each type of obtained structures.

4.3.1 Computational boost

The main objective of these type of Accelerated Molecular Dynamics methods is to increase the computational efficiency, allowing to simulate larger system sizes and longer physical time scales.. So, despite TAD having other useful aspects for the study of these type of physical systems, knowing the boost factor given by the method is also relevant. In this case, the boost factor is defined as the simulation time at the lower temperature given by TAD, divided by the amount of physical time simulated with MD using the

Table 4.1: CNA analysis for different magic numbers, where Dh are decahedral structures, Ih are Icosahedral, and TO truncated octahedral.

N	P(5,5,5)	P(4,2,1)	P(4,2,2)	Structure
75	1.25	28.2	20.4	(2,2,2)m-Dh
100	0.92	27.6	19.6	(3,1,2)m-Dh
101	1.12	33.7	20.2	(2,3,2)m-Dh
146	0.75	39.6	18.7	(3,2,2)m-Dh
192	0.66	45.3	18.2	(3,3,2)m-Dh
212	0.60	44.7	16.4	(2,2,3)m-Dh
238	0.61	48.6	18.0	(3,4,2)m-Dh
247	0.51	47.2	16.9	(4,2,2)m-Dh
268	0.54	48.6	15.8	(2,3,3)m-Dh
318	0.45	52.5	16.3	(4,3,2)m-Dh
55	10.3	0.00	38.5	Ih
147	5.12	17.2	38.8	Ih
309	3.10	31.0	34.9	Ih
561	2.06	41.2	30.9	Ih
116	0.00	60.5	0.00	TO
201	0.00	64.6	0.00	TO
225	0.00	61.8	0.00	TO
314	0.00	68.0	0.00	TO

same amount of computational work [53]. Taking that into account, we can observe in Figure 4.5a) the boost factor as a function of the size of the clusters for various temperatures and on Figure 4.5b) the same boost factor, but for different pressures of the metal gas.

It can be observed in Figure 4.5a) that, as it should be expected, the boost is largely increased for lower temperatures. This is mainly due to the fact that the high temperature of the simulation cannot be above the melting temperature of clusters, which is considerably lower than in the bulk. As can be seen in Figure 4.5b), the lower the flux, the higher the boost factor. This is mainly due to the fact that TAD keeps track of the energy basins the system has visited, and accelerate considerably the simulations using this knowledge (see Section 1.4), which the lower fluxes allow a larger amount of relaxation time. In both cases the boost factor decrease significantly for larger cluster sizes, which is due to

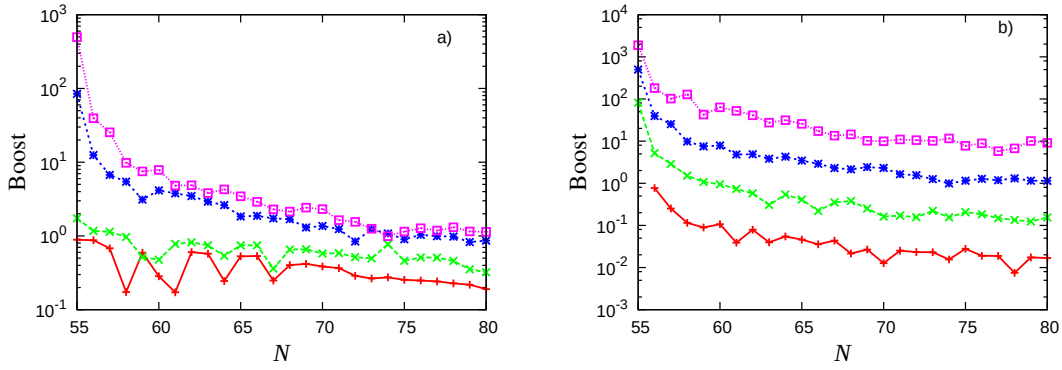

Figure 4.5: Boost of the TAD relaxation over MD as a function of the size of the cluster for a) from top to bottom temperatures of 50K, 100K, 150K, and 200K for a pressure of 0.1 atm. b) from top to bottom pressures of 0.01 atm, 0.1 atm, 1 atm, and 10 atm for a temperature of 50K.

a dependency of N^3 with system size dependency on TAD.

4.3.2 Common Neighbor Analysis index distribution

As previously stated, the CNA analysis is a good method to distinguish different cluster structures. Since a large number of samples have been simulated for various temperatures and pressures, one needs to use the CNA indexes to study the distribution of those structures. The best index to manage that is the P(5,5,5) index, since it shows the fivefold symmetry present in the cluster, where the icosahedral structures have a large number of fivefold, decahedral have usually very few, and FCC structures have no fivefold symmetry.

We have simulated the evolution of clusters from a 55 atoms cluster to a 80 atoms one, and averaged over 50 samples. The 55 Mackay icosahedron structure was used as the seed, since simulations where made for different values of pressure and temperature starting with a 7 atom cluster and the 55 icosahedral cluster was always reached. This is due to the fact that this structure is a very stable "magic" size. We will then present the distributions of P(5,5,5) on a cluster of 75 atoms for a growth at different temperatures and fluxes, as can be seen on Figure 4.6.

The influence of the temperature can be observed on the left plots of Figure 4.6, where at low temperatures the CNA index P(5,5,5) does not evince over the others, which means that no defined structure is found. However, at higher temperatures some structures prevail at some specific P(5,5,5) index values. In the case of the flux influence, similar behavior can be observed on the right plots of Figure 4.6, where at high fluxes no CNA index can also stand over the other values (no defined structure), however at lower fluxes some structures start to appear more frequently at specific P(5,5,5) index values.

It is also observed, that at these low temperatures, the stable "magic" size 75 decahedral (see table 4.1) structure is not the most common one. A variety of structures like Icosahedral, Decahedral, and FCC can be observed. To better identify these specific structures at their P(5,5,5) value, we present in Figure 4.7 all distribution functions independently of the values of pressure or temperature. Some peaks in the distribution function can be found, where above 0.05 ICO structures dominate (A), around 0.0125 the DECA is presented (B), and at 0 the FCC structure appears (C). Snapshots at these different peaks are presented on Figure 4.8.

4.3.3 Influence of deposited particles

In the literature, the 75 DECA is considered to growth through a shell of particles formed around the 55 structure [20]. Like in many cases, the formation of structures from previously stable ones, is mostly considered by being formed by the new deposited particles in the cluster. For that, it is necessary to understand the influence of particles deposited on top of the 55 ICO stable structure.

To study the effect of the new deposited particles for the ICO and DECA structures at the 75 atoms cluster, we use two different methods. First, we use the distribution of the distance of these deposited particles to the center of mass of the cluster, as can be seen in Figure 4.9a). And second, in Figure 4.9b) we plot the distribution of the angles formed between the position of the particles as a function of the center of mass of the cluster.

In both distribution functions, no particular peak is found. For the distance distribution, the average distance changes due to the difference in the form of the cluster between the ICO and DECA structures. However, no difference is found in the peaks of the distribution for the two structures. In the case of the angles distribution function, the same distribution of angles for the two structures is observed. This shows that the new particles do not have particular distribution for each structure, which reveals that the new particles do not form a shell around the 55 ICO, in contradiction with the literature [20]. This result shows that all particles have a role on the cluster restructuring and not only the new deposited ones in top of the 55 ICO structures.

4.3.4 Activation Barriers evolution

Since the deposition of new particles is not the main cause of structure formation, the energy surface is studied. This is a main advantage of using the TAD method, since during relaxation, it keeps track of all the activation barriers that the diffusive process has encountered.

Also in this case, the main structures of ICO and DECA were studied. In Figure 4.10a), the average activation energies encountered during relaxation as a function of the cluster size is presented. The maximum activation energies found on the diffusion of particles in the cluster as a function of its size is presented on Figure 4.10b).

These results show a higher activation barrier for the DECA formation, which can explain why this stable structure is mainly found at higher temperatures. It is observed that at a size of 75 particles, the activation barriers reverse their values, which reveals a large and stable basin around the 75 DECA structure, where transitions do not cross relatively high barriers.

4.4 Main Conclusions

We presented a model for the growth of free nanoclusters that set apart from the conventional models by properly computing the flux and the direction of particles velocity towards the cluster. We adapt the temperature accelerated dynamics technique to the relaxation of the cluster. The efficiency of the technique was demonstrated and simulations of cluster growth at experimental conditions of gas pressure were performed for the first time.

The main focus of our work was on small cluster sizes, specifically between 55 and 75 atoms. The effect of deposited particles on top of the stable 55 icosahedron was studied. It was shown that these deposited particles were not the only ones that have an effect on the cluster restructuring to a 75 decahedron.

Due to the capability of the TAD method of keeping track of all activation barriers of the transitions that took place, a size study of these barriers was performed. An evolution through higher barriers was found for the formation of the 75 decahedron, which can explain the necessity of higher temperatures to achieve this structure. The very low fluxes simulated were not low enough for those activation barriers to be overcome.

In the present work, we restrict our study to the growth of copper nanoclusters in the size range between 55 and 80 atoms. Despite the experimentally relevant fluxes values achieved in this work, there was difficulties on simulating at high temperatures. However, our technique can be easily applied to materials that growth nanoclusters at very low temperatures. The ability to keep track of all transitions overcome during diffusion, can deliver a useful way to list all mechanisms found, including concerted moves. This feature can lead to a future application of those mechanism to less computationally demanding methods like KMC.

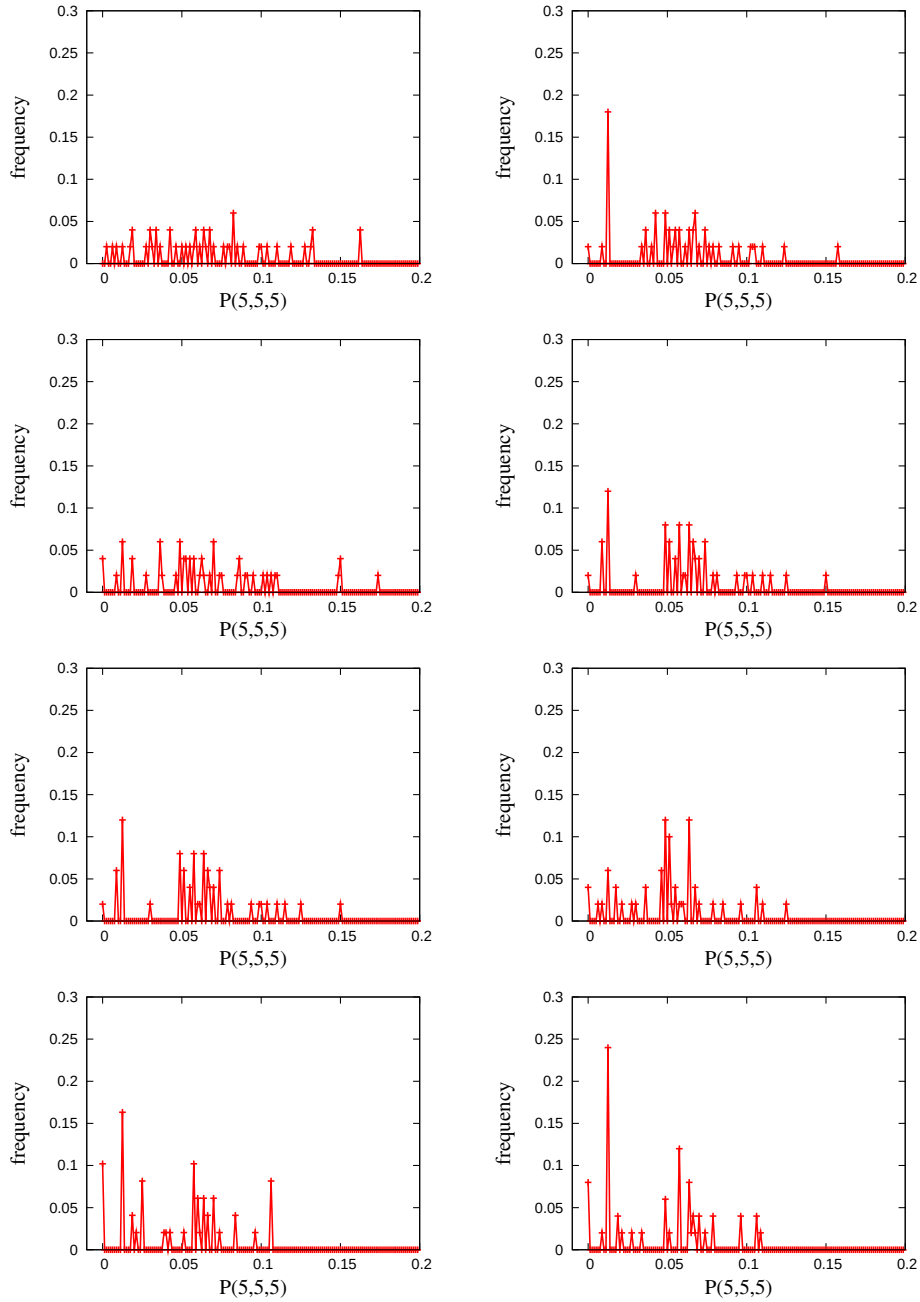

Figure 4.6: Distribution of the CNA index P(5,5,5) for a 75 atoms cluster at, left plots, a pressure of 1 atm and temperatures from top to bottom of 50, 100, 150, and 200 K. Right hand-side plots, a temperature of 150 K and pressures from top to bottom of 10, 1, 0.1, and 0.001 atm.

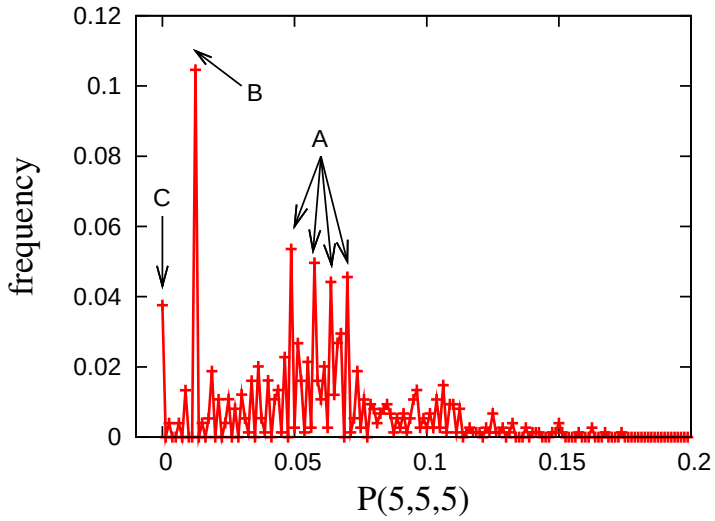

Figure 4.7: CNA P(5,5,5) index distribution for all samples, with different pressures and temperatures. A- ICO, B- DECA and C- FCC.

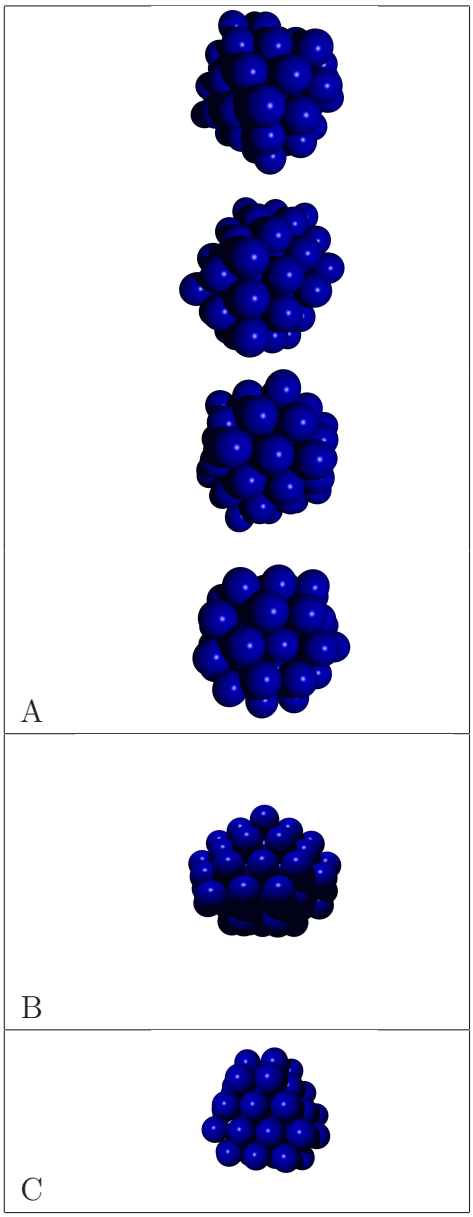

Figure 4.8: Most common structures of 75 atoms cluster for A-Icosahedral, B-Decahedral, and C-FCC.

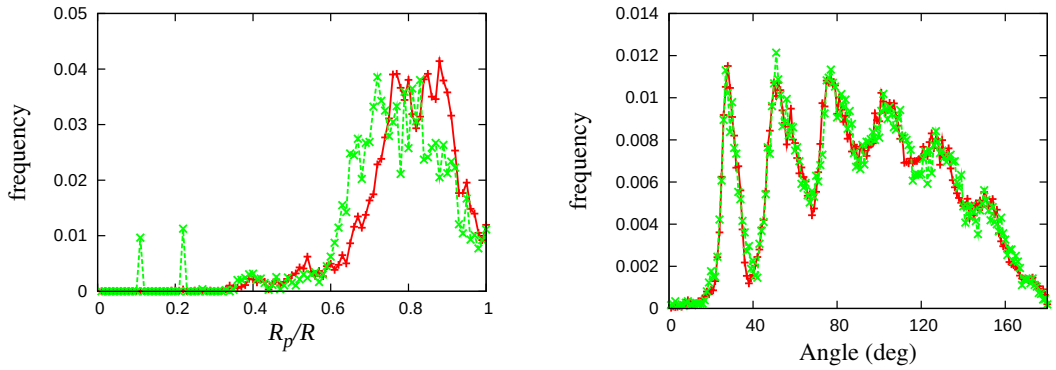

Figure 4.9: Distribution of a) distances of the new particles to the center of mass of the cluster and b) angle between the different particles for decahedral (red) and icosahedral (green) formation.

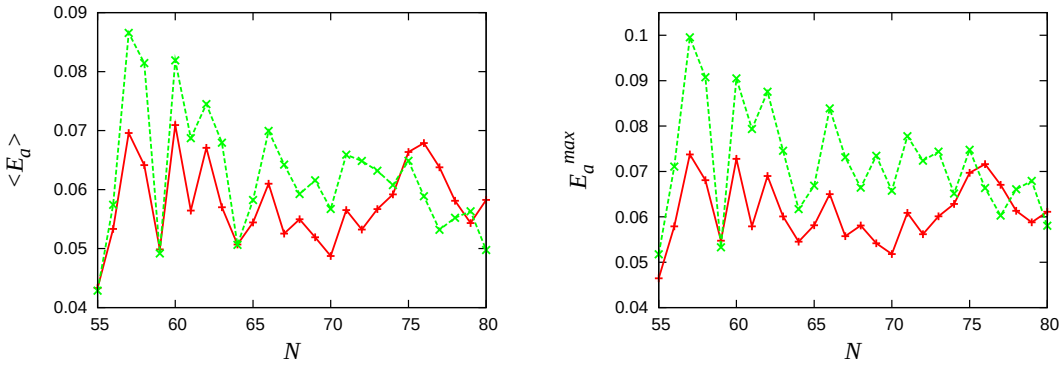

Figure 4.10: Distribution of a) average activation barrier found for each size and b) maximum activation barrier found for each size, for decahedral (red) and icosahedral (green) formation.

Final remarks

Throughout this thesis, several computational techniques have been employed. The computational methods varied accordingly to the specific characteristics of the system under study. In the first chapter, dedicated to the methods, each of the used computational technique is described and a justification for the use on specific systems is given.

The systems under study and the corresponding results have been divided into three chapters, depending on the main mechanisms and the type of substrate. On the first case, Chapter 2 was dedicated to reaction mechanisms on a crystalline substrate. Here, a model has been proposed for the ethanol electro-oxidation and another model for the oxidation of carbon monoxide, based on the Ziff, Gulari, and Barshad model [42]. In both models the effect of quenched impurities was considered. On Chapter 3, the mechanisms of deposition and particles diffusion on a crystalline substrate during thin-film growth was studied. In this case, a model has been developed, in 1+1D, that considers activation barriers depending on neighbors configurations. For the last physical system, on Chapter 4, the deposition on nanoclusters was simulated. A model taking into account the kinetic effects of deposition was used and simulations with temperature accelerated dynamics were performed.

For the ethanol electro-oxidation study, a model was created and solved analytically in 1D. Monte Carlo simulations in 1D validated the analytical results. A 2D study was also performed in both clean and impurities covered substrate. Particles percolation transitions were analyzed. For the clean substrate, it was proven that both transitions belong to the percolation universality class. On the substrate covered with impurities, it was shown

that monomers coverage is favored by these quenched impurities and both percolation thresholds are shifted.

Despite the simplicity of the proposed model, it is the first study to propose a generic model for the electo-oxidation of ethanol on a crystalline substrate where the cleavage mechanism has a key role. It can straightforwardly be applied to the electro-oxidation of other molecules, like other alcohols or even sugars, where a longer range cooperative behavior could be necessary.

On the carbon monoxide oxidation system, the phase transitions on the Ziff, Gulari, and Barshad model with impurities were studied. Emphasis was given to the monomer poisoning transition, since the nature of the transition changes with the increase of the coverage of impurities. This change was studied resorting to the fact that first-order transitions have short range correlation and second-order transitions are characterized by a diverging correlation length. With this knowledge, a point where the nature of the transition changes was pin down.

We have proposed a new method to classify the nature of an irreversible phase transition, which can be considered to other nonequilibrium systems with absorbing states. We have given explanations for the change in the nature and have computed more accurately the position of the change.

To study epitaxial growth, a (1+1)D kinetic Monte Carlo model was used, where the influence of the temperature and the flux was monitored. Different growth regimes where found, and a relation between the thermal and the kinetic roughening transitions was proposed. A phase diagram of the system was presented and the different transitions between regimes were studied in detail. The influence of the *corner rounding* process was also studied, and the Schwoebel barrier effect was shown to occur naturally in our model.

Here, a simple (1+1)D model has been used to explain some relevant phenomena on thin-film growth. A maximum on the roughness as a function of the mobility has been shown and the effect of the Schwoebel barrier has been explained at different parameters values. This model can be extended to (2+1)D, where other effects will emerge due to

the extra degrees of freedom, or also the introduction of a different interaction with the substrate may be of interest.

The last physical system of free nanocluster growth was studied using the technique of regular molecular dynamics for the deposition and temperature accelerated dynamics for the relaxation of the cluster. It was shown a boost on computational efficiency with the use of TAD, mainly at low temperatures and fluxes. The effect of deposited atoms on a 55 atoms icosahedral clusters was studied, where it was shown that the newly deposited particles do not form a shell around the stable 55 atoms cluster as previously thought. The ability to study the evolution of the system activation barrier was presented, where their influence on the formation of the final structure was shown.

Despite the limitations of the technique to simulate large systems, the analysis could be performed for even lower fluxes and temperatures. This method could also be of interest by keeping track of all transitions occurring during the cluster relaxation. This can give researchers a list of common mechanisms during growth, that could be used in more efficient techniques like kinetic Monte Carlo.

In this thesis, we have studied the effects of deposition on crystalline and amorphous substrates, and studied the mechanisms that follow it. Several computational techniques were used for these studies. It was shown that each technique has a different applications, depending on the study at hands.

Bibliography

[1] N. Bernstein, "Atomistic Simulations of Fracture in Semiconductors," in *Handbook of Materials Modeling* (S. Yip, ed.), p. 855, Dordrecht: Springer, 2005.

[2] C. G. Van de Walle, "Defects and Impurities in Semiconductors," in *Handbook of Materials Modeling* (S. Yip, ed.), p. 1877, Dordrecht: Springer, 2005.

[3] W. Szymczyk, "Numerical simulation of composite surface coating as a functionally graded material," *Mater. Sci. Eng. A*, vol. 412, p. 61, 2005.

[4] L. A. Dobrzański, A. Śliwa, and W. Kwaśny, "The computer simulation of stresses in the Ti+ Ti (C x N) coatings obtained in the PVD process," *J. Achiev. Mater. Manu. Eng.*, vol. 24, p. 155, 2007.

[5] T. R. Powers, "Mechanics of Lipid Bilayer Membranes," in *Handbook of Materials Modeling* (S. Yip, ed.), p. 2631, Dordrecht: Springer, 2005.

[6] E. Tajkhorshid, F. Zhu, and K. Schulten, "Kinetic theory and simulation of single-channel water transport," in *Handbook of Materials Modeling* (S. Yip, ed.), p. 1797, Dordrecht: Springer, 2005.

[7] F. Zaera, "The Surface Chemistry of Heterogeneous Catalysis: Mechanisms, Selectivity, and Active Sites," *Chem. Rec.*, vol. 5, p. 133, 2005.

[8] F. Zaera, "The surface chemistry of catalysis: new challenges ahead," *Surface Science*, vol. 500, pp. 947–965, 2002.

[9] A. T. Bell, "The Impact of Nanoscience on Heterogeneous Catalysis," *Science*, vol. 299, p. 1688, 2003.

[10] N. D. Spencer and G. A. Somorjai, "Catalysis," *Rep. Prog. Phys.*, vol. 46, p. 1, 1983.

[11] V. Privman, *Nonequilibrium Statistical Mechanics in One Dimension*. Cambridge: Cambridge University Press, 2005.

[12] M. L. Cohen, "Concepts for Modeling Electrons in Solids: A Perspective," in *Handbook of Materials Modeling* (S. Yip, ed.), p. 13, Dordrecht: Springer, 2005.

[13] D. P. Landau and K. Binder, *A guide to Monte Carlo simulations in statistical physics*. Cambridge: Cambridge University Press, 2005.

[14] D. Rapaport, *The art of molecular dynamics simulation*. Cambridge: Cambridge University Press, 2 ed., 2004.

[15] R. Car and M. Parrinello, "Unified approach for molecular dynamics and density-functional theory," *Phys. Rev. Lett.*, vol. 55, p. 2471, 1985.

[16] W. P. McCray, "MBE deserves a place in the history books.," *Nature nanotechnology*, vol. 2, no. 5, pp. 259–61, 2007.

[17] D. J. Wales, *Energy Landscapes With Applications to Clusters, Biomolecules and Glasses*. Cambridge: Cambridge University Press, 2003.

[18] P. Jensen, "Growth of nanostructures by cluster deposition: Experiments and simple models," *Rev. Mod. Phys*, vol. 71, p. 1695, 1999.

[19] R. Ferrando, J. Jellinek, and R. L. Johnston, "Nanoalloys: from theory to applications of alloy clusters and nanoparticles.," *Chem. Rev.*, vol. 108, p. 845, 2008.

[20] F. Baletto and R. Ferrando, "Structural properties of nanoclusters: Energetic, thermodynamic, and kinetic effects," *Rev. Mod. Phys.*, vol. 77, p. 371, 2005.

[21] C. Binns, "Nanoclusters deposited on surfaces," *Surf. Sci. Rep.*, vol. 44, p. 1, 2001.

[22] A. T. Bell, "The Impact of Nanoscience on Heterogeneous Catalysis," *Science*, vol. 299, p. 1688, 2003.

[23] H. F. Wang and Z. P. Liu, "Comprehensive mechanism and structure-sensitivity of ethanol oxidation on platinum: new transition-state searching method for resolving the complex reaction network," *J. Am. Chem. Soc.*, vol. 130, p. 10996, 2008.

[24] H.-F. Wang and Z.-P. Liu, "Selectivity of Direct Ethanol Fuel Cell Dictated by a Unique Partial Oxidation Channel," *J. Phys. Chem. C*, vol. 111, p. 12157, 2007.

[25] M. P. Allen and D. J. Tildesley, *Computer simulation of liquids*. Oxford: Oxford University Press, 1 ed., 1990.

[26] S. Das Sarma, C. J. Lanczycki, R. Kotlyar, and S. V. Ghaisas, "Scale invariance and dynamical correlations in growth models of molecular beam epitaxy," *Phys. Rev. E*, vol. 53, p. 359, 1996.

[27] W. L. Cavalcanti, W. Figueiredo, and M. Santos, "Growth model on (1 + 1) dimensions with local relaxation and discrete number of orientations," *Phys. Stat. Sol. (a)*, vol. 201, p. 894, 2004.

[28] R. Phillips and D. C. Chrzan, "Kinetic Phase Diagram for Crystal Growth: A (1+1)-Dimensional Model," *Phys. Rev. Lett.*, vol. 67, p. 220, 1991.

[29] T. Kaneko, P. Šmilauer, B. A. Joyce, T. Kawamura, and D. D. Vvedensky, "Reentrant layer-by-layer etching of GaAs(001)," *Phys. Rev. Lett.*, vol. 74, p. 3289, 1995.

[30] M. F. Gyure, J. J. Zinck, C. Ratsch, and D. D. Vvedensky, "Unstable growth on rough surfaces," *Phys. Rev. Lett.*, vol. 81, p. 4931, 1998.

[31] S. Das Sarma and P. I. Tamborenea, "A new universality class for kinetic growth: One-dimensional molecular-beam epitaxy," *Phys. Rev. Lett.*, vol. 66, p. 325, 1991.

[32] Z.-L. Liu, L. Yu, K.-L. Yao, X.-B. Jing, X.-A. Li, and X.-Z. Sun, "Kinetic Monte Carlo simulation of deposition of energetic copper atoms on a Cu(001) substrate," *J. Phys. D: Appl. Phys.*, vol. 38, p. 4202, 2005.

[33] L. Wang and P. Clancy, "Kinetic Monte Carlo simulation of the growth of polycrystalline Cu films," *Surf. Sci.*, vol. 473, p. 25, 2001.

[34] R. Ferrando and G. Treglia, "High-Temperature Study of the Schwoebel Effect in Au (111)," *Phys. Rev. Lett.*, vol. 76, p. 2109, 1996.

[35] S. Das Sarma, S. M. Paik, K. E. Khor, and A. Kobayashi, "Atomistic numerical simulation of epitaxial crystal growth," *J. Vac. Sci. Technol. B*, vol. 5, p. 1179, 1987.

[36] J. Doye and D. Wales, "Thermodynamics of Global Optimization," *Phy. Rev. Lett.*, vol. 80, p. 1357, 1998.

[37] V. G. Grigoryan, D. Alamanova, and M. Springborg, "Structure and energetics of nickel, copper, and gold clusters," *Eur. Phys. J. D*, vol. 34, p. 187, 2005.

[38] J. Uppenbrink and D. J. Wales, "Structure and energetics of model metal clusters," *J. Chem. Phys.*, vol. 96, p. 8520, 1992.

[39] D. Alamanova, V. Grigoryan, and M. Springborg, "Theoretical Study of the Structure and Energetics of Silver Clusters," *Journal of Physical Chemistry C*, vol. 111, no. 34, pp. 12577–12587, 2007.

[40] L. R. Lynd, "Overview and evaluation of fuel ethanol from cellulosic biomass: technology, economics, the environment, and policy," *Annu. Rev. Energy Environ.*, vol. 21, p. 403, 1996.

[41] J. W. Evans, "Random and cooperative sequential adsorption," *Rev. Mod. Phys.*, vol. 65, p. 1281, 1993.

[42] R. M. Ziff, E. Gulari, and Y. Barshad, "Kinetic phase transitions in an irreversible surface-reaction model," *Phys. Rev. Lett.*, vol. 56, p. 2553, 1986.

[43] I. Jensen and H. Fogedby, "Kinetic phase transitions in a surface-reaction model with diffusion: Computer simulations and mean-field theory," *Phys. Rev. A*, vol. 42, no. 4, p. 1969, 1990.

[44] J. W. Evans, "ZGB surface reaction model with high diffusion rates," *J. Chem. Phys.*, vol. 98, p. 2463, 1993.

[45] S. Pezzagna, S. Vézian, J. Brault, and J. Massies, "Layer-by-layer epitaxial growth of Mg on GaN(0001)," *Appl. Phys. Lett.*, vol. 92, p. 233111, 2008.

[46] M. Meixner, R. Kunert, and E. Schöll, "Control of strain-mediated growth kinetics of self-assembled semiconductor quantum dots," *Phys. Rev. B*, vol. 67, p. 24, 2003.

[47] A.-L. Barabási and H. E. Stanley, *Fractal Concepts in Surface Growth*. Cambridge: Cambridge University Press, 1995.

[48] J. Krug, M. Plischke, and M. Siegert, "Surface diffusion currents and the universality classes of growth," *Phys. Rev. Lett.*, vol. 70, p. 3271, 1993.

[49] P. P. Chatraphorn and S. Das Sarma, "Layer-by-layer epitaxy in limited mobility nonequilibrium models of surface growth," *Phys. Rev. E*, vol. 66, p. 041601, 2002.

[50] P. Smilauer, M. R. Wilby, and D. D. Vvedensky, "Reentrant layer-by-layer growth: A numerical study," *Phys. Rev. B*, vol. 47, p. 4119, 1993.

[51] M. Schimschak and J. Krug, "Bulk defects and surface roughening in epitaxial growth," *Phys. Rev. B*, vol. 52, p. 8550, 1995.

[52] B. Meng and W. H. Weinberg, "Dynamical Monte Carlo studies of molecular beam epitaxial growth models: interfacial scaling and morphology," *Surf. Sci.*, vol. 364, p. 151, 1996.

[53] M. R. Sø rensen and A. F. Voter, "Temperature-accelerated dynamics for simulation of infrequent events," *J. Chem. Phys.*, vol. 112, p. 9599, 2000.

[54] B. P. Uberuaga, F. Montalenti, T. C. Germann, and A. F. Voter, "Accelerated molecular dynamics methods," in *Handbook of Materials Modeling* (S. Yip, ed.), p. 629, Dordrecht: Springer, 2005.

[55] S. Yip, *Handbook of materials modeling*. Dordrecht: Springer, 2005.

[56] M. C. Payne, M. P. Teter, D. C. Allan, T. A. Arias, and J. D. Joannopoulos, "Iterative minimization techniques for *ab initio* total-energy calculations - Molecular-Dyanmics and conjugate gradients," *Rev. Mod. Phys.*, vol. 64, p. 1045, 1992.

[57] K. Binder, "Applications of Monte Carlo methods to statistical physics," *Rep. Prog. Phys.*, vol. 60, p. 487, 1997.

[58] J. Peiró and S. Sherwin, "Finite Difference, Finite Element and Finite Volume methods for partial differential equations," in *Handbook of Materials Modeling* (S. Yip, ed.), p. 2415, Dordrecht: Springer, 2005.

[59] T. Y. Hou, "Multiscale Computation of Fluid Flow in Heterogeneous Media," in *Handbook of Materials Modeling* (S. Yip, ed.), p. 1507, Dordrecht: Springer, 2005.

[60] R. E. Rudd, "Concurrent Multiscale Simulation at Finite Temperature: Coarse-Grained Molecular Dynamics," in *Handbook of Materials Modeling* (S. Yip, ed.), p. 649, Dordrecht: Springer, 2005.

[61] E. Weinan and X. Li, "Multiscale Modeling of Crystalline Solids," in *Handbook of Materials Modeling* (S. Yip, ed.), p. 1491, Dordrecht: Springer, 2005.

[62] G. Gilmer and S. Yip, "Basic Monte Carlo Models: Equilibrium and Kinetics," in *Handbook of Materials Modeling* (S. Yip, ed.), p. 613, Dordrecht: Springer, 2005.

[63] V. G. Mavrantzas, "Monte Carlo simulation of chain molecules," in *Handbook of Materials Modeling* (S. Yip, ed.), p. 2583, Dordrecht: Springer, 2005.

[64] E. V. Albano and J. Marro, "Monte Carlo study of the CO-poisoning dynamics in a model for the catalytic oxidation of CO," *J. Chem. Phys.*, vol. 113, p. 10279, 2000.

[65] E. V. Albano and R. A. Monetti, "Numerical Study of the First Order Irreversible Phase Transition in the Ziff-Gulari-Barshad Model," *Surf. Rev. Lett.*, vol. 10, p. 867, 2003.

[66] J. Marro and R. Dickman, *Nonequilibrium phase transitions in lattice models*. Cambridge: Cambridge University Press, 1999.

[67] A.-L. Barabási, *Linked: The New Science of Networks*. Cambridge: Perseus Books Group, 2002.

[68] H. Solomon, *Geometric probability*. Philadelphia: SIAM, 1978.

[69] W. Krauth, *Statistical Mechanics: Algorithms and Computations*. Oxford: Oxford University Press, 2006.

[70] N. Metropolis and S. Ulam, "The monte carlo method," *J. Amer. Stat. Ass.*, vol. 44, p. 335, 1949.

[71] N. Metropolis, "The beginning of the Monte Carlo method," *Los Alamos Science*, vol. 15, no. 7, p. 125, 1987.

[72] N. Metropolis, A. W. Rosenbluth, M. N. Rosenbluth, A. H. Teller, E. Teller, and Others, "Equation of state calculations by fast computing machines," *j. chem. phys.*, vol. 21, p. 1087, 1953.

[73] J. M. Ortiz de Zárate, "Interview with Michael E. Fisher," *Europhys. News*, vol. 42, p. 14, 2011.

[74] M. W. Zemansky and R. H. Dittman, *Heat and Thermodynamics*. Singapore: McGraw-Hill, 7 ed., 1997.

[75] F. Reif, *Fundamentals of statistical and thermal physics*. Auckland: McGraw-Hill, 1985.

[76] H. Gould and J. Tobochnik, *Statistical and Thermal Physics: With Computer Applications*. Princeton: Princeton University Press, 2010.

[77] N. G. V. Kampen, *Stochastic processes in physics and chemistry*. Amsterdam: North-Holland, 1992.

[78] L. E. Reichl, *A modern course in statistical physics*. New York: John Wiley & Sons, 3 ed., 2009.

[79] M. E. J. Newman and G. T. Barkema, *Monte Carlo methods in statistical physics*. Oxford: Clarendon Press, 1999.

[80] S. G. Brush, "History of the Lenz-Ising model," *Rev. Mod. Phys.*, vol. 39, p. 883, 1967.

[81] F. Wu, "The potts model," *Rev. Mod. Phys.*, vol. 54, p. 235, 1982.

[82] L. P. Kadanoff, "More is the Same; Phase Transitions and Mean Field Theories," *J. Stat. Phys.*, vol. 137, p. 777, 2009.

[83] L. P. Kadanoff, "Phases of Matter and Phase Transitions; From Mean Field Theory to Critical Phenomena," *J. Phys.: Cond. Matt.*, vol. 12, p. 1496, 2009.

[84] N. Araújo, *Nonequilibrium thin-film growth: kinetics of deposition and post evolution relaxation*. Germany: Lambert Academic Publishing, 2010.

[85] G. Ódor, *Universality in nonequilibrium lattice systems*. Singapore: World Scientific, 2008.

[86] Z. Rácz, "Nonequilibrium phase transitions," in *Notes to lectures delivered in Les Houches (Summer school, July 2002)*, 2002.

[87] J. R. Dorfman, *An introduction to chaos in nonequilibrium statistical mechanics.* Cambridge: Cambridge Univ Pr, 1999.

[88] S. Katz, J. L. Lebowitz, and H. Spohn, "Nonequilibrium Steady States of Stochastic Lattice Gas Models of Fast Ionic Conductors," *J. Stat. Phys.*, vol. 34, p. 497, 1984.

[89] A. A. Ovchinnikov and Y. B. Zeldovich, "Role of density fluctuations in bimolecular reaction kinetics," *Chem. Phys.*, vol. 28, p. 215, 1978.

[90] A. B. Bortz, M. H. Kalos, and J. L. Lebowitz, "A new algorithm for Monte Carlo simulation of Ising spin systems," *J. Comp. Phys.*, vol. 17, p. 10, 1975.

[91] P. Hänggi, P. Talkner, and M. Borkovec, "Reaction-rate theory: fifty years after Kramers," *Rev. Mod. Phys.*, vol. 62, p. 251, 1990.

[92] K. J. Laidler and M. C. King, "Development of transition-state theory," *J. Chem. Phys.*, vol. 87, p. 2657, 1983.

[93] A. F. Voter, "Introduction to the kinetic Monte Carlo method," in *Radiation Effects in Solids* (K. E. Sickafus, E. Kotomin, and B. P. Uberuaga, eds.), p. 1, Dordrecht: Springer, 2007.

[94] T. Pang, *An introduction to computational physics.* Cambridge: Cambridge University Press, 2 ed., 2006.

[95] A. Rahman, "Correlation of motion of atoms in liquid argon," *Phys. Rev. E*, vol. 136A, p. 405, 1964.

[96] A. F. Voter, "The Embedded Atom Method," in *Intermetallic Compounds: Principles and Practice* (J. H. Westbrook and R. L. Fleischer, eds.), p. 77, john wiley ed., 1994.

[97] A. F. Voter, "Parallel replica method for dynamics of infrequent events," *Phys. Rev. B*, vol. 57, p. 985, 1998.

[98] G. Henkelman and H. Jónsson, "Long time scale kinetic Monte Carlo simulations without lattice approximation and predefined event table," *J. Chem. Phys.*, vol. 115, p. 9657, 2001.

[99] D. T. Gillespie, "A general method for numerically simulating the stochastic time evolution of coupled chemical reactions," *J. comp. phys.*, vol. 22, p. 403, 1976.

[100] G. Henkelman and H. Jónsson, "Improved tangent estimate in the nudged elastic band method for finding minimum energy paths and saddle points," *J. Chem. Phys.*, vol. 113, p. 9978, 2000.

[101] F. Montalenti and A. F. Voter, "Exploiting past visits or minimum-barrier knowledge to gain further boost in the temperature-accelerated dynamics method," *J. Chem. Phys.*, vol. 116, p. 4819, 2002.

[102] A. F. Voter, "A method for accelerating the molecular dynamics simulation of infrequent events," *J. Chem. Phys.*, vol. 106, p. 4665, 1997.

[103] R. A. Miron and K. A. Fichthorn, "Multiple-Time Scale Accelerated Molecular Dynamics: Addressing the Small-Barrier Problem," *Phys. Rev. Lett.*, vol. 93, p. 128301, 2004.

[104] A. F. Voter, F. Montalenti, and T. C. Germann, "Extending the Time Scale in Atomistic Simulations of Materials," *Annu. Rev. Mater. Res.*, vol. 32, p. 321, 2002.

[105] A. Cadilhe, N. A. M. Araújo, and V. Privman, "Random sequential adsorption: from continuum to lattice and pre-patterned substrates," *J. Phys.: Condens. Matter*, vol. 19, p. 065124, 2007.

[106] N. A. M. Araújo and A. Cadilhe, "Gap-Size Distribution Functions of a Random Sequential Adsorption Model of Segments on the Line," *Phys. Rev. E*, vol. 73, p. 051602, 2006.

[107] N. A. M. Araújo and A. Cadilhe, "Jammed state characterization of the random sequential adsorption of segments of two lengths on a line," *J. Stat. Mech.*, vol. 2010, p. 9, 2010.

[108] B. Bonnier, "Random sequential adsorption of binary mixtures on a line," *Phys. Rev. E*, vol. 64, p. 066111, 2001.

[109] B. Bonnier, M. Hontebeyrie, Y. Leroyer, C. Meyers, and E. Pommiers, "Adsorption of line segments on a square lattice," *Phys. Rev. E*, vol. 49, p. 305, 1994.

[110] V. Privman, "Dynamics of nonequilibrium processes: Surface adsorption, reaction−diffusion kinetics, ordering and phase separation," *Trends Stat. Phys.*, vol. 1, p. 89, 1994.

[111] B. J. Brosilow, R. M. Ziff, and R. D. Vigil, "Random sequential adsorption of parallel squares," *Phys. Rev. A*, vol. 43, p. 631, 1991.

[112] J. Feder, "Random sequential adsorption," *J. Theor. Biol.*, vol. 87, p. 237, 1980.

[113] V. Privman, J.-S. Wang, and P. Nielaba, "Continuum limit in random sequential adsorption," *Phys. Rev. B*, vol. 43, p. 3366, 1991.

[114] M. C. Bartelt and V. Privman, "Kinetics of irreversible monolayer and multilayer adsorption," *Int. J. Mod. Phys. B*, vol. 5, p. 2883, 1991.

[115] J. W. Evans, "Exactly solvable irreversible processes on Bethe lattices," *J. Math. Phys.*, vol. 25, p. 2527, 1984.

[116] R. Dickman and J. S. Wang, "Random sequential adsorption: Series and virial expansions," *J. Chem. Phys.*, vol. 94, p. 8252, 1991.

[117] H. Wang, Z. Jusys, and R. J. Behm, "Ethanol Electrooxidation on a Carbon-Supported Pt Catalyst: Reaction Kinetics and Product Yields," *J. Phys. Chem. B*, vol. 108, p. 19413, 2004.

[118] J. W. Evans and R. S. Nord, "Competitive irreversible random one-, two-, three-,... point adsorption on two-dimensional lattices," *Phys. Rev. B*, vol. 31, p. 1759, 1985.

[119] R. H. López, F. Romá, V. Gargiulo, J. L. Sales, and G. Zgrablich, "Enantioselectivity in random deposition processes on template surfaces.," *J. Phys. Chem. B*, vol. 112, p. 8619, 2008.

[120] J. J. González, P. C. Hemmer, and J. S. Hø ye, "Cooperative effects in random sequential polymer reactions," *Chem. Phys.*, vol. 3, p. 228, 1974.

[121] P. J. Flory, "Intramolecular Reaction between Neighboring Substituents of Vinyl Polymers," *J. Am. Chem. Soc*, vol. 61, p. 1518, 1939.

[122] L. Finegold and J. T. Donnell, "Maximum density of random placing of membrane particles," *Nature*, vol. 278, p. 443, 1979.

[123] A. S. McLeod and L. F. Gladden, "The influence of the random sequential adsorption of binary mixtures on the kinetics of hydrocarbon hydrogenation reactions," *J. Chem. Phys.*, vol. 110, p. 4000, 1999.

[124] J. Feder and I. Giaever, "Adsorption of ferritin," *J. Colloid Interf. Sci.*, vol. 78, p. 144, 1980.

[125] G. Y. Onoda and E. G. Liniger, "Experimental determination of the random-parking limit in two dimensions," *Phys. Rev. A*, vol. 33, p. 715, 1986.

[126] P. Parpot, N. Nunes, and A. P. Bettencourt, "Electrocatalytic oxidation of monosaccharides on gold electrode in alkaline medium: Structure-reactivity relationship," *J. Electroanal. Chem.*, vol. 596, p. 65, 2006.

[127] A. J. Ramirez-Pastor, J. L. Riccardo, and V. Pereyra, "Adsorption of linear k-mers on heterogeneous surfaces with simple topographies," *Langmuir*, vol. 16, p. 682, 2000.

[128] C. Zuppa, M. Ciacera, and G. Zgrablich, "Cooperative Sequential Adsorption of k-mers on Heterogeneous Substrates," *Langmuir*, vol. 15, p. 5984, 1999.

[129] J. L. Riccardo, M. A. Chade, V. D. Pereyra, and G. Zgrablich, "Adsorption and surface diffusion on generalized heterogeneous surfaces," *Langmuir*, vol. 8, p. 1518, 1992.

[130] D. J. Stacchiola, M. Ciacera, C. Zuppa, T. P. Eggarter, and G. Zgrablich, "Cooperative sequential adsorption processes on heterogeneous substrates," *J. Chem. Phys.*, vol. 108, p. 1730, 1998.

[131] J. L. Sales and G. Zgrablich, "Thermal desorption of interacting molecules from heterogeneous surfaces," *Phys. Rev. B*, vol. 35, p. 9520, 1987.

[132] G. Kondrat, "The effect of impurities on jamming in random sequential adsorption of elongated objects.," *J. Chem. Phys.*, vol. 124, p. 054713, 2006.

[133] J. W. Lee, "Kinetics of random sequential adsorption on disordered substrates," *J. Phys. A: Math. Gen.*, vol. 29, p. 33, 1996.

[134] E. Ben-Naim and P. L. Krapivsky, "On irreversible deposition on disordered substrates," *J. Phys. A: Math. Gen.*, vol. 27, p. 3575, 1994.

[135] N. A. M. Araújo, A. Cadilhe, and V. Privman, "Morphology of fine-particle monolayers deposited on nanopatterned substrates," *Phys. Rev. E*, vol. 77, p. 031603, 2008.

[136] M. J. S. Farias, G. A. Camara, and A. A. Tanaka, "Electrooxidation of isotope-labeled ethanol: a FTIRS study," *J. Solid State Electrochem.*, vol. 11, p. 1465, 2007.

[137] E. V. Albano, "Finite-size effects in kinetic phase transitions of a model reaction on a fractal surface: Scaling approach and Monte Carlo investigation," *Phys. Rev. B*, vol. 42, p. 10818, 1990.

[138] J. P. Hovi, J. Vaari, H. P. Kaukonen, and R. M. Nieminen, "Simulations of the effect of preadsorbed poisons and promoters on irreversible surface reactions," *Comp. Mat. Sci.*, vol. 1, p. 33, 1992.

[139] G. L. Hoenicke and W. Figueiredo, "Ziff-Gulari-Barshad model with random distribution of inert sites," *Phys. Rev. E*, vol. 62, p. 6216, 2000.

[140] C. D. Lorenz, R. Haghgooie, C. Kennebrew, and R. M. Ziff, "The effects of surface defects in a catalysis model," *Surf. Sci.*, vol. 517, p. 75, 2002.

[141] D.-y. Hua and Y.-q. Ma, "Hysteresis phenomena in CO catalytic oxidation system in the presence of inhomogeneities of the catalyst surface," *Phys. Rev. E*, vol. 66, p. 066103, 2002.

[142] L. A. Abramova, S. P. Baranov, and A. A. Dulov, "A Model for the CO Oxidation Reaction over a Catalyst Surface with Microscopic Nonuniformities," *Kinet. Catal.*, vol. 44, p. 862, 2003.

[143] A. P. J. Jansen and J. J. Lukkien, "Dynamic Monte-Carlo simulations of reactions in heterogeneous catalysis," *Catal. Today*, vol. 53, p. 259, 1999.

[144] V. Bustos, R. O. Unac, and G. Zgrablich, "Kinetic phase transitions in a contaminated monomer-dimer reaction model," *Phys. Rev. E*, vol. 62, p. 8768, 2000.

[145] D. H. Schmidt and M. Santos, "Dimer production in a poisoned catalytic model," *Phys. Stat. Sol. (a)*, vol. 187, p. 305, 2001.

[146] J. W. Evans, "Random and cooperative sequential adsorption: exactly solvable models on ID lattices, continuum limits, and 2D extensions," in *Nonequilibrium Statisti-*

cal Mechanics in One Dimension (V. Privman, ed.), Cambridge: Cambridge Univ. Pr., 1997.

[147] K. J. Vette, T. W. Orent, D. K. Hoffman, and R. S. Hansen, "Kinetic model for dissociative adsorption of a diatomic gas," *J. Chem. Phys.*, vol. 60, p. 4854, 1974.

[148] F. Rampf and E. V. Albano, "Interplay between jamming and percolation upon random sequential adsorption of competing dimers and monomers," *Phys. Rev. E*, vol. 66, p. 61106, 2002.

[149] J. Hoshen and R. Kopelman, "Percolation and cluster distribution. I. Culster multiple labeling technique and critical concentration algorithm," *Phys. Rev. B*, vol. 14, p. 3438, 1976.

[150] D. Stauffer and A. Aharony, *Introduction to percolation theory.* London: Taylor & Francis, 1994.

[151] G. Ódor, "Universality classes in nonequilibrium lattice systems," *Rev. Mod. Phys*, vol. 76, p. 663, 2004.

[152] H. Hinrichsen, "Non-equilibrium critical phenomena and phase transitions into absorbing states," *Adv. Phys*, vol. 49, p. 815, 2000.

[153] M. Henkel, H. Hinrichsen, and S. Lübeck, *Non-Equilibrium Phase Transitions. Volume 1: Absorbing Phase Transitions.* Dordrecht: Springer, 2008.

[154] D.-y. Hua and Y.-q. Ma, "Monomer-dimer reaction model with asymmetric adsorption of monomer and dimer on the catalyst surface," *Phys. Rev. E*, vol. 64, p. 056102, 2001.

[155] R. Dickman, "Kinetic phase transitions in a surface-reaction model: mean-field theory," *Phys. Rev. A*, vol. 34, p. 4246, 1986.

[156] J. W. Evans and M. S. Miesch, "Characterizing kinetics near a first-order catalytic-poisoning transition," *Phys. Rev. Lett.*, vol. 66, p. 833, 1991.

[157] J. W. Evans and M. S. Miesch, "Catalytic reaction kinetics near a first-order poisoning transition," *Surf. Sci.*, vol. 245, no. 3, p. 401, 1991.

[158] R. M. Ziff and B. J. Brosilow, "Investigation of the first-order phase transition in the $A - B_2$ reaction model using a constant-coverage kinetic ensemble," *Phys. Rev. A*, vol. 46, p. 4630, 1992.

[159] E. Loscar and E. V. Albano, "Critical behaviour of irreversible reactions," *Rep. Prog. Phys.*, vol. 66, p. 1343, 2003.

[160] M. Kolb and Y. Boudeville, "Kinetic model for heterogeneous catalysis: Cluster and percolation properties," *J. Chem. Phys.*, vol. 92, p. 3935, 1990.

[161] R.-F. Xiao and N.-B. Ming, "Surface roughening and surface diffusion in kinetic thin-film deposition," *Phys. Rev. E*, vol. 49, p. 4720, 1994.

[162] P. A. Thiel and J. W. Evans, "Energetic parameters for atomic-scale processes on Ag(100)," *J. Phys. Chem. B*, vol. 108, p. 14428, 2004.

[163] G. Rosenfeld, B. Poelsema, and G. Comsa, "The concept of two mobilities in homoepitaxial growth," *J. Cryst. Growth*, vol. 151, p. 230, 1995.

[164] G. Rosenfeld, N. N. Lipkin, W. Wulfhekel, J. Kliewer, K. Morgenstern, B. Poelsema, and G. Comsa, "New concepts for controlled homoepitaxy," *Appl. Phys. A*, vol. 61, p. 455, 1995.

[165] J. W. Evans, P. A. Thiel, and M. C. Bartelt, "Morphological evolution during epitaxial thin film growth: Formation of 2D islands and 3D mounds," *Surf. Sci. Rep.*, vol. 61, p. 1, 2006.

[166] T. Michely and J. Krug, *Islands, mounds, and atoms*. Berlin: Springer, 2004.

[167] A. Pimpinelli and J. Villain, *Physics of crystal growth.* Cambridge: Cambridge Univ Pr, 1998.

[168] J. Lapujoulade, "The roughening of metal surfaces," *Surf. Sci. Rep.*, vol. 20, p. 191, 1994.

[169] D. D. Vvedensky, "Epitaxial phenomena across length and time scales," *Surf. Interface Anal.*, vol. 31, p. 627, 2001.

[170] S. Das Sarma, "Numerical studies of epitaxial kinetics: What can computer simulation tell us about nonequilibrium crystal growth?," *J. Vac. Sci. Technol. A*, vol. 8, p. 2714, 1990.

[171] S. Clarke and D. D. Vvedensky, "Origin of Reflection High-Energy Electron-Diffraction Intensity Oscillations during Molecular-Beam Epitaxy: A Computational Modeling Approach," *Phys. Rev. Lett.*, vol. 58, p. 2235, 1987.

[172] A. Rockett, "Monte Carlo simulations of the growth of diamond-structure semiconductors and surface-reflected electron-beam intensities during molecular-beam epitaxy," *J. Vac. Sci. Technol. B*, vol. 6, p. 763, 1988.

[173] A. Kobayashi and S. Das Sarma, "Epitaxial growth of Ge_xSi_{1-x} on Si: A direct Monte Carlo simulation," *Phys. Rev. B*, vol. 37, p. 1039, 1988.

[174] T. Kawamura, A. Kobayashi, and S. Das Sarma, "Stochastic simulation of molecular-beam epitaxial growth of a model compound semiconductor: Effects of kinetics," *Phys. Rev. B*, vol. 39, p. 12723, 1989.

[175] C. R. Stoldt, C. J. Jenks, P. A. Thiel, A. M. Cadilhe, and J. W. Evans, "Smoluchowski ripening of Ag islands on Ag(100)," *J. Chem. Phys.*, vol. 111, p. 5157, 1999.

[176] C. R. Stoldt, A. M. Cadilhe, M. C. Bartelt, C. J. Jenks, P. A. Thiel, and J. W. Evans, "Formation and relaxation of 2D island arrays in metal (100) homoepitaxy," *Prog. Surf. Sci.*, vol. 59, p. 67, 1998.

[177] R. Ganapathy, M. R. Buckley, S. J. Gerbode, and I. Cohen, "Direct measurements of island growth and step-edge barriers in colloidal epitaxy.," *Science*, vol. 327, p. 445, 2010.

[178] T. L. Einstein and T. J. Stasevich, "Epitaxial Growth Writ Large," *Science*, vol. 327, p. 423, 2010.

[179] F. L. Forgerini and W. Figueiredo, "Thin-film growth by random deposition of linear polymers on a square lattice," *Phys. Rev. E*, vol. 81, p. 51603, 2010.

[180] C.-H. Lam, "Kinetic Monte Carlo simulation of faceted islands in heteroepitaxy using a multistate lattice model," *Phys. Rev. E*, vol. 81, p. 021607, 2010.

[181] C. Misbah, O. Pierre-Louis, and Y. Saito, "Crystal surfaces in and out of equilibrium: A modern view," 2010.

[182] P. Šmilauer and D. D. Vvedensky, "Coarsening and slope evolution during unstable spitaxial growth," *Phys. Rev. B*, vol. 52, p. 14263, 1995.

[183] M. C. Bartelt and J. W. Evans, "Transition to multilayer kinetic roughening for metal (100) homoepitaxy," *Phys. Rev. Lett.*, vol. 75, p. 4250, 1995.

[184] D. P. Landau and S. Pal, "Monte Carlo simulation of simple models for thin film growth by MBE," *Thin Solid Films*, vol. 272, p. 184, 1996.

[185] P. I. Tamborenea and S. Das Sarma, "Surface-diffusion-driven kinetic growth on one-dimensional substrates," *Phys. Rev. E*, vol. 48, p. 2575, 1993.

[186] F. D. A. Aarão Reis, "Dynamic scaling in thin-film growth with irreversible step-edge attachment," *Phys. Rev. E*, vol. 81, p. 041605, 2010.

[187] W. Kanjanaput, S. Limkumnerd, and P. Chatraphorn, "Growth instability due to lattice-induced topological currents in limited-mobility epitaxial growth models," *Phys. Rev. E*, vol. 82, p. 041607, 2010.

[188] A. Baskaran and P. Smereka, "Mechanisms of Stranski-Krastanov Growth," *Arxiv preprint arXiv:1101.3775*, 2011.

[189] B. Poelsema, K. Lenz, L. S. Brown, L. K. Verheij, and G. Comsa, "Lateral distribution of ion bombardment induced defects on Pt(111) at 80 K," *Surf. Sci.*, vol. 162, p. 1011, 1985.

[190] S. Das Sarma, C. J. Lanczycki, S. V. Ghaisas, and J. M. Kim, "Defect formation and crossover behavior in the dynamic scaling properties of molecular-beam epitaxy," *Phys. Rev. B*, vol. 49, p. 10693, 1994.

[191] I. K. Marmorkos and S. Das Sarma, "Atomistic numerical study of molecular-beam-epitaxial growth kinetics," *Phys. Rev. B*, vol. 45, p. 11262, 1992.

[192] I. K. Marmorkos and S. Das Sarma, "Kinetic simulation of molecular beam epitaxial growth dynamics," *Surf. Sci. Lett.*, vol. 237, p. L411, 1990.

[193] C. J. Lanczycki and S. Das Sarma, "Nonequilibrium influence of upward atomic mobility in one-dimensional molecular-beam epitaxy," *Phys. Rev. E*, vol. 50, p. 213, 1994.

[194] C. R. Stoldt, K. J. Caspersen, M. C. Bartelt, C. J. Jenks, P. A. Thiel, and J. W. Evans, "Using Temperature to Tune Film Roughness: Nonintuitive Behavior in a Simple System," *Phys. Rev. Lett.*, vol. 85, p. 800, 2000.

[195] A. F. Voter and J. D. Doll, "Transition state theory description of surface self-diffusion: Comparison with classical trajectory results," *J. Chem. Phys.*, vol. 80, p. 5832, 1984.

[196] C. R. Stoldt, A. Cadilhe, C. J. Jenks, J.-M. Wen, J. W. Evans, and P. A. Thiel, "Evolution of Far-From-Equilibrium Nanostructures Formed by Cluster-Step and Cluster-Cluster Coalescence in Metal Films," *Phy. Rev. Lett.*, vol. 81, p. 2950, 1998.

[197] A. M. Cadilhe, C. R. Stoldt, C. J. Jenks, P. A. Thiel, and J. W. Evans, "Evolution of far-from-equilibrium nanostructures on Ag(100) surfaces: Protrusions and indentations at extended step edges," *Phys. Rev. B*, vol. 61, p. 4910, 2000.

[198] J. Villain, "Continuum models of crystal growth from atomic beams with and without desorption," *J. Phys. I*, vol. 1, p. 19, 1991.

[199] J. H. Neave, P. J. Dobson, B. A. Joyce, and J. Zhang, "Reflection high-energy electron diffraction oscillations from vicinal surfaces - a new approach to surface diffusion measurements," *Appl. Phys. Lett.*, vol. 47, p. 100, 1985.

[200] J. Krug, "Four lectures on the physics of crystal growth," *Physica A*, vol. 313, p. 47, 2002.

[201] M. I. Haftel, "Ehrlich-Schwoebel effect for vacancies: Low-index faces of silver," *Phys. Rev. B*, vol. 64, p. 125415, 2001.

[202] E. Cox, M. Li, P.-W. Chung, C. Ghosh, T. S. Rahman, C. J. Jenks, P. A. Thiel, and J. W. Evans, "Temperature dependence of island growth shapes during submonolayer deposition of Ag on Ag(111)," *Phys. Rev. B*, vol. 71, p. 115414, 2005.

[203] A. M. Ferrenberg, D. P. Landau, and K. Binder, "First-order versus second-order interface localization transition of thin Ising films with competing walls," *Phys. Rev. E*, vol. 58, p. 3353, 1998.

[204] R. L. Johnston, *Atomic and molecular clusters.* London: Taylor & Francis, 2002.

[205] C. R. Henry, "Surface studies of supported model catalysts," *Surf. Sci. Rep.*, vol. 31, p. 231, 1998.

[206] A. M. Bittner, "Clusters on soft matter surfaces," *Surf. Sci. Rep.*, vol. 61, p. 383, 2006.

[207] A. C. Templeton, W. P. Wuelfing, and R. W. Murray, "Monolayer-Protected Cluster Molecules," *Acc. Chem. Res.*, vol. 33, p. 27, 2000.

[208] K. G. Thomas and P. V. Kamat, "Chromophore-functionalized gold nanoparticles.," *Acc. Chem. Res.*, vol. 36, p. 888, 2003.

[209] M.-C. Daniel and D. Astruc, "Gold nanoparticles: assembly, supramolecular chemistry, quantum-size-related properties, and applications toward biology, catalysis, and nanotechnology.," *Chem. Rev.*, vol. 104, p. 293, 2004.

[210] T. L. Hill, *Thermodynamics of small systems*. Amsterdam: Dover Pubns, 2002.

[211] M. Brack, "The physics of simple metal clusters: self-consistent jellium model and semiclassical approaches," *Rev. Mod. Phys.*, vol. 65, p. 677, 1993.

[212] W. de Heer, "The physics of simple metal clusters: experimental aspects and simple models," *Rev. Mod. Phys.*, vol. 65, p. 611, 1993.

[213] J. P. K. Doye and D. J. Wales, "Global minima for transition metal clusters described by Sutton Chen potentials," *New J. Chem.*, vol. 22, p. 733, 1998.

[214] J. Uppenbrink and D. J. Wales, "Packing schemes for Lennard-Jones clusters of 13 to 150 atoms: minima, transition states and rearrangement mechanisms," *J. Chem. Soc. Faraday Trans.*, vol. 87, p. 215, 1991.

[215] Z. Li and H. A. Scheraga, "Monte Carlo-minimization approach to the multiple-minima problem in protein folding," *Proc. Nat. Acad. Sci.*, vol. 84, p. 6611, 1987.

[216] F. Baletto, A. Rapallo, G. Rossi, and R. Ferrando, "Dynamical effects in the formation of magic cluster structures," *Phys. Rev. B*, vol. 69, p. 235421, 2004.

[217] P. Milani and S. Iannotta, *Cluster beam synthesis of nanostructured materials*. Berlin: Springer, 1999.

[218] D. Reinhard, B. D. Hall, D. Ugarte, and R. Monot, "Size-independent fcc-to-icosahedral structural transition in unsupported silver clusters: An electron diffraction study of clusters produced by inert-gas aggregation," *Phys. Rev. B*, vol. 55, p. 7868, 1997.

[219] D. Reinhard, B. D. Hall, P. Berthoud, S. Valkealahti, and R. Monot, "Size-dependent icosahedral-to-fcc structure change confirmed in unsupported nanometer-sized copper clusters," *Phys. Rev. Lett.*, vol. 79, p. 1459, 1997.

[220] F. Baletto, C. Mottet, and R. Ferrando, "Reentrant morphology transition in the growth of free silver nanoclusters," *Phys. Rev. Lett.*, vol. 84, p. 5544, 2000.

[221] F. Baletto, C. Mottet, and R. Ferrando, "Non-crystalline structures in the growth of silver nanoclusters," *Eur. Phys. J. D*, vol. 16, p. 25, 2001.

[222] F. Baletto, C. Mottet, and R. Ferrando, "Microscopic mechanisms of the growth of metastable silver icosahedra," *Phys. Rev. B*, vol. 63, p. 155408, 2001.

[223] F. Baletto, J. Doye, and R. Ferrando, "Evidence of Kinetic Trapping in Clusters of C60 Molecules," *Phys. Rev. Lett.*, vol. 88, p. 075503, 2002.

[224] F. Baletto, R. Ferrando, A. Fortunelli, F. Montalenti, and C. Mottet, "Crossover among structural motifs in transition and noble-metal clusters," *J. Chem. Phys.*, vol. 116, p. 3856, 2002.

[225] D. Faken and H. Jónsson, "Systematic analysis of local atomic structure combined with 3D computer graphics," *Comp. Mat. Sci.*, vol. 2, p. 279, 1994.